Montanuniversität Leoben

The effects of alloying elements on the microstructure of Al-rich TiAl alloys

Diploma Thesis

Reinhold Wartbichler

This thesis was conducted at the Department Physical Metallurgy and Materials Testing at the Montanuniversität Leoben in Austria in cooperation with the Max Planck Institut für Eisenforschung GmbH in Düsseldorf, Germany.

Leoben, August 2017

I. Statutory declaration

I declare in lieu of oath, that I have developed and written the enclosed thesis by myself, and have not used sources or means without declaration in the text.

Leoben, 30/08/2017 Reinhold Wartbichler

II. Acknowledgement

I would hereby like to thank Svea Mayer and Helmut Clemens for the possibility to conduct this thesis at the Department Physical Metallurgy and Materials Testing at the Montanuniversität Leoben and the very extensive supervision. Furthermore, I want to express my gratitude towards Martin Palm and Frank Stein from the Max Planck Institut für Eisenforschung GmbH for the exceptional assistance and the opportunity for a stay in Düsseldorf, which was very rewarding.

III. Table of contents

I. Statutory declaration i

II. Acknowledgement ii

III. Table of contents iii

IV. List of abbreviations and symbols v

1 Introduction and motivation 1

2 Literature survey and previous results 3

2.1 Phase equilibria in the Al-rich part of the TiAl phase diagram 3
2.2 Phase reactions in the Al-rich part of the TiAl phase diagram 6
2.2.1 Melting and solidification 6
2.2.2 Solid-state reactions 6
2.3 Phases in the Al-rich part of the TiAl phase diagram 7
2.4 Ordering process of Al-rich-TiAl crystals 8
2.5 Microstructural evolution in Al-rich TiAl alloys 10
2.6 Thermal stability of Ti_3Al_5 and h-$TiAl_2$ 13
2.7 Microstructural influence of Niobium in Al-rich TiAl alloys 15
2.8 Alloying of $TiAl_3$ to form $L1_2$ cubic phases 16

3 Experimental procedure 18

3.1 Investigated alloys 18
3.2 Heat treatments 19
3.3 Scanning electron microscopy 20
3.4 Electron probe micro analysis 20
3.5 X-ray diffraction 20
3.6 Differential thermal analysis 20
3.7 Differential scanning calorimetry 21

4 Results 22

4.1 Microstructural characterization 22
4.1.1 As-cast state 22
4.1.2 Heat-treated state: 1000 °C / 200 h / WQ 29
4.1.3 Heat-treated state: 1000 °C / 24 h / WQ 38
4.1.4 Heat-treated state: 800 °C / 500 h / WQ 41
4.1.5 Heat-treated state: 800 °C / 24 h / WQ 46
4.1.6 Heat-treated state: 1400 °C / 1 h / FC 47
4.2 Thermal Investigation 49
4.2.1 Differential thermal analysis 49
4.2.2 Differential scanning calorimetry 50
4.2.2.1 Determination of the γ-TiAl/r-$TiAl_2$ ↔ γ-TiAl transition temperature 54
4.2.2.2 Determination of the Ti_3Al_5 decomposition temperature 56
4.2.3 The quasi binary Ti-60Al - Mo phase diagram 58

5 Discussion 61

6 Conclusions **69**
7 Bibliography **71**

IV. List of abbreviations and symbols

at.%	Atomic percent
BSE	Back-scattered electrons
DSC	Differential scanning calorimetry
DTA	Differential thermal analysis
EDX	Energy dispersive X-ray
EPMA	Electron probe micro analysis
FC	Furnace cooling
LM	Levitation melting
LP	Long period
SEM	Scanning electron microscopy
TEM	Transmission electron microscopy
VAR	Vacuum arc remelting
WDX	Wavelength dispersive X-ray
WQ	Water quenching
XRD	X-ray diffraction
λ	Wavelength

1 Introduction and motivation

Future advanced high performance materials need to maintain high specific strength and low weight. These properties are required for the next generations of automotive and aeronautic applications to further improve efficiency and lower fuel consumption as well as CO_2 emission [1, 2]. Exemplary novel lightweight materials as γ-TiAl based alloys generate two-phase lamellar microstructures of γ-TiAl and Ti_3Al and thus feature sufficient strength at elevated temperature as well as ductility at ambient temperature [3].

Current scientific activities often focus on further improving creep resistance and oxidation behaviour at elevated temperature of this alloy system. Exceeding alumina contents of 54 atomic percent improves oxidation behaviour due to forming of Al_2O_3 layers even at highly increased temperature up to 1200 °C [4]. Furthermore, increasing the alumina content results in a lower density of about 3.2 g cm^{-3} compared to about 4.0 g cm^{-3} of γ-TiAl/Ti_3Al alloys. In addition, lamellar microstructures consisting of γ-TiAl and r-$TiAl_2$ are producible for alumina-rich alloys, which may improve creep behaviour [5]. Therefore, Al-rich TiAl alloys may offer the required properties for high performance structural materials.

The complexity of the Al-rich TiAl system increases with the formation of metastable phases impeding the generation of equilibrium microstructures and leading to embrittlement of the alloy. In addition, the adjusting microstructure highly depends on earlier heat treatments and the processing technique.

Although the phase equilibrium in the binary system has already been extensively investigated, knowledge about the influences of additional alloying elements is scarce. Information about whether additional alloying elements could suppress unwanted, embrittling metastable phases and accelerate phase transition to a highly desired, lamellar microstructure in an equilibrium state or not is therefore worth investigating. This present diploma thesis examines the influence of alloying elements such as Mo, Nb and B on the microstructural development of Al-rich TiAl alloys, as well as the influence on microstructural evolution in terms of kinetics and transition temperatures.

For these purposes, several compositions of Al-rich TiAl alloys containing approximately 60 atomic percent (at.%) alumina and additional alloying elements in different ranges were prepared. Furthermore, two different processing routes, levitation melting (LM) and vacuum arc remelting (VAR), and their influence on the adjusting microstructures were investigated.
Several heat treatments were carried out to offer possible comparison to the binary system and influential interpretation of alloying elements. These samples were metallographically prepared and investigated via Scanning Electron Microscope (SEM). Additionally, Electron Probe Micro Analysis (EPMA) was performed to further investigate phase and equilibrium compositions as well as possible solubility limits. To identify the occurring phases, X-ray diffraction was executed on powder samples. In addition, differential scanning calorimetry (DSC) and differential thermal analysis (DTA) were carried out to gain information about transition temperatures of stable as well as metastable phases.

Results were summarized in a quasibinary phase diagram to further visualize the influence of the alloying elements mentioned above on the microstructural evolution of Al-rich TiAl alloys.

The present diploma thesis was conducted at the Department Physical Metallurgy and Materials Testing at the Montanuniversität Leoben in Austria in cooperation with the Max Planck Institut für Eisenforschung in Düsseldorf, Germany.

2 Literature survey and previous results

2.1 Phase equilibria in the Al-rich part of the TiAl phase diagram

The availability of properly settled phase diagrams plays an important role for alloy development of all kind and especially for structural, high performance materials. In terms of Al-rich TiAl alloys, investigation of the phase equilibria offered several challenges and was therefore handled with incertitude.

Throughout the available literature up to eight different intermetallic phases were identified additionally to γ-TiAl during the investigation of the Al-rich TiAl phase diagram ($TiAl_2$, Ti_2Al_5, Ti_3Al_5, $TiAl_3$,$Ti_{1-x}Al_{1+x}$, r-$TiAl_2$, h-$TiAl_2$, $Al_{23}Ti_9$/$Al_{24}Ti_8$) [6]. Multiple reasons caused difficulties in establishing an adequate binary system. Whereas phases in the Ti-rich part of the TiAl phase diagram offer several easily distinguishable crystallographic structures [7], the occurring phases on the Al-rich side are much more closely related. In fact, all of them are one-dimensional, long range ordered superstructures composed of different stacking sequences of the $L1_0$ cell with additional Al-layers along the c-axis [6]. Furthermore, these structures are often only receivable for very narrow composition ranges, of which some are very close to each other. Therefore, phase characterizations via X-ray diffraction patterns often rely on appropriate intensity of superlattice diffraction peaks to properly identify a phase and becomes suitable difficult if more than one long range superstructure is present.

In addition, several durable metastable phases impede culmination of equilibrium states and possible contaminations with gaseous impurities especially during high temperature heat treatments endanger accuracy of scientific results [8]. Also, alumina is prone to evaporate at elevated temperatures [9].

Hence some phase boundaries were often unassertive in appropriate data and were therefore displayed as broken lines. The current state of the art binary phase diagram for the Ti-Al system is given in figure 2.1 [10].

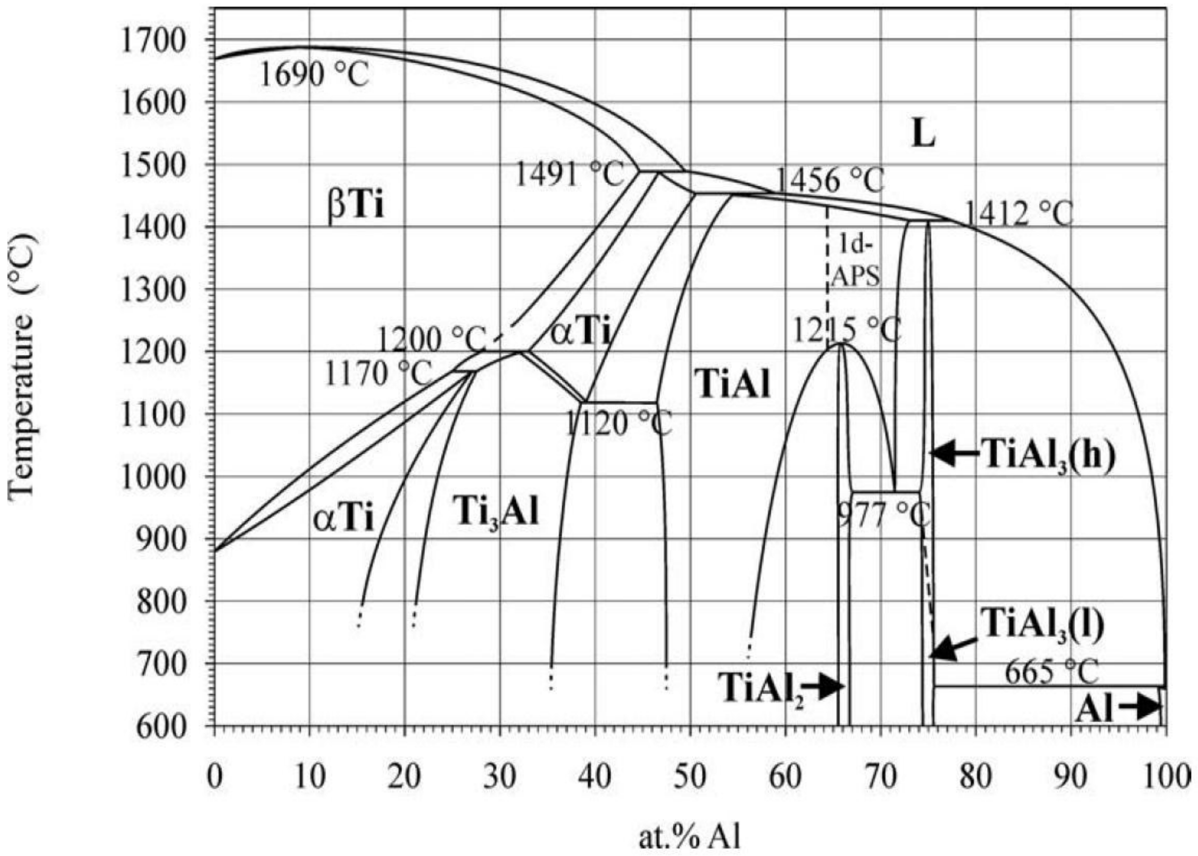

Fig. 2.1: Ti-Al system according to [10]

The driving force for the various reactions taking place at respectively high alumina content exceeding 55 atomic percent is the strong dependence of the alumina solubility in the γ-TiAl $L1_0$ cell on temperature. With decreasing temperature, these solubility decreases and Al-rich phases form.

The current assessment displays additionally to γ-Ti-Al the stable phases r-$TiAl_2$ and $TiAl_3$ in the Al-rich section of the phase diagram. Furthermore, metastable phases, such as h-$TiAl_2$ and Ti_3Al_5, can be observed at room temperature, which form instantly during cooling because the transformation to r-$TiAl_2$ occurs via comparatively slow reactions [6]. At elevated temperature, metastable superstructures frequently called "one-dimensional antiphase domain structures" (1d-APSs) are observable (which were denoted as Ti_5Al_{11} [11], Ti_2Al_5 [12], γ_2 [13], long period structures (LP) [14] or 1d-APS [15]). Due to their metastability, the corresponding phase border is displayed with a broken line. It has yet to be clarified, whether narrow two-phase fields exist, γ-TiAl second order transists to 1d-APS or if transient 1d-APS structures form upon cooling via precipitation reactions. Furthermore, two different $TiAl_3$ modifications are present in the current assessment. Figure 2.2 shows currently assessed stability ranges for several Al-rich phases. and the metastable phase Ti_3Al_5.

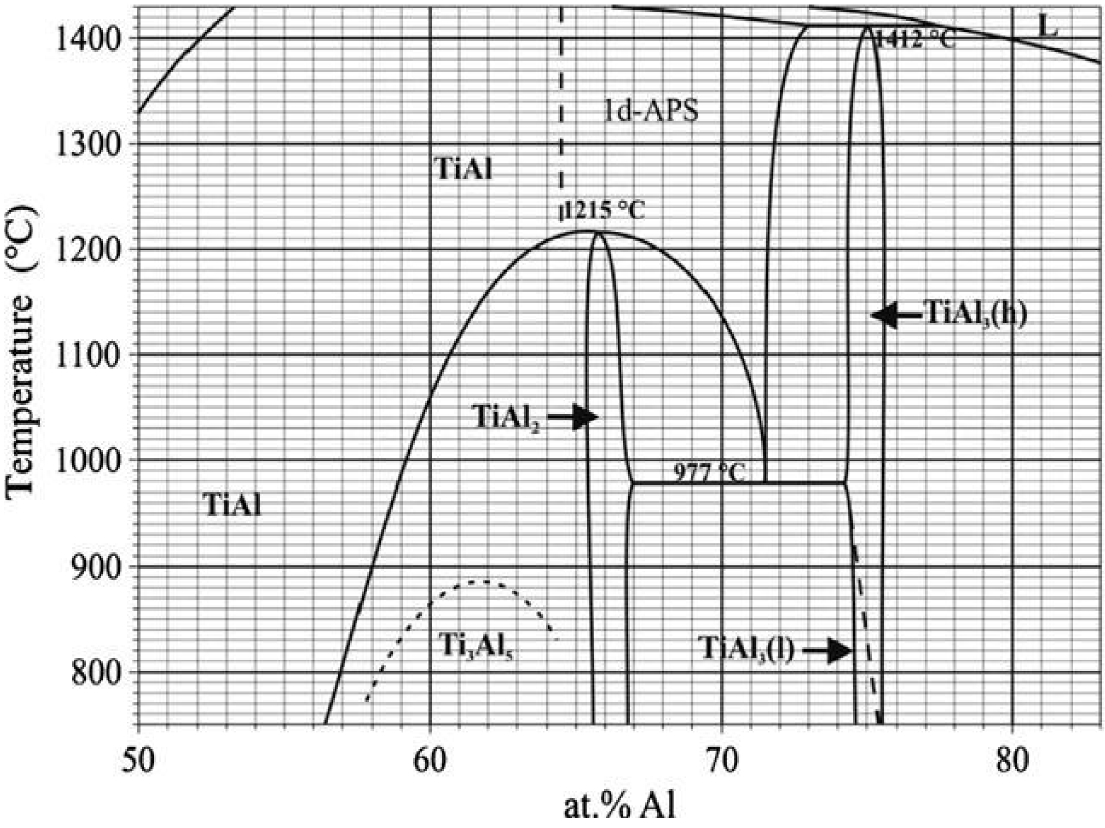

Fig. 2.2: Stability ranges of several stable and metastable Al-rich TiAl phases according to [10]

The actual existence of the $Ti_{1-x}A_{1+x}$ phase is currently disputed. Although such a phase was reported [8, 16], a required two-phase region for the existence of this phase could not be found in corresponding literature [6, 13] and the representing XRD-spectra endangers confusion with overlapping spectra of γ-TiAl and h-$TiAl_2$. The next section describes the currently established stable phase reactions occurring in the Al-rich part of the Ti-Al system.

2.2 Phase reactions in the Al-rich part of the TiAl phase diagram

The following phase reactions are in comprehension to the currently available assessment of the Ti-Al system according to [10]. "L" implies the liquefied material.

2.2.1 Melting and solidification

The Al-rich section of the Ti-Al system includes 2 invariant peritectic reactions covering the liquid phase.

- L + l-$TiAl_3$ ↔ Al at 665 °C and 99.92, 75.5, 99.2 at.% Al (2.1)
- L + “X” ↔ h-$TiAl_3$ at 1412 ± 4 °C and 77.5, 73, 75 at.% Al (2.2)

The "X" herby refers to Ti_5Al_{11}, Ti_2Al_5, γ_2, long period structures (LP) or 1d-APS, as mentioned in section 2.1.

2.2.2 Solid-state reactions

Three different solid-state reactions take place in the Al-rich area of the Ti-Al phase diagram applying to stable phases.

- γ-TiAl/"X" ↔ $TiAl_2$ at 1215 °C and 65.7 at.% Al (2.3)

  Due to decreasing solubility of Al in γ -TiAl/"X" with reducing temperature $TiAl_2$ precipitations form during cooling. The metastable phase h-$TiAl_2$ establishes with less effort than its stable counterpart r-$TiAl_2$ due to closer crystallographic relations (see further sections).

- γ-TiAl/"X" ↔ $TiAl_2$ + h-$TiAl_3$ at 977 ± 3 °C and 71.5, 67.0, 74.2 at.% Al (2.4)

  This reaction shows the eutectoid decomposition of γ-TiAl/"X" into Al-rich phases. The compositions of $TiAl_2$ and h-$TiAl_3$ are almost settled due to very narrow homogeneity ranges.

- h-$TiAl_3$ ↔ l-$TiAl_3$ (2.5)

  Two different modifications were reported for $TiAl_3$ [17]. Currently stability ranges and transformation temperatures lack proper data and are therefore not assessed with certainty.

2.3 Phases in the Al-rich part of the TiAl phase diagram

Table 2.1 includes crystallographic data for stable as well as metastable phases of the Al-rich part of the TiAl phase diagram. The content is based on [7]. As previously mentioned, all of them are one dimensional, long range ordered superstructures composed of different stacking sequences of the $L1_0$ cell (which is featured by γ-TiAl) with additional Al-layers along the c-axis [6]. In the column "Stability" a "s" implies a stable phase, whereas a "m" denotes a metastable structure.

Table 2.1: Crystallographic data of Al-rich phases in the TiAl phase diagram [7]

Designation	**Pearson symbol**	**Space Group**	**Stability**	**Lattice parameters**	**Prototype**
γ TiAl	tP4	P4/mmm	s	a=0.3997nm c=0.4062nm	AuCu
r-$TiAl_2$	tI24	$I4_1$/amd	s	a=0.3971nm c/6=0.4052nm a/c=1,02	$HfGa_2$
h-$TiAl_2$	oC12	Cmmm	m	a/3=0.4032nm b=0.3959nm c=0.4032nm	$ZrGa_2$
$TiAl_3$(h)	tI8	I4/mmm	s	a=0.3849nm c/2=0.4305nm	$TiAl_3$(h)
$TiAl_3$(l)	tI32	I4/mmm	s	a=0,3877nm c/2=0.4229nm	$TiAl_3$(l)
Ti_3Al_5	tP32	P4/mbm	m	a/4=0.3980nm c=0.4038nm	Ti_3Ga_5

As derivable from the corresponding Pearson symbol, each of these crystal structures except for the h-$TiAl_2$ is tetragonal. The orthorhombic crystal of the h-$TiAl_2$ offers the opportunity to distinguish r-$TiAl_2$ and h-$TiAl_2$ from XRD-patterns more easily than its $L1_0$ based relatives. Furthermore, adjacency to the equilibrium state may be derived from the pattern, as h-$TiAl_2$ is a metastable phase contrary to r-$TiAl_2$. The following subchapters go deeper into the specific phases and their properties.

Figure 2.3 shows crystal structures for the $L1_0$ cell as well as h-$TiAl_2$, r-$TiAl_2$ and Ti_3Al_5, which are of uttermost importance to this present thesis. All of them possess different lattice periodicity. Whereas r-$TiAl_2$ holds six-fold periodicity along the c axis, h-$TiAl_2$ has three-fold periodicity along the b-axis and Ti_3Al_5 four-fold periodicity along the a- and b-axis. Furthermore, whereas every second layer parallel to the (002)-plane for Ti_3Al_5 and h-$TiAl_2$ contains only Al atoms, the periodicity for the Al-layers in r-$TiAl_2$ is every third. Therefore, the metastable structures are crystallographically more closely related to the $L1_0$ structure than r-$TiAl_2$ [18].

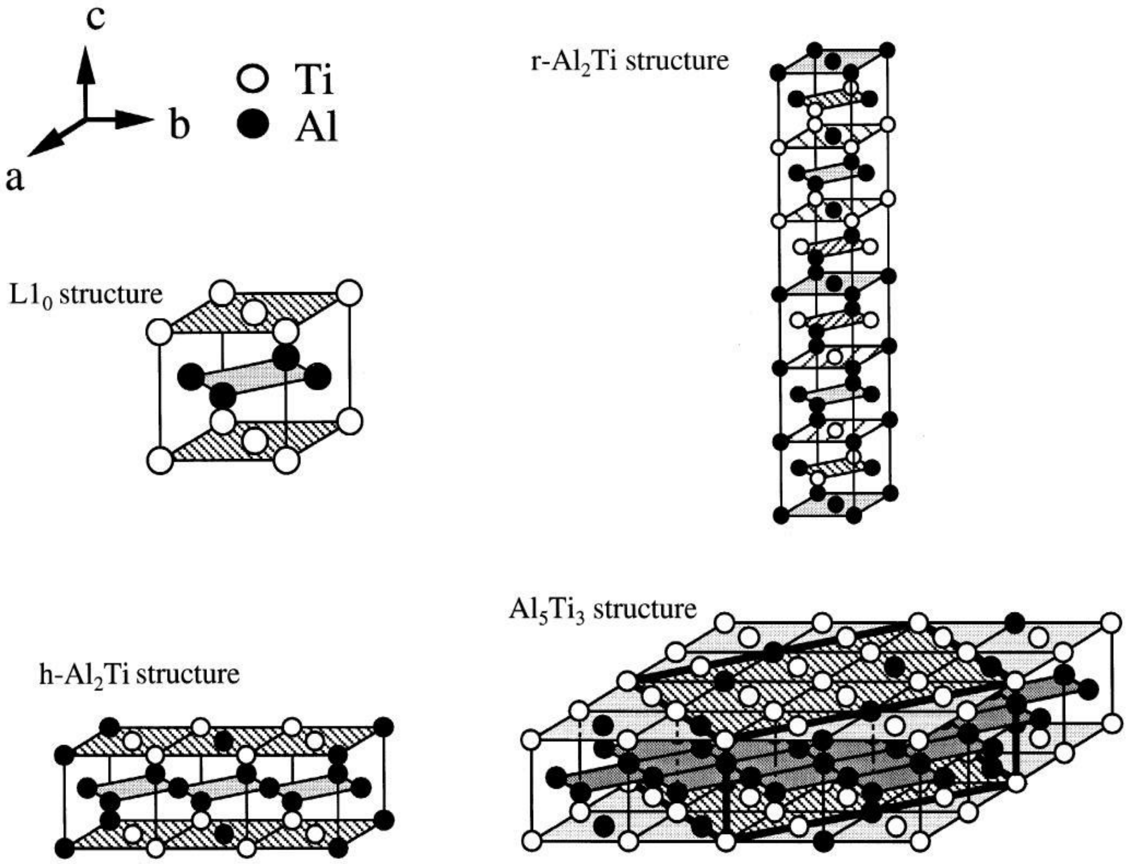

Fig. 2.3: Crystal structures for several phases present in the Al-rich section of the TiAl phase diagram [18]

The following section describes the formation of these ordered, Al-rich structures from an oversaturated γ-TiAl crystal.

2.4 Ordering process of Al-rich-TiAl crystals

The crystallographic relationships between the $L1_0$-γ-TiAl phase and several Al-rich intermetallic phases were observed in [18] using electron diffraction patterns. The following information is based on that specific work.

For h-$TiAl_2$, two types were observed that satisfy the following relationship:

$$[001]_{L1_0}//[001]_{h\text{-}TiAl_2},\ [100]_{L1_0}//[100]_{h\text{-}TiAl_2} \tag{2.6}$$

$$[001]_{L1_0}//[001]_{h\text{-}TiAl_2},\ [100]_{L1_0}//[010]_{h\text{-}TiAl_2} \tag{2.7}$$

Both phases share the same periodic Al-layers in either relationship, therefore high coherency is maintained at the interface.

Furthermore, the determined relation for Ti_3Al_5 is as follows:

$$<001]_{L1_0}//<001]_{Ti_3Al_5},\ <100]_{L1_0}//<100]_{Ti_3Al_5} \tag{2.8}$$

Relationship (2.8) is very similar to (2.6) and (2.7) and results also in common Al-layers for γ-TiAl and Ti_3Al_5.

On samples containing γ-TiAl as well as h-$TiAl_2$ and precipitates of r-$TiAl_2$ the following relationship was observable:

$$[001]_{L1_0}//[001]_{h\text{-}TiAl_2}//<100]_{r\text{-}TiAl_2},\ <100]_{L1_0}//[100]_{h\text{-}TiAl_2}//<010]_{r\text{-}TiAl_2} \tag{2.9}$$

The (002) Al-layers of r-$TiAl_2$ are therefore perpendicular to those contained in γ-TiAl and h-$TiAl_2$ and semi-coherent boundaries are established.

Figure 2.4 shows the atomic arrangements on the (002) Ti-rich-layers for Al-rich TiAl-superstructures, where Al-layers appear alternatively on (002) planes. Whereas the $L1_0$ structure is the crystal with stoichiometric concentration for TiAl, the $L1_0$' structure contains Al atoms on the (002) Al-planes and excess Al atoms on random Ti sites of the (002) Ti-plane. Therefore, the formation of ordered Al-rich superstructures sharing the same parallel (002) Al layers is a rather ordinary process by just ordering the surplus Al atoms on the (002) Ti-planes. Specifically, the formation of Ti_3Al_5 is less hindered due to having a smaller amount of Al atoms on the Ti plane to order than h-$TiAl_2$ [18].

Because h-$TiAl_2$ also has different arrangements of the atoms along the a- and b-axis, whereas the Ti_3Al_5 shows no such anisotropy, it is proposed in [18] that the h-$TiAl_2$ structure has therefore a higher coherent strain energy at the interface to the $L1_0$ phase, often resulting in lamellar structures contrary to Ti_3Al_5.

Note: The $L1_2$ phase under section d) in Figure 2.4 refers to $TiAl_3$ complemented with particular ternary alloying elements, stabilizing the $L1_2$ crystal structure rather than the $D0_{22}$ for stoichiometric TAl_3. Further information is included in section 2.8.

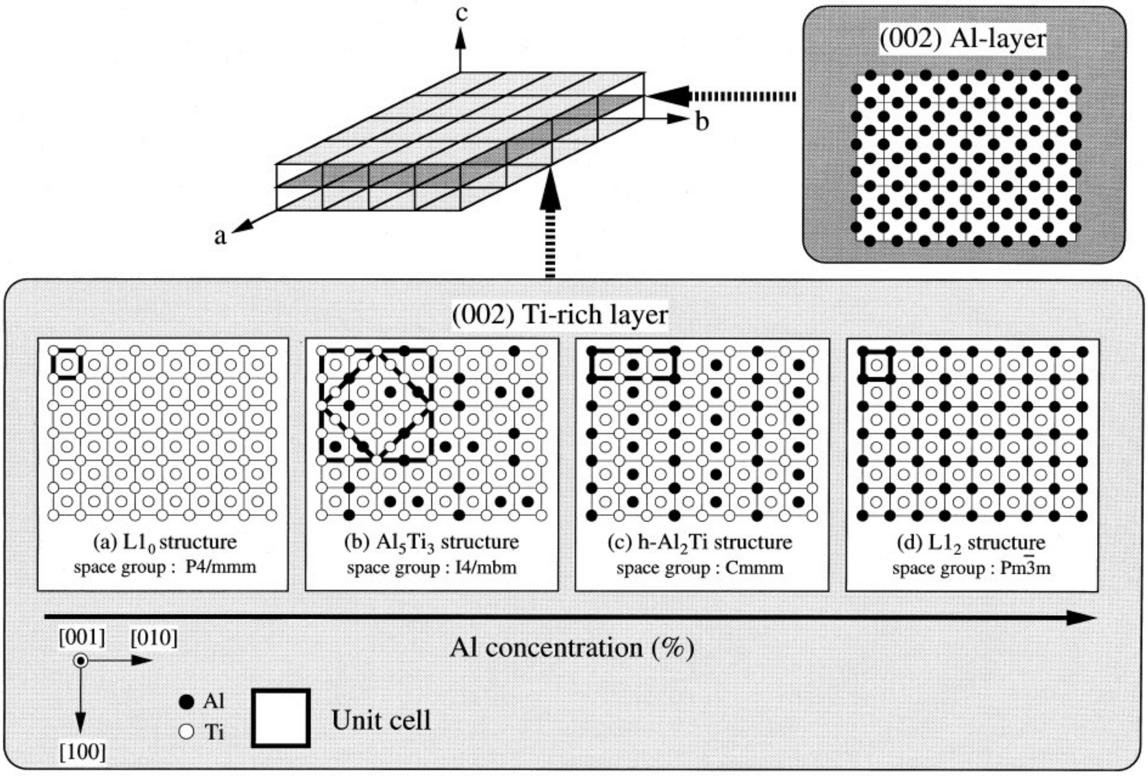

Fig. 2.4: Atomic arrangements for the (002) planes for γ-TiAl($L1_0$) and several Al-rich TiAl intermetallic phases [18]

Since the arrangement of Al-layers for the stable r-$TiAl_2$ phase requires extensive diffusion on the contrary to its metastable counterparts, r-$TiAl_2$ precipitations tend to form from grain boundaries and triple junctions [18]. Therefore, metastable phases such as h-$TiAl_2$ and Ti_3Al_5 nucleate more easily and are rather persistent.

The following section concerns possible microstructural evolution in Al-rich TiAl alloys considering the formation processes of these intermetallic phases.

2.5 Microstructural evolution in Al-rich TiAl alloys

As already mentioned in section 1, γ-TiAl/Ti_3Al based alloys fulfill their required material properties by combining high ductility of a duplex microstructure with high toughness and creep resistance of lamellar formations [2]. Lamellar microstructures are also obtainable in Al-rich TiAl alloys exceeding 55 at.% Al content. Figure 2.5 shows a light-optical micrograph of Ti-62 at.% Al, which has been annealed at 950 °C for 200 h to achieve equilibrium state, and its lamellar microstructure of γ-TiAl and r-$TiAl_2$ [5].

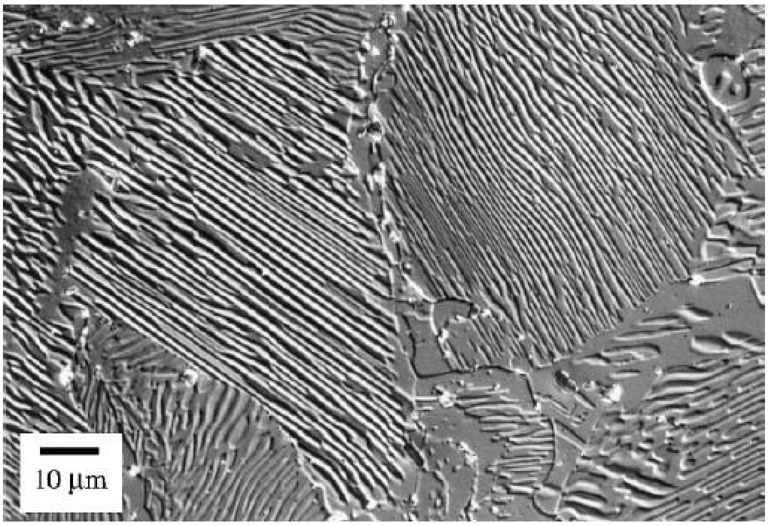

Fig. 2.5: Light optical micrograph of Ti-62 at.% Al annealed at 950 °C for 200 h consisting of a lamellar γ-TiAl+r-$TiAl_2$ microstructure [5]

The transformation from the metastable h-$TiAl_2$ to the stable r-$TiAl_2$ takes place by two mechanisms, both of which are shown in figure 2.6. The first one herby is the continuous transformation by advancing elimination of anti-phase-boundaries which separate the h-$TiAl_2$ and r-$TiAl_2$ structure and leaves planar defects observable via transmission electron microscopy (TEM). Thereby, the orientation relationship between γ-TiAl and h-$TiAl_2$ gets inherited by the r-$TiAl_2$ and equals equation (2.9).
A second transformation mechanism takes place as a discontinuous reaction. The stable r-$TiAl_2$ plates precipitate from γ-TiAl after dissolution of h-$TiAl_2$. The continuous mechanism is rather sluggish according to [5], whereas the discontinuous reaction is quicker once it has started. The relationship between the crystal orientations is not inherited and was found to be as follows:

$$[001]_{L1_0} // <001]_{r\text{-}TiAl_2},\ <010]_{L1_0} // <010]_{r\text{-}TiAl_2} \tag{2.9}$$

The second, discontinuous transformation process leads therefore to a different orientation relationship that leads to lamellar microstructures of γ-TiAl and r-$TiAl_2$. Determination of the specific formation process of r-$TiAl_2$ is therefore possible by establishing of the orientation relationship between γ-TiAl and r-$TiAl_2$. Due to the sluggishness of these transformation reactions, the metastable h-$TiAl_2$ remains rather persistent and extensive annealing is necessary to achieve equilibrium state.
Additionally, further annealing also coarsens the lamellar structure according to [9].

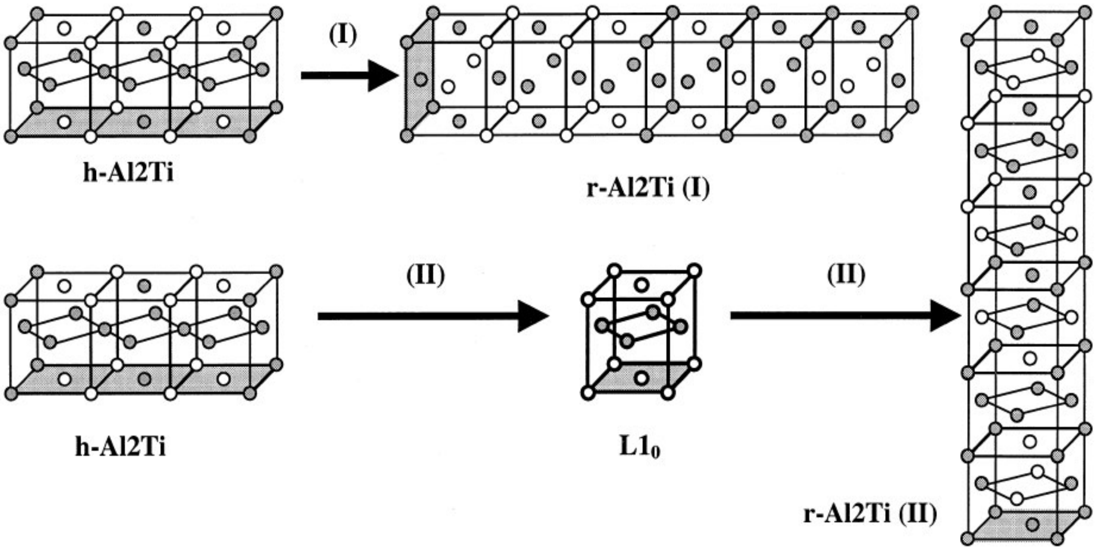

Fig. 2.6: Schematic illustration of the phase transformation from h-$TiAl_2$ to r-$TiAl_2$ via (I) continuous transformation and (II) discontinuous transformation [5]

Nevertheless, not only the occurring transformation reaction and fitting heat treatments are key prerequisites for suitable microstructures for possible high-performance applications, also the initial microstructure from the processing highly influences the possibilities of Al-rich TiAl alloys.

Though h-$TiAl_2$ dissolves in γ-TiAl during the discontinuous reaction forming lamellar structures, it is also relevant whether h-$TiAl_2$ is present at grain boundaries, which leads to nucleation of globular r-$TiAl_2$ at those boundaries and only a possible growth of few coarse lamellae into the grain or not, which might lead to fully lamellar structures. A fully oversaturated γ-TiAl crystal is necessary in order to achieve this fully lamellar structure [19].

Figure 2.7 shows two SEM-BSE images of Ti-59.7 at.% Al, which were processed by centrifugally cast (left), and Ti-59.4 at.% Al, which is a single crystal by float zone processing (right), both annealed at 900 °C for 100 h. Due to h-$TiAl_2$ at grain boundaries, no fully lamellar structure is achievable in the centrifugally cast sample and the grain boundaries are covered with globular r-$TiAl_2$, whereas the float zone single crystal has no grain boundaries and therefore a fully lamellar microstructure.

Proper knowledge of the stability ranges of the metastable phases in the Al-rich section of the TiAl phase diagram is also required to control microstructural evolution. Therefore, the next section deals with the thermal stability of the metastable phases Ti_3Al_5 and h-$TiAl_2$.

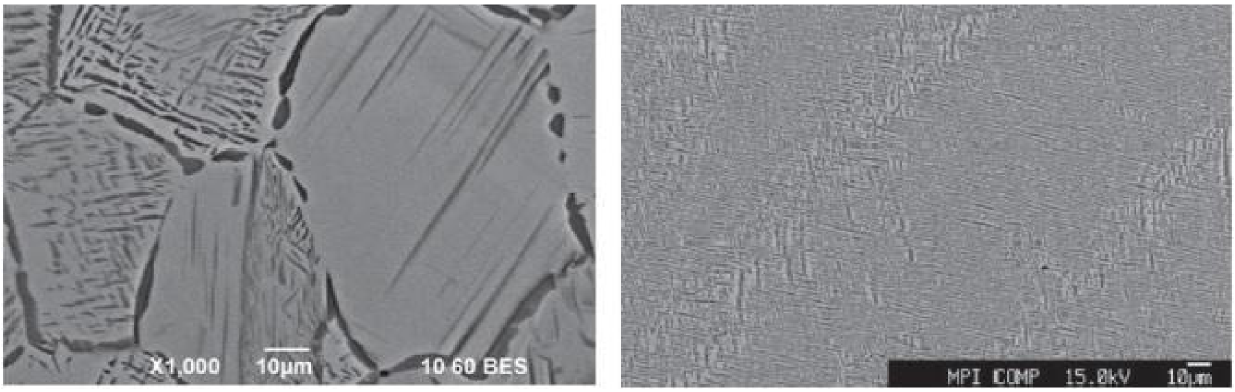

Fig. 2.7: SEM-BSE images of centrifugally cast Ti-59.7 at.% Al (left) and float zone single crystal Ti-59.4 at.% Al (right) with microstructures consisting of γ-TiAl (light) and r-$TiAl_2$ (dark) [19]

2.6 Thermal stability of Ti_3Al_5 and h-$TiAl_2$

The high decline of the Al-solubility with decreasing temperature in the γ-TiAl phase is the reason for formation of various Al-rich superstructures from oversaturated $L1_0$ crystals. As shown in sections 2.4 and 2.5, the equilibrium phase r-$TiAl_2$ does not form instantaneously, but rather the metastable phases Ti_3Al_5 and h-$TiAl_2$. Both of them are crystallographically more closely related to γ-TiAl because only short-range diffusion is required for their formation.

As concluded in [6], h-$TiAl_2$ is no equilibrium phase due to discovered violations of the Gibbs phase rule and missing phase contact with all present phases, as to be expected from an equilibrium phase. Furthermore, it was concluded in [20] that Ti_3Al_5 it is no stable phase as well. After the annealing of Ti-62 at.% Al samples above the decomposition temperature of Ti_3Al_5 but below the γ-TiAl one phase field at 900 °C for 200 h no traces of Ti_3Al_5 could be found again, even after performing heat treatments, that previously lead to large Ti_3Al_5 domains. If the annealing temperature was in the range of 1100 to 1176 °C, the portion of supersaturated γ-TiAl was already high enough for Ti_3Al_5 to form again during cooling. Furthermore, if Ti_3Al_5 was a stable phase, a single-phase field between γ-TiAl and r-$TiAl_2$ should exist, and in addition, a peritectoid reaction in the range of 850 to 900 °C should be observable, independent from small composition changes at constant temperature. Such a reaction could not be found with differential thermal analysis (DTA), and therefore metastability of Ti_3Al_5 was concluded [20].

The decomposition temperature of Ti_3Al_5 is highly depending on the sample composition. The highest state of stability is reached near the stoichiometric composition of 62.5 at.% Al, where the highest value for the decomposition temperature is observed. Ti_3Al_5 dissolves rapidly above that decomposition temperature [21]. Figure 2.8 shows the Ti-Al phase diagram between 54 and 65,5 at.% Al according to [9] and [20], investigated with differential thermal analysis (DTA) and electron probe micro analysis (EPMA). The dotted line represents the observed decomposition temperature for Ti_3Al_5.

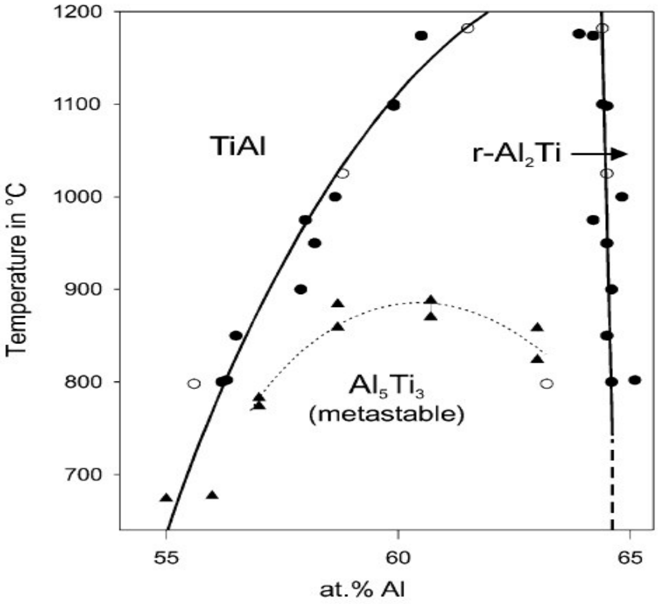

Fig. 2.8: Binary phase diagram of Ti-Al between 54 and 65.5 at.% Al, the dotted line marks the decomposition temperature of Ti_3Al_5 [9, 20]

Furthermore, the microstructure containing Ti_3Al_5 is dependent on the Al content. In case of investigated Ti-62 at.% Al, which is close to stoichiometric Ti_3Al_5, large domains of Ti_3Al_5 were observable when annealed at 800 °C. For 60 at.% Al, the developing microstructure for an annealing heat treatment at 800 °C is completely different. Due to the composition being central between γ-TiAl and Ti_3Al_5 at this temperature, a tweed-like lamellar microstructure could be investigated. Figure 2.9 shows a TEM micrograph of such lamellar γ-TiAl+Ti_3Al_5 structures of Ti-60 at.% Al annealed at 800 °C for 500 h [20]. In both cases, Ti_3Al_5 rapidly dissolves when crossing the decomposition line.

Although the decomposition temperature line could be investigated successfully with DTA [20], the actual temperature where Ti_3Al_5 starts to dissolve is dependent on the annealing state. Microstructures obtained by long-time annealing like in figure 2.9 increase the decomposition temperature remarkably up to 25 degrees, whereas additional reheating results in the original, unimpaired temperature values [20]. The reasons are differences in interfacial energies due to formation of certain microstructures [19].

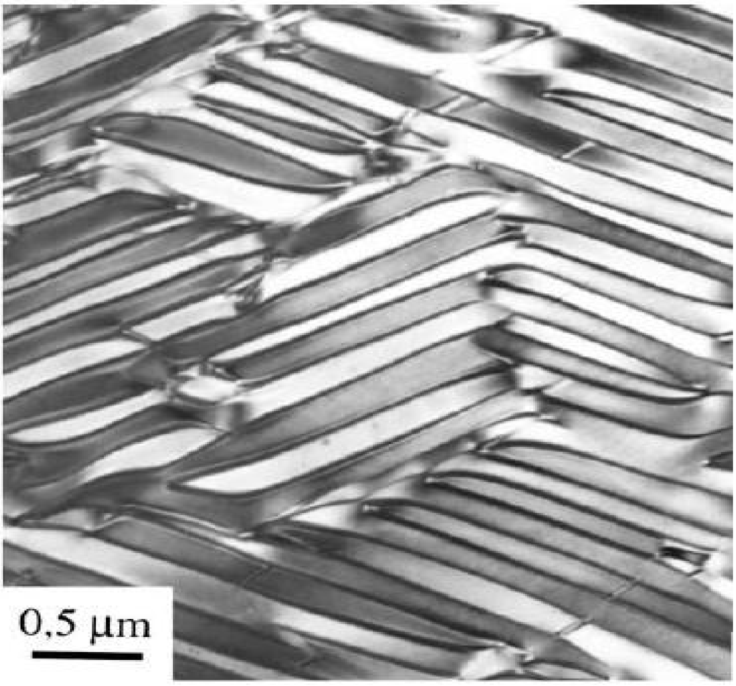

Fig. 2.9: TEM image of tweed-like γ-TiAl+Ti_3Al_5 structure observed in Ti-60 at.% Al after annealing for 500 h at 800 °C [20]

Due to its embrittling nature for Al-rich alloys, the formation of Ti_3Al_5 needs to be preferably prevented for a possible high-performance application of Al-rich TiAl alloys. It is yet to investigate whether additional alloying elements impede appearance and development of this metastable phase and to which extend. Therefore, this remains a matter this thesis wants to address.

2.7 Microstructural influence of Niobium in Al-rich TiAl alloys

Although the Al-rich section of the TiAl phase diagram has already been extensively investigated, microstructural influences of ternary alloying elements are still rather unknown to the present day. In [22] samples consisting of Ti-62 at.% Al-2 at.% Nb were investigated after annealing at 950 °C for 50 h. Figure 2.10 shows a light-optical micrograph of aforesaid sample with a fine lamellar microstructure consisting of γ-TiAl and r-$TiAl_2$, as identified via X-ray diffraction. Furthermore, the author of [22] reported improvements with casting of those ternary alloyed specimens and a decreasing amount of radial cracks in the as-cast state.

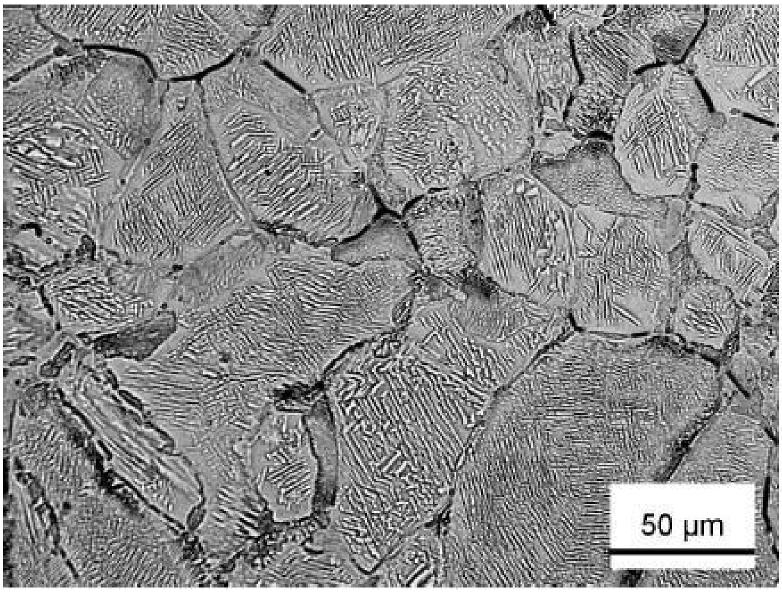

Fig. 2.10: Light-optical micrograph of Ti-62 at.% Al-2 at.% Nb annealed at 950 °C for 50 h showcasing a lamellar microstructure of γ-TiAl and r-$TiAl_2$ [22]

The influences of increased amounts of Niobium and different additional alloying elements remain uncertain.

2.8 Alloying of $TiAl_3$ to form $L1_2$ cubic phases

Due to proper oxidation resistance and appropriate specific mechanical properties, $TiAl_3$ offers several qualities for a high performance structural material. Partially due to its tetragonal crystal structure, $TiAl_3$ suffers from poor ductility and toughness [23] though. Addition of fourth period elements such as Cr, Mn, Zn, Cu and Fe change the $D0_{22}$ crystal to a cubic $L1_2$, which leads to an increase of mechanical properties and improved ductility, especially for an addition of Cr and Mn [23 - 25]. The actual solubility range for fourth period elements in the tetragonal $TiAl_3$ crystal is in the range of 1 at.%. Above this solubility limit, the spare atoms start to occupy unusual lattice sites until the tetragonal lattice changes to a cubic version with a specific threshold limit for the specific ternary element. Figure 2.11 shows ternary phase diagrams for Al-Cr-Ti and Al-Mn-Ti and the determined range of the $L1_2$ structure according to [23].

Typical $L1_2$ ternary alloys are $Al_{67}Cr_8Ti_{25}$ and $Al_{67}Mn_8Ti_{25}$. Though the investigated specimens in this work contain a lower Al content, suppression of several Al-rich phases and formation of $TiAl_3$ based or similar structures at a lower Al content might be a possibility.

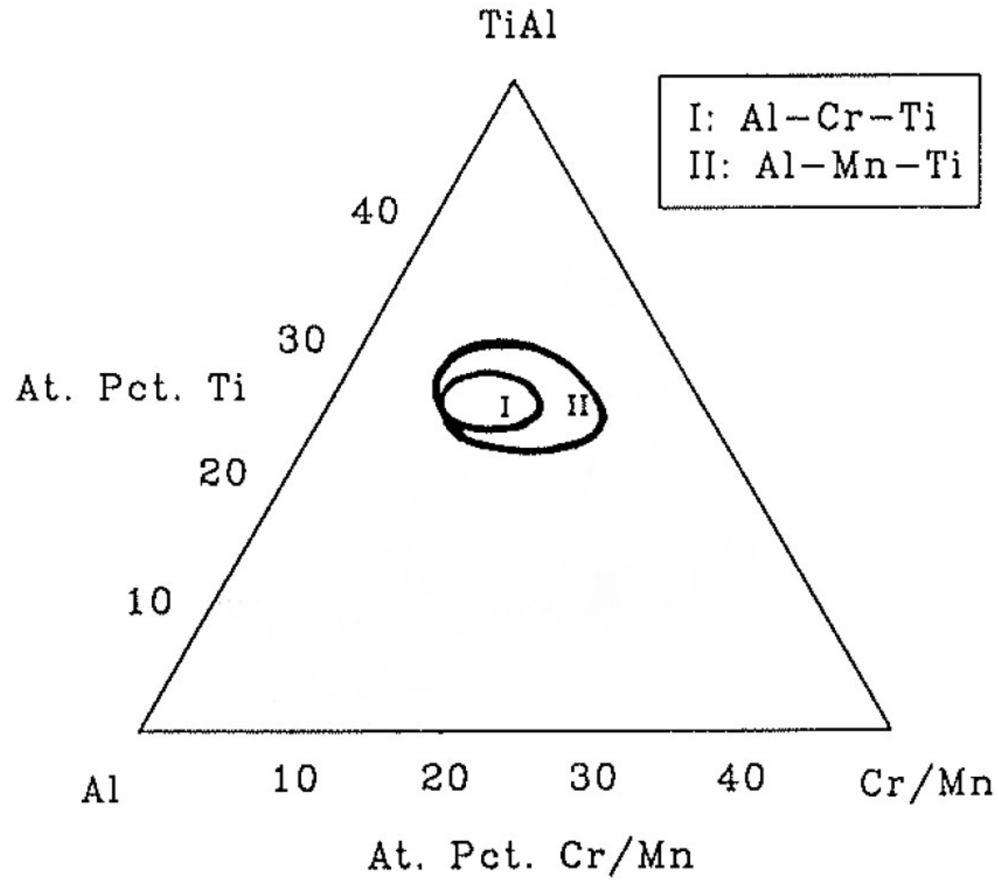

Fig. 2.11: Range of the $L1_2$ structure in the Al-rich corner of the Al-Cr-Ti/Al-Mn-Ti ternary system according to [23]

3 Experimental procedure

3.1 Investigated alloys

In the present diploma thesis Ti-Al alloys with nominal Al content of 62 at.% and additional alloying elements such as Nb, Mo and B were examined to investigate their influence on the microstructural evolution of Al-rich TiAl alloys. Table 3.1 shows the nominal compositions of the studied samples, whereas table 3.2 shows the actual composition of those specimens due to wet chemical analysis. Approximately 2 at.% Al vaporized during the melting process, most probably due to the high temperature necessary to melt the refractory metals. Furthermore, non-negligible impurifications of oxygen were observable. Two different processing routes were chosen to additionally investigate their influences on microstructural formations, herby two nominal compositions were processed via both processing routes to ensure proper comparability. These processing routes were the vacuum arc remelting (VAR) and the crucible-free levitation melting (LM), performed on self-constructed facilities. Cylindrical samples of ten millimeters height were then cut from the melting bulk for further investigation via heat treatments and thermal analysis.

Table 3.1: Nominal compositions of investigated alloys in atomic percent [at.%] and their corresponding processing

Processing	Ti	Al	Mo	Nb	B
VAR	37	62	1	-	-
VAR	35	62	3	-	-
VAR	32.9	62	1	4	0.1
LM	37	62	1	-	-
LM	35	62	3	-	-

Every further composition indication in this work is denoted in atomic percent, and therefore the "at.%"-label will consecutively be skipped. A specimen containing 62 at.% Al and 1 at.% Mo processed via levitation melting (LM) with remaining parts being Ti will be indicated in the following as LM-Ti-62Al-1Mo.

Table 3.2: Actual compositions of investigated alloys in atomic percent [at.%] due to wet chemical analysis and their corresponding designation

Designation	Ti	Al	Mo	Nb	B	O
VAR-Ti-59.8Al-1Mo	39.0	59.8	1.0	-	-	0.2
VAR-Ti-60.3Al-3Mo	36.5	60.3	3.0	-	-	0.2
VAR-Ti-59.8Al-1Mo-3.9Nb-0.03B	35.1	59.8	1.0	3.9	0.03	0.2
LM-Ti-60.4Al-1Mo	38.4	60.4	1.0	-	-	0.2
LM-Ti-60.0Al-3.1Mo	36.7	60.0	3.1	-	-	0.2

3.2 Heat treatments

In order to provide a proper comparison to the binary system various heat treatments were carried out. Table 3.3 contains a list of the performed heat treatments with their corresponding annealing temperature, annealing time and way of cooling afterwards. "WQ" implies water quenching, "FC" stands for furnace cooling. Heat treatments were performed in unaltered furnace air.

Table 3.3: List of performed heat treatments with annealing temperatures, annealing times and the way of cooling

Index	Temperature [°C]	Time [h]	Way of cooling
01	1000	200	WQ
02	800	500	WQ
03	1000	24	WQ
04	800	24	WQ
05	1400	1	FC

Motivation for the long-time annealing heat treatments were a comparison with already performed heat treatments in binary Ti-60Al alloys, whereas the treatments with an annealing time of 24 hours were conducted to investigate kinetics of the transformations. Heat treatment 05 was performed to investigate homogenization of the specimens. All treatments were carried out in an Carbolite RHF 1600 furnace.

3.3 Scanning electron microscopy

The whole range of specimens was investigated in the as-cast state and after the heat treatments via scanning electron microscopy (SEM) to image the generated microstructure. All measurements were performed on a Zeiss EVO50 operating at 15 kV detecting back-scattered electrons (BSE). Additionally, energy dispersive X-ray spectroscopy (EDX) was executed to analyze local chemical compositions. All specimens were grinded and electrolytically polished using an Struers LectroPol-5 operating at 36 V for 25 seconds.

3.4 Electron probe micro analysis

To analyze chemical compositions of phases as well as further investigate the observed microstructure electron probe micro analysis (EPMA) using wavelength dispersive X-ray spectroscopy (WDX) was performed. Investigations were carried out on a JEOL JXA-8100 operating at 15kV and 20nA, herby the pure elements served as standards. All measurements were performed at the Max Planck Institut für Eisenforschung in Düsseldorf.

3.5 X-ray diffraction

X-ray diffraction (XRD) was performed on powders to identify present phases on a Philips PW1830 using a Co x-ray source ($\lambda_{CoK\alpha1}$=1.79*10^{-10}m) operating from 10° to 120° with a step size of 0.02° and 10 seconds per step. Additional measurements were executed on a Bruker D8 Advance utilizing a Cu x-ray source ($\lambda_{CuK\alpha1}$=1.54*10^{-10}m) from 15° to 120° with a step size of 0.02° and 1.2 seconds per step. All samples were rotated.

3.6 Differential thermal analysis

To investigate influences of the additional alloying elements on transition temperatures differential thermal analysis (DTA) on the as-casted specimens was performed. Measurements were taken on Setaram SETSYS-18 in Ar-atmosphere. All samples were heated 3 times with 10 K/min the first and the second time and with 5 K/min for the last time. All measurements were performed at the Max Planck Institut für Eisenforschung in Düsseldorf.

3.7 Differential scanning calorimetry

To further expand the evaluation of transition temperatures of alloyed Al-rich TiAl alloys differential scanning calorimetry (DSC) was performed on a Setaram LABSYS Evo with 10 K/min heating and 40 K/min cooling rate under Argon atmosphere. Samples of about 20 ± 2 milligram were herby placed on sapphire disks to decrease reaction probability of specimens and the Al_2O_3 crucible. Temperature calibration was performed using pure elements of Al, Ag, Au, Cu and Pd according to [26] leading to a temperature accuracy of ± 1K. Experiments were performed on VAR-Ti-59.8Al-1Mo, VAR-Ti-60.3Al-3Mo and VAR-Ti-59.8Al-1Mo-3.9Nb-0.03B in the as-cast and heat-treated states (treatment 01 and 02 from section 3.2). A three-stage heating cycle was performed on all specimens in the DSC device. First, the sample was heated to 900 °C and held for ten hours following cooling down to room temperature. Afterwards the specimen was heated to 1100 °C where it was held for 30 minutes and cooled down again. At last the sample was heated to 1300 °C.

4 Results

4.1 Microstructural characterization

4.1.1 As-cast state

The foundation for proper investigations of the influence from additional elements in metallic alloys is an adequate characterization of their corresponding as-cast state after processing. Figure 4.1 shows the stereo-micrographs of all prepared specimens in their polished state. Whereas on the samples processed with levitation melting (fig. 4.1a and fig. 4.1b) manufacturing related flaws keep within a limit, specimens processed with vacuum arc remelting (fig. 4.1c, fig. 4.1d and fig. 4.1e) show a large amount of macroscopic impairments.

The LM-Ti-60.4Al-1Mo (fig. 4.1a) reveals the least damaged macrostructure. No macroscopic flaws such as cracks or cavities are observable. In addition, the metallographic preparation was comparatively easy. The LM-Ti-60.0Al-3.1Mo (fig. 4.1b) specimen exhibits also a rather unimpaired macrostructure accompanying a large, mostly radial crack running through the center. Preparation was also rather smooth.

On the contrary, all investigated samples processed via VAR reveal a high amount of radial cracks and additional cavities. These specimens already received a high amount of damage via their respective manufacturing process. Given that countless numbers of cracks run in radial direction, high temperature differences between center and surface of the cylindrical bulk during the cooling process can be concluded. Furthermore, shrinkage cavities are present in the centers of every sample.

All three specimens processed with VAR revealed a macrostructure consisting of a crack network lancing the full dimensions of the respective samples. Whereas the VAR-Ti-60.3Al-3Mo (fig. 4.1d) sample shows an accumulation of cracks in radial direction accompanied with tangential cracks, the samples VAR-Ti-59.8Al-1Mo and VAR-Ti-59.8Al-1Mo-3.9Nb-0.03B (fig. 4.1c and fig. 4.1e) reveal a huge deterioration to full extend.

In advance, metallographic preparation of the VAR samples proved to be much more difficult in comparison to its LM counterparts due to very pronounced brittle behaviour of the samples as answer to the grinding resulting in constant fractures and blowouts of small pieces of the disk. The VAR-Ti-59.8Al-1Mo-3.9Nb-0.03B (fig. 4.1e) shows therefore damages along the margin.

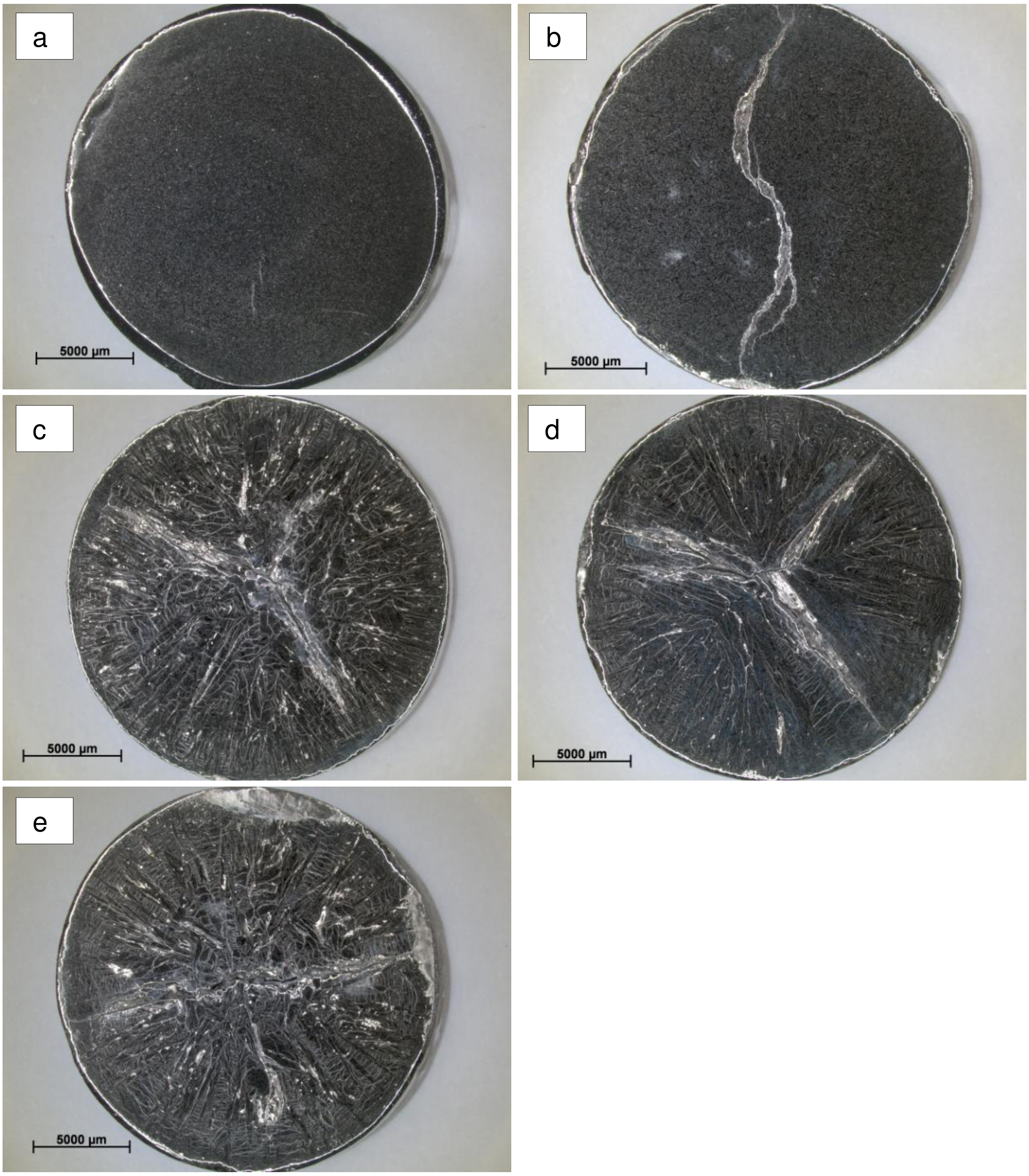

Fig. 4.1: Stereo-micrographs of the as-cast state of the investigated specimens after grinding and polishing for a) LM-Ti-60.4Al-1Mo, b) LM-Ti-60.0Al-3.1Mo, c) VAR-Ti-59.8Al-1Mo, d) VAR-Ti-60.3Al-3Mo and e) VAR-Ti-59.8Al-1Mo-3.9Nb-0.03B. The specimens processed with LM obtain a less damaged surface, whereas the VAR samples show a heavily flawed macrostructure with pronounced crack networks.

To get insights on formed microstructures of the as-casted samples SEM was performed. Figure 4.2 shows the SEM-BSE pictures of all investigated specimens, on which strong segregations and a large share of pores are observable.

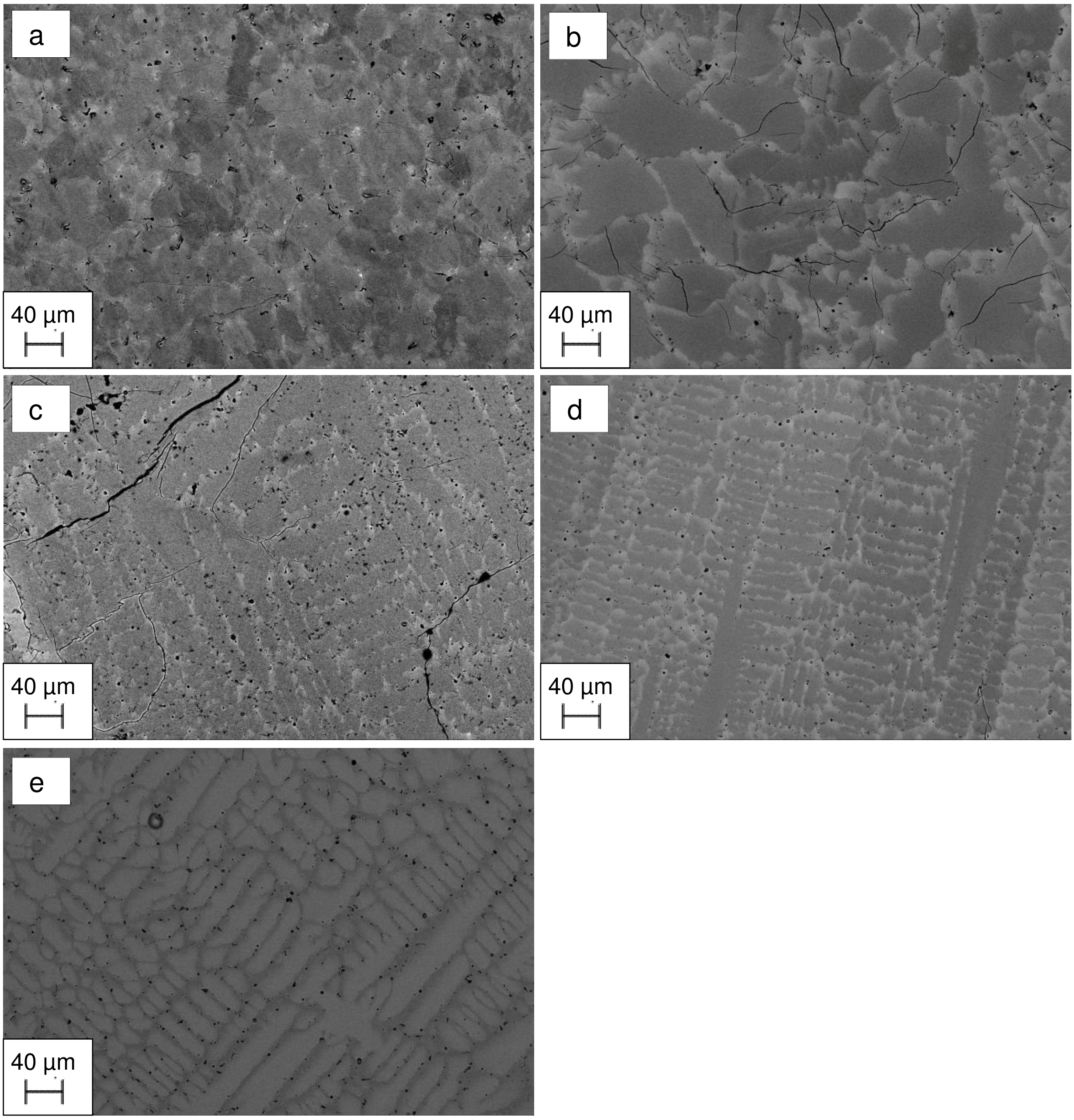

Fig. 4.2: SEM-BSE-micrographs of the as-cast state of the investigated specimens after grinding and polishing for a) LM-Ti-60.4Al-1Mo, b) LM-Ti-60.0Al-3.1Mo, c) VAR-Ti-59.8Al-1Mo, d) VAR-Ti-60.3Al-3Mo and e) VAR-Ti-59.8Al-1Mo-3.9Nb-0.03B. Segregations appear as lighter areas for a)-d) and as darker areas in e). A fine-grained microstructure is observable for the LM-processed samples a) and b), whereas the VAR specimens c), d) and e) obtained dendritic features.

Although the LM-processed alloys revealed a comparably less damaged macrostructure (Fig. 4.1), the SEM-BSE pictures reveal a highly damaged microstructure for all present samples. The LM-Ti-60.0Al-3.1Mo shows a large crack network, whereas the cracks are less frequent in LM-Ti-60.4Al-1Mo, but still observable. Furthermore, a great portion of pores lance the surface, which might be due to an additional leaching effect of the electrolytic polishing, that further increases pore sizes.

Whereas the LM samples show relative fine grains margined with segregations along the grain boundaries, the VAR-specimens reveal highly segregated, dendritic formations which originated from a strong supercooling. Therefore, it is concluded that all present samples are in a state very far from equilibrium.

To analyze the chemical compositions EPMA was performed on these specimens. All of them revealed high impurities of Fe and Ni as well as O, probably stemming from grade 2 Titanium used for the samples [27]. Small, rod-like oxides appearing dark were found in the whole range of samples. LM-Ti-60.4Al-1Mo was strongly contaminated and therefore only qualitatively analyzed, the remaining specimens were quantitatively investigated with 3 to 6 measurements per zone. Figure 4.3 shows the BSE micrograph for the LM-Ti-60.4Al-1Mo (fig. 4.3a) along with the observed spectrum for the brighter areas (fig. 4.3b). The segregations align in lines and therefore the observed microstructure differs from the observed one in figure 4.2a. Given that the EPMA specimens are taken from a different area of the bulk, a differing microstructure along the bulk can be concluded. As shown in figure 4.3b, the segregated areas consist of enrichments of Fe, whereas the oxides contain Al and Ti additionally to O. Small to no intensities for Mo were observed via the measurement.

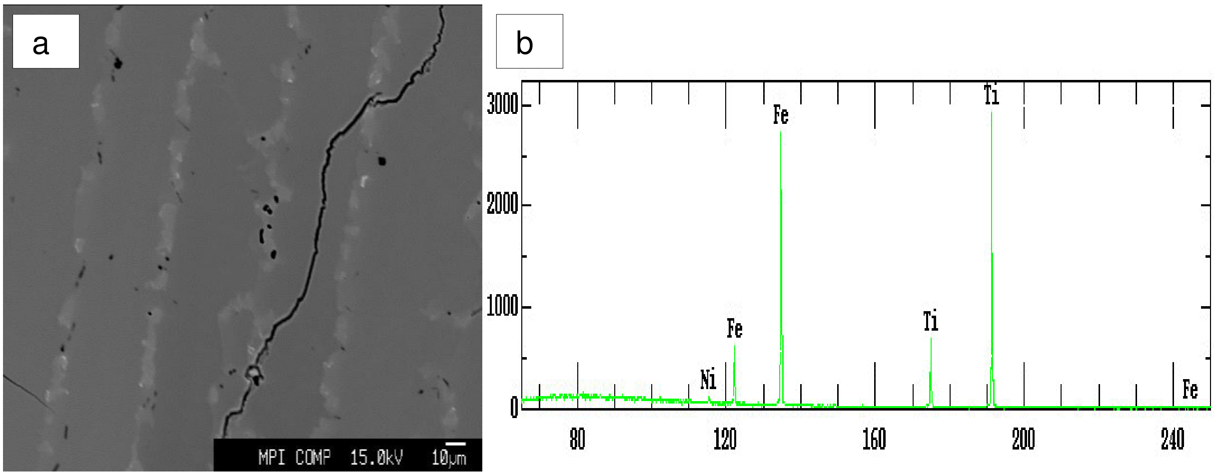

Fig. 4.3: BSE micrograph of LM-Ti-60.4Al-1Mo (fig. 4.3a) and the spectrum for the brighter, linear shaped areas revealing enrichments of Fe (fig. 4.3b)

For VAR-Ti-59.8Al-1Mo on the other hand, the segregations contain up to 1.2 % Mo and a higher amount of Al of about 63.2 %, whereas the dimmer sections only hold up to 0.1 % Mo and 60.4 % Al (fig. 4.2c), but a larger Ti content. Furthermore, some very light spots contain high amounts of Fe (up to 1.5 %), Mo (up to 1.3 %) and Ni (up to 1.2 %). Impurities such as Fe and Ni therefore seem to cluster in small areas.

Though the microstructure for LM-Ti-60.0Al-3.1Mo and VAR-Ti-60.3Al-3Mo is highly different (fig. 4.2b and fig. 4.2d), both specimens show similar results throughout the EPMA investigation. Segregations with high amounts of Mo (3.9 % for the LM and 4.2 % for the VAR sample) and higher Al amounts (62.5 % for LM and 61.9 % for VAR) accompany dimmer areas containing much smaller amounts of Mo (LM: 1.9 %; VAR:1.6 %) and also less Al (LM: 61.9 %; VAR: 60.5 %). In direct comparison, the segregation degree is therefore somewhat higher within the VAR specimens. Furthermore, rod-shaped oxides could be observed additionally to clusters containing high amounts of Mo, Fe and Ni (LM: 5.6 % Mo, 1.7 % Fe, 0.5 % Ni; VAR: 2.9 % Mo, 1.5 % Fe, 1.5 % Ni). Fe and Ni were not observed elsewhere.

Due to the high amount of Nb alloyed within the VAR-Ti-59.8Al-1Mo-3.9Nb-0.03B the SEM-BSE pictures show a reversed result with segregations appearing darker than their surroundings. EPMA revealed that despite the Mo actually segregates to a large extend, the reason is the high amount of Nb solidifying within the dendrites and therefore causing the reversed contrast. Figure 4.4 shows the BSE recording of the VAR-Ti-59.8Al-1Mo-3.9Nb-0.03B specimen.

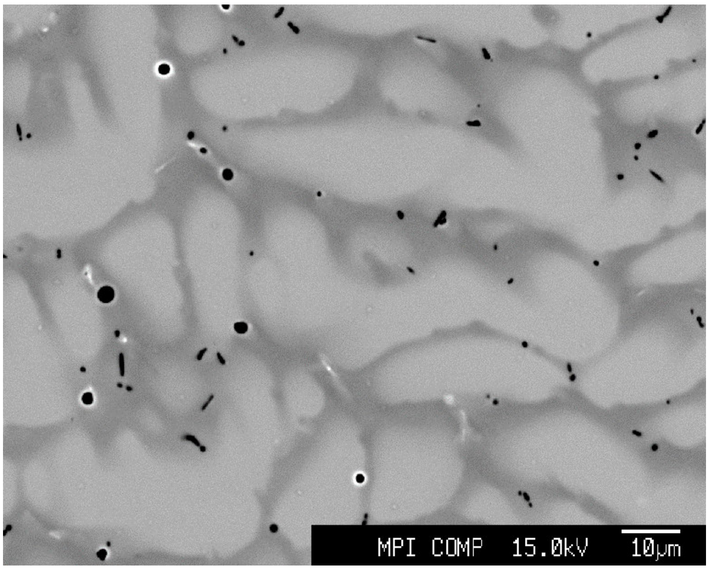

Fig. 4.4: BSE picture of VAR-Ti-59.8Al-1Mo-3.9Nb-0.03B revealing dark segregations, oxides and bright clusters.

The segregations along the grain boundaries show a larger Al content (63.4 %), similar to the other, quantitatively investigated samples. Furthermore, 2 % Mo and 2 % Nb were found in the segregated zone, as well as small amounts of Fe (0.2 %) and Ni (0.05 %). No B was observable within the segregation as well as no grain fining effect stemming from B enrichment at grain boundaries. The inner grains actually offer a range of different compositions, varying from 0.0 to 0.7 % Mo, 2.6 to 4.6 % Nb and 60.9 to 62.0 % Al. Also, up to 0.01 % B was observable within the grains in the brighter zones. As shown in figure 4.4, some very bright spots could be investigated containing relatively high amounts of Fe (1.0 %) and Ni (0.6 %), as well as 0.3 % Mo, 3.3 % Nb and 0.7 % B. Furthermore, in addition to the pervasive oxides, borides could be observed, though there a none in figure 4.4. The borides contained up to 21.4 % B, in addition to 48.4 % Al as well as small amounts of Mo (1.7 %), Nb (1.5 %), Fe (0.2 %) and Ni (0.1 %).

Due to the XRD-investigations the present phases could be qualitatively identified as γ-TiAl accompanied by shares of h-$TiAl_2$, which is however not observable in any of the SEM-BSE pictures. A possible explanation could be a missing contrast due to the very similar nominal compositions of γ-TiAl and h-$TiAl_2$ relatively to highly segregated zones containing large amounts of heavy refractory metals.

Figure 4.5 shows the diffraction pattern of VAR-Ti-59.8Al-1Mo in its as-cast state measured with a CoKα anode. The γ-TiAl and h-$TiAl_2$ diffraction peaks cover the range completely and therefore it is concluded, that the as-cast state consists of a γ-TiAl matrix accompanied by the metastable h-$TiAl_2$. Slight shift in terms of Peak angle (2θ) of the measured interferences might be due to the inclusion of additional alloying elements within the γ-TiAl matrix. Furthermore, the inhomogeneous distribution of these within the sample powder based on the segregated state, which might further blur the diffraction recording.

All investigated specimens shared the same XRD results. In their as-cast state, all microstructures qualitatively consist of a γ-TiAl matrix with shares of the metastable h-$TiAl_2$ phase, which can be identified either by its characteristic superlattice diffraction peaks or, alternatively, its different intensity sequence to γ-TiAl and r-$TiAl_2$ at the double peaks (~53°, ~78° and ~95° 2θ).

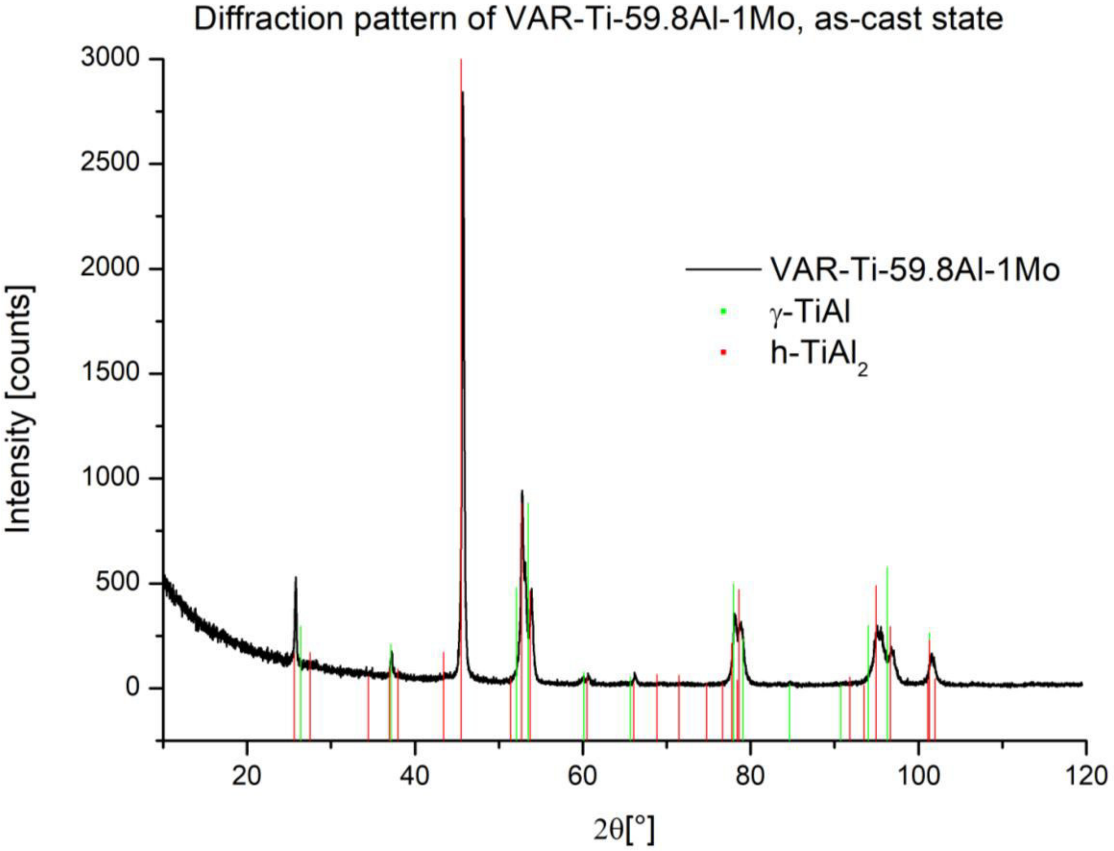

Fig. 4.5: Diffraction pattern of VAR-Ti-59.8Al-1Mo in its as-cast state measured with CoKα. The respective diffraction peaks of γ-TiAl (green) and h-$TiAl_2$ (red) are indicated.

Hereby the as-cast state summarizes as follows: The whole range of specimens show impairments in form of cracks and crack-networks stemming from the cooling process in addition to contamination with Fe, Ni and O possibly due to the usage of grade 2 Titanium. The levitation melted samples obtained a relative fine-grained microstructure during processing, whereas the vacuum arc remelted ones resulted in coarsely-grained, dendritic structures. SEM investigations revealed segregations in all the samples containing the largest share of Mo and a higher content of Al. The LM-Ti-60.4Al-1Mo is extraordinarily strong contaminated with Fe, Ni and O and was therefore not quantitatively investigated. Contrary to the other samples, Fe was found in the segregated areas. In all other samples Fe and Ni were almost only found in local clusters and did not solve in the matrix. Whereas Mo tended to segregate, Nb leaned to solve within the dendrites and therefore the BSE-contrast was reversed for the Nb-alloyed specimen. Oxides were found in all samples, as well as a large share of pores. In the VAR-Ti-59.8Al-1Mo-3.9Nb-0.03B sample no grain-fining effect due to

B can be observed, especially because the main portion of B is not present within the segregations. Phases were identified as γ-TiAl with additional h-$TiAl_2$ via XRD measurements.

Note: Most of the observed Al-values are in fact higher than the corresponding Al content in the whole sample. This might be due a relatively low amount of measuring points (three to six) and therefore these values should be considered rather as trend values than absolute ones.

4.1.2 Heat-treated state: 1000 °C / 200 h / WQ

The following results show the microstructural evolution of samples annealed at 1000 °C for 200 h followed by water quenching to properly freeze the elevated temperature condition. Special attention was given to an appropriate comparison to the binary system undergoing similar heat treatments. Figure 4.6 shows SEM-BSE micrographs for the five investigated alloy compositions.

All detected microstructures consist of γ-TiAl, which appears brighter in the BSE-micrographs due to larger amounts of the additional, heavy elements Mo and Nb, and r-$TiAl_2$, which appears dimmer due to the higher Al content. The samples containing LM-Ti-60.4Al-1Mo (fig. 4.6a) and VAR-Ti-59.8Al-1Mo (fig. 4.6c) revealed lamellar microstructures as established in [5], whereas the specimens LM-Ti-60.0Al-3.1Mo (fig. 4.6b), VAR-Ti-60.3Al-3Mo (fig. 4.6d) and VAR-Ti-59.8Al-1Mo-3.9Nb-0.03B (fig. 4.6e) received plate-formed, hastate like shards of r-$TiAl_2$, known from similar heat treatments executed on binary TiAl alloys containing 60 at.% Al [19]. Due to the water quenching, the heat treatment nucleated several cracks and fissures. Structural damages due to rapid cooling can be identified via the fact that no r-$TiAl_2$ surrounds the crack areas, though they should nucleate more easily at free surfaces due to higher diffusion rates if the crack was already present during the annealing. All specimens show cracks based on water quenching, though the LM-Ti-60.4Al-1Mo is least affected.

The LM-Ti-60.4Al-1Mo specimen shows a fully lamellar microstructure (fig. 4.6a) and up to no originally segregated areas are observable in the SEM-BSE micrograph. Some extended areas of r-$TiAl_2$ are also detectable. These appear as granular r-$TiAl_2$ especially around grain boundaries, but a fully lamellar structure is still achieved via the heat treatment. This sample also appears to be the closest one to equilibrium state.

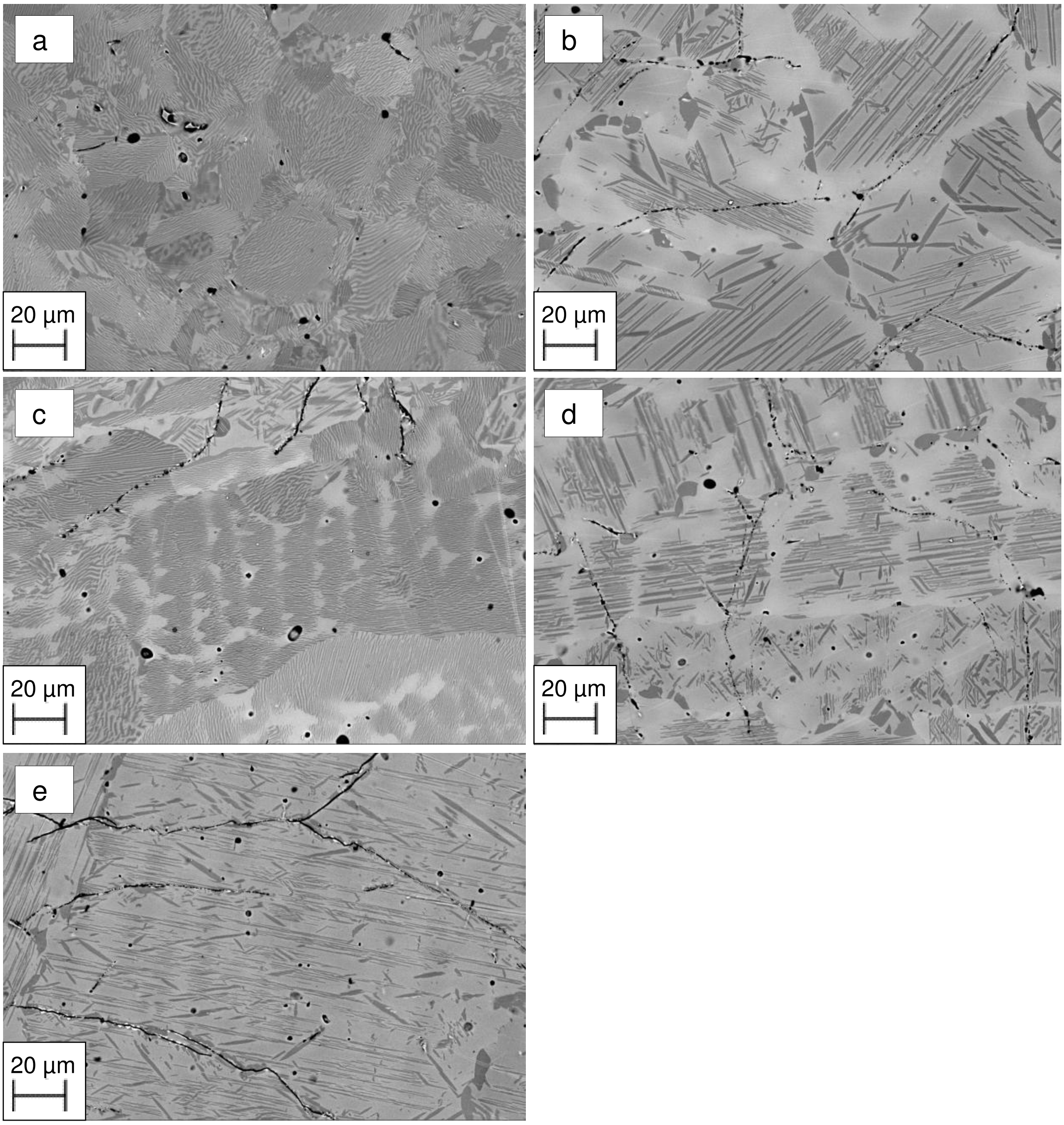

Fig. 4.6: SEM-BSE-micrographs for a) LM-Ti-60.4Al-1Mo, b) LM-Ti-60.0Al-3.1Mo, c) VAR-Ti-59.8Al-1Mo, d) VAR-Ti-60.3Al-3Mo and e) VAR-Ti-59.8Al-1Mo-3.9Nb-0.03B containing γ-TiAl (bright areas) and r-$TiAl_2$ (dim areas) after annealing at 1000 °C for 200 h following water quenching. The samples containing nominally 1 % Mo a) and c) revealed a lamellar microstructure, whereas higher alloyed samples in b), d) and e) show plate-like microstructures with smaller ratios of r-$TiAl_2$. Newly nucleated cracks are observable as well as traces of the as-cast microstructure; b) and d) reveal pronounced remains of the segregations of the as-cast state.

The sample containing VAR-Ti-59.8Al-1Mo (fig. 4.6c) reveals a partly similar microstructure. Although the lamellar microstructure of γ-TiAl and r-$TiAl_2$ is observable, traces of the original dendritic microstructure and its segregations are still detectable. Therefore, it is interpreted, that further annealing time in addition to 200 hours would be necessary to reach a desired equilibrium state. Furthermore, zones with large globular r-$TiAl_2$ precipitations as in the LM-Ti-60.4Al-1Mo specimen can be observed.

The specimens containing nominal contents of 3 % Mo (fig. 4.6b and fig. 4.6d) show similar results after the corresponding heat treatment. Both reveal γ-TiAl grains with plates of r-$TiAl_2$ surrounded by segregations containing high amounts of Mo as well as several granular r-$TiAl_2$ precipitations. The segregated areas remaining from the as-cast state are still highly pronounced, annealing at 1000 °C for 200 hours does clearly not achieve an equilibrium state for these samples.

The highly alloyed VAR-Ti-59.8Al-1Mo-3.9Nb-0.03B on the other hand shows no segregated areas, and its plate-like formations of r-$TiAl_2$ in γ-TiAl appear to be fine grained in comparison to VAR-Ti-60.3Al-3Mo and LM-Ti-60.0Al-3.1Mo. No segregations are observable, though coarse-grained r-$TiAl_2$ around cracks and grain boundaries is shown.

Figure 4.7 shows the XRD pattern for LM-Ti-60.4Al-1Mo (fig. 4.7a) and VAR-Ti-60.3Al-3Mo (fig. 4.7b) after 1000 °C / 200 h / WQ measured with a CoKα source. The diffraction peaks for the Al-rich phases are marked. As shown in figure 4.6, all microstructures consist of γ-TiAl and r-$TiAl_2$ with diverging proximity to an equilibrium state. The diffraction patterns herby report that those microstructures are in fact γ-TiAl + r-$TiAl_2$, but in addition, h-$TiAl_2$ is still present in all 5 alloy compositions because the superlattice diffraction peaks are still present. This fact exaggerates the assumption that none of the investigated samples has reached an equilibrium state yet. Although VAR-Ti-60.3Al-3Mo revealed the double peak intensity sequence matching to γ-TiAl and r-$TiAl_2$, a characteristic h-$TiAl_2$ peak at around 51° could have been observed.

To further investigate the chemical distribution of Al and Mo in the samples with conditions very far from equilibrium, EDX-mappings were produced. Figure 4.8 shows the results for the LM-Ti-60.0Al-3.1Mo specimen with the SEM-BSE micrograph (fig. 4.8a) and the respective mappings for Al (fig. 4.8b), Ti (fig. 4.8c) and Mo (fig. 4.8d). Higher color intensities indicate a higher count number and therefore a higher amount of the corresponding element in that specific area.

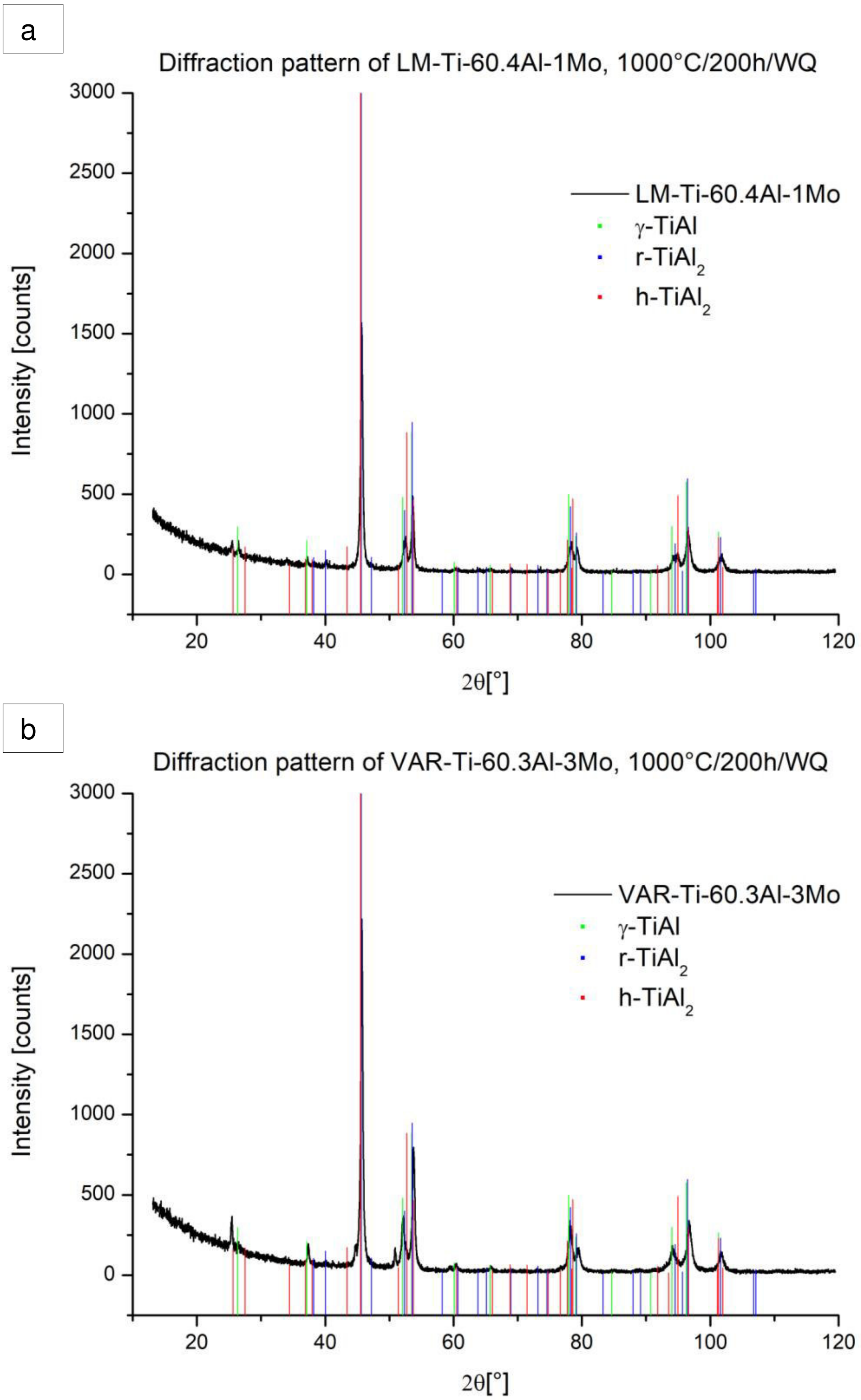

Fig. 4.7: XRD pattern for a) LM-Ti-60.4Al-1Mo and b) VAR-Ti-60.3Al-3Mo after 1000 °C / 200 h / WQ measured with CoKα. The respective diffraction peaks of γ-TiAl (green), r-$TiAl_2$ (blue) and h-$TiAl_2$ (red) are indicated.

The SEM-BSE micrograph (fig. 4.8a) shows grains of γ-TiAl with plates of r-$TiAl_2$ surrounded by the remains of the segregations stemming from processing. Figure 4.8b indicates the mapping for Al, which reveals, as expected, high Al contents in the Al-rich r-$TiAl_2$ phase, but no extensive chemical differences between the grain interior γ-TiAl and the γ-TiAl along grain boundaries containing large shares of Mo. The mapping for Ti (fig. 4.8c) reveals no obvious preferences, whereas missing tendency of the sample for the formation of precipitations at the still segregated, high Mo containing areas framing the grains is immediately observable from the Mo mapping (fig. 4.8d). Therefore, it is concluded, that the high amounts of Mo in certain areas of the LM-Ti-60.0Al-3.1Mo specimen suppressed the formation r-$TiAl_2$ during the heat treatment, or at least, precipitations of the Al-rich r-$TiAl_2$ preferably took place at areas containing comparatively lower amounts of Mo. Furthermore, the r-$TiAl_2$ contains the least portions of Mo. The VAR-Ti-60.3Al-3Mo sample showed similar results via the WDX-mapping.

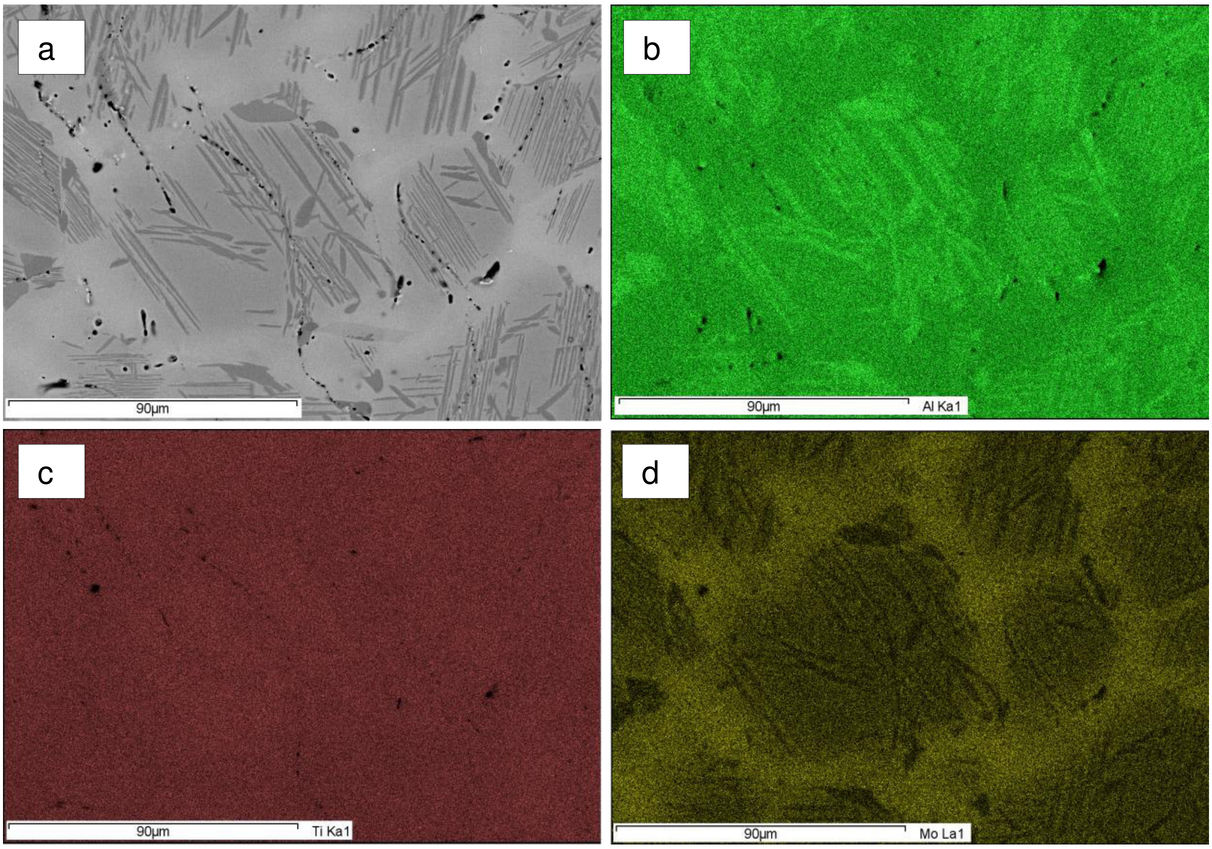

Fig. 4.8: WDX-mapping for LM-Ti-60.0Al-3.1Mo after 1000 °C / 200 h / WQ consisting of a) SEM-BSE micrograph, b) mapping for Al with high amounts in the Al-rich r-$TiAl_2$, c) mapping for Ti with no specific preferences observable and d) mapping for Mo showing enrichment along the original segregations with almost no precipitations. The recorded spectral lines are indicated in the inset.

To gain further information on the chemical distribution in the annealed samples, EPMA investigations were performed. In the as cast state the LM-Ti-60.4Al-1Mo specimen revealed large portions of impurities and only small traces of Mo, which lead to the conclusion of a strongly inhomogeneous distribution of alloying elements across the bulk material. The quantitative EPMA showed also for the heat-treated state of 200 hours at 1000 °C followed by water quenching only very small shares of Mo contents up to 0.43 at.% in the brighter areas containing γ-TiAl and no shares of Mo were found in the dimmer r-$TiAl_2$ (fig. 4.6a). Mo could not be detected in all γ-TiAl measurement spots. As expected, the r-$TiAl_2$ reveals larger portions of Al and smaller shares of Ti than the γ-TiAl. Furthermore, impurities of Fe were measured in all spots, ranging from 0.41 at.% up to 1.04 at.%. The content of Fe in the r-$TiAl_2$ is in the range of 1.0 at.%, whereas the γ-TiAl only revealed shares of about 0.5 at.%, which is the opposite behaviour of the Mo.

On the contrary, the sample VAR-Ti-59.8Al-1Mo showed only small portions of Fe impurities averaging 200 ppm, no Ni was observed. No preference trends in Fe whereabouts where observable. Furthermore, the measured share of Mo was higher than the amounts of the LM-Ti-60.4Al-1Mo alloy. Though no Mo was found in the r-$TiAl_2$, the brighter γ-TiAl included an average of 0.57 at.% ranging up to 1.05 at.%. As within the previous sample, the measured Mo content is lower than the values estimated with wet chemical analysis. Strong inhomogeneity across the bulk material might be a possible explanation for measured Mo contents lower than estimated. As expected, the γ-TiAl included smaller shares of Al and higher contents of Ti. Two measurements across 10 µm circular spots revealed only very small Mo portions within the fine lamellar structures of γ-TiAl and r-$TiAl_2$ of 0.15 at.% and 0.11 at.%, whereas the larger γ-TiAl areas occurring within the microstructure contain the larger shares of Mo. Therefore, it is concluded, that only locally small Mo contents lead to lamellar microstructures of this kind and Mo diffusion has to take place in before appropriate phase transition happens. Figure 4.9 shows the BSE micrograph of the VAR-Ti-59.8Al-1Mo specimen with the position of the two 10 µm areas and four spot points. One of the grain interiors shows a microstructure where the transformation is not finished, and therefore the specimen has not reached an equilibrium state after 200 hours at 1000 °C yet as already proposed by XRD. The two large, white areas are impurifications with copper from preparation; they did not impair the EPMA on the sample surface itself.

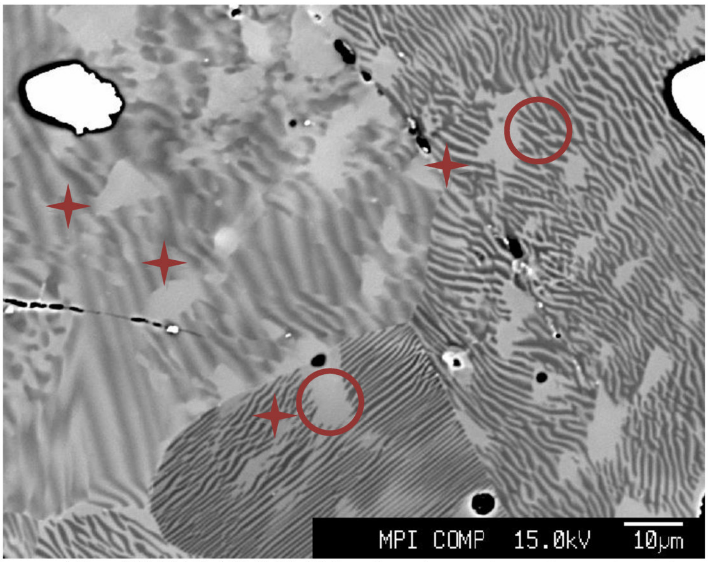

Fig. 4.9: BSE picture of the VAR-Ti-59.8Al-1Mo showing a lamellar microstructure of γ-TiAl and r-$TiAl_2$. Several spots and areas for the EPMA are marked. The microstructure on the upper left corner proves that the specimen has not yet reached an equilibrium state. Two large, white contaminations of copper stemming from the preparation are observable that did not impair the measurement.

The specimens with nominal 3 at.% Mo revealed once more similar results. LM-Ti-60.0Al-3.1Mo and VAR-Ti-60.3Al-3Mo showed comparatively small contaminations with Fe of around 500 ppm and 200 ppm. Furthermore, the sample processed via levitation melting also contains around 100 ppm Ni impurities. Previous SEM-BSE investigations revealed a highly segregated microstructure with the inner grain areas containing less Mo developing two-phase microstructures of γ-TiAl and r-$TiAl_2$. plates and the margins of the grains with high contents of Mo and scarce, granular r-$TiAl_2$. Throughout the EPMA it gets clear once more, that the specimens are both far from an equilibrium state.

The samples show a large range of observable Mo contents within the brighter, γ-TiAl areas (60.84 at.% Al and 36.34 at.% Ti) from 1.5 at.% to 3.6 at.%, depending on the measurement spot within the segregated areas. Contrary to the previous samples, where no Mo soluded within the r-$TiAl_2$ (65.02 at.% Al and 34.01 at.% Ti), the r-$TiAl_2$ does contain up to 1.1 at.% Mo. The Mo shares within the granular $TiAl_2$ at the grain boundary are averaging 0.88 at.%, whereas the needles contain around 0.72 at.%. The uneven distribution of the Mo within the γ-TiAl furthermore proves that an equilibrium state is not yet reached. Figure 4.10 shows the BSE micrograph of VAR-Ti-60.3Al-3Mo showing γ-TiAl and r-$TiAl_2$-plates as well as 3 marked circles for 10 µm EPMA spot measurements. Across the spots Mo averaged 2.3 at.%, ranging from 2.22 at.% to 2.47 at.%. The average Mo share therefore within areas of γ-TiAl and plates of r-$TiAl_2$ is lower than the absolute content of Mo within the VAR-Ti-60.3Al-3Mo specimen.

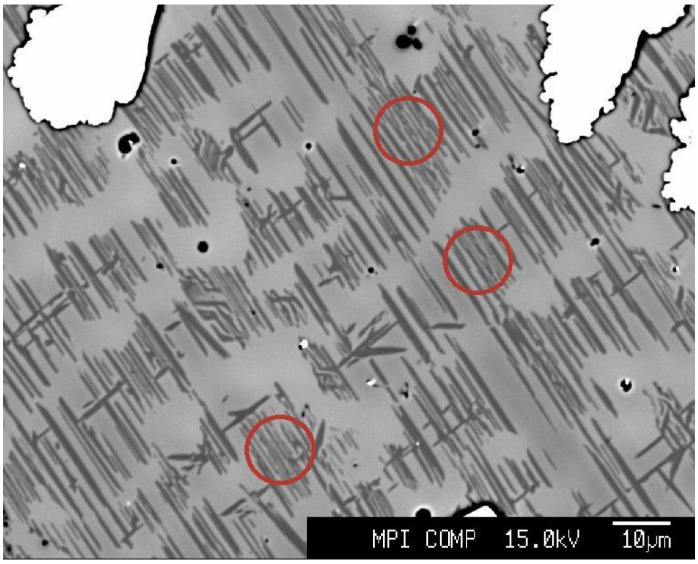

Fig. 4.10: BSE micrograph of VAR-Ti-60.3Al-3Mo showing γ-TiAl (light areas) and r-$TiAl_2$ (dim plates). White flakes in the top stem from preparation and did not impair the EPMA measurement. Three spots for 10µm spot measurements are marked.

To further visualize the uneven distribution of Mo across the material and especially within large domains of γ-TiAl, EPMA line measurements were performed. Figure 4.11a shows the SE micrograph for VAR-Ti-60.3Al-3Mo in complement to figure 4.11b, which shows the BSE micrograph of the same area. The measured line is marked accordingly and visible in the SE picture. Figure 4.11c reveals the results of the line measurement for Al, Ti and Mo aligned to the micrographs above. Whereas the alternating Mo, Al and Ti values corresponding to previous EPMA measurements within the γ-TiAl and r-$TiAl_2$ areas are clearly observably along the line, the Mo share increases gradually within the larger γ-TiAl domain. Along the far-right edge of the line scan Mo shares drop and Al shares increase again. The stable r-$TiAl_2$ preferably seems to form in areas containing a relatively small share of Mo, or, at least, a small share of Mo is necessary locally to allow the phase transition to r-$TiAl_2$. Although the observed Mo share within the r-$TiAl_2$ plates is comparatively small it does not equal zero, contrary to the samples containing nominally 1 at.% Mo.

The additional specimen VAR-Ti-59.8Al-1Mo-3.9Nb-0.03B showed a previously reversed behaviour contrary to the other samples in terms of contrast due to Nb predominantly solidifying within the dendrites. The EPMA revealed a lower content of refractory metals within the plate-like r-$TiAl_2$ similar to previous results in this thesis. The r-$TiAl_2$ (65.43 at.% Al, 31.90 at.% Ti) contained on average 2.62 at.% Nb, whereas the γ-TiAl (61.27 at.% Al, 34.35 at.% Ti) averaged 4.35 at.% Nb.

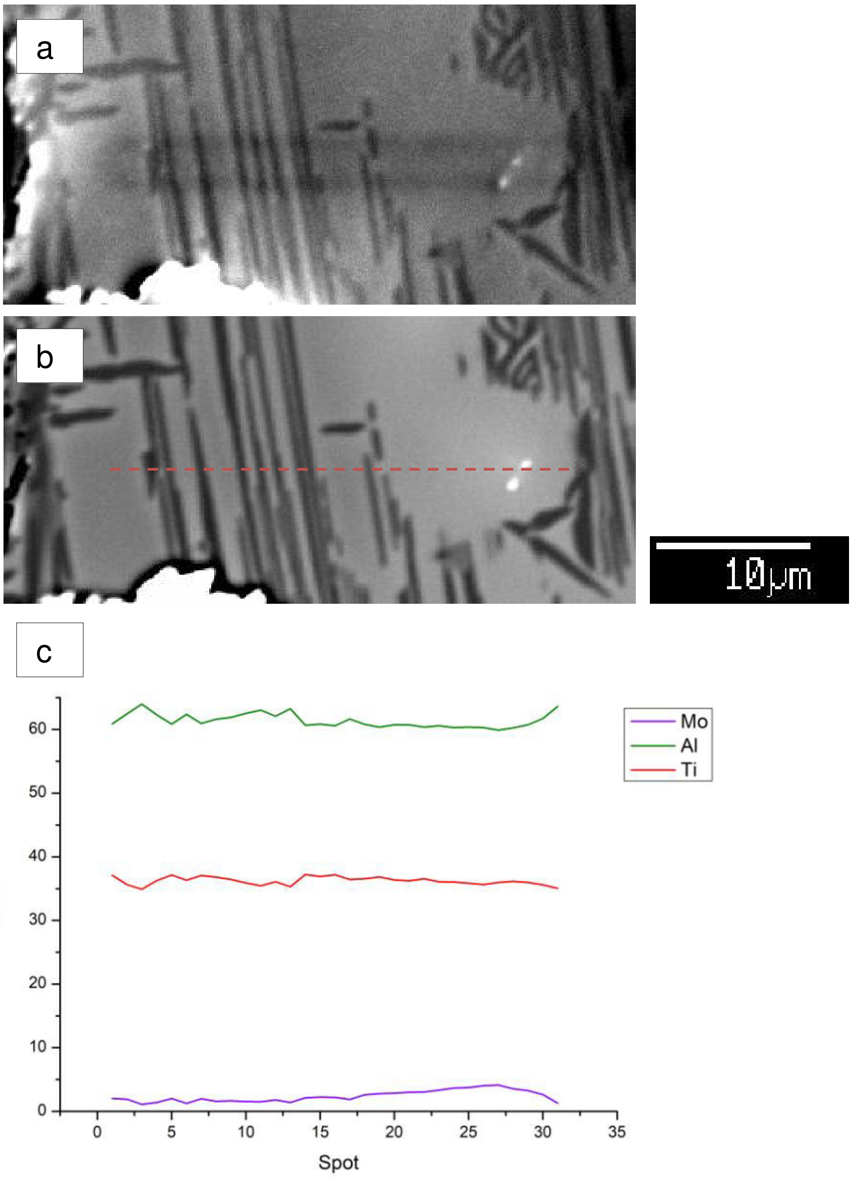

Fig. 4.11: EPMA line measurement of VAR-Ti-60.3Al-3Mo consisting of a) SE micrograph, b) BSE micrograph and c) Mo, Al and Ti values in at.% of the corresponding measurement spots. The graph was aligned to fit to the micrographs properly.

Furthermore, impurities of Fe could be detected all across the specimen, 216 ppm on average for γ-TiAl and 475 ppm for r-$TiAl_2$. This behaviour seems similar to results of the highly Fe polluted LM-Ti-60.4Al-1Mo, which contained the double amount of Fe within the r-$TiAl_2$ than the γ-TiAl. Additionally, though the wet chemical analysis previously resulted in 1 at.% Mo across the alloy, no measurement spot except one for each phase amounted a Mo containment, which were only in 100 to 200 ppm range. Furthermore, additional areas of the sample were found where segregated areas were still largely pronounced and the sample locally kinetically farer from equilibrium, contrary to previous measurements using SEM where no such areas were observable.

Figure 4.12 shows the BSE micrograph of these local area. The large white flakes again stem from preparation and did not impair the EPMA measurement. In Addition, globular r-$TiAl_2$ was observable along the grain boundary area which is accompanied by clusters containing large shares of refractory alloying elements. 0.97 at.% Mo and 6.97 at.% Nb were observable within these clusters as well as 782 ppm Fe. An additional measurement within the segregation revealed 967 ppm Mo and 3.21 at.% Nb (a value in-between the γ-TiAl and the r-$TiAl_2$ values).

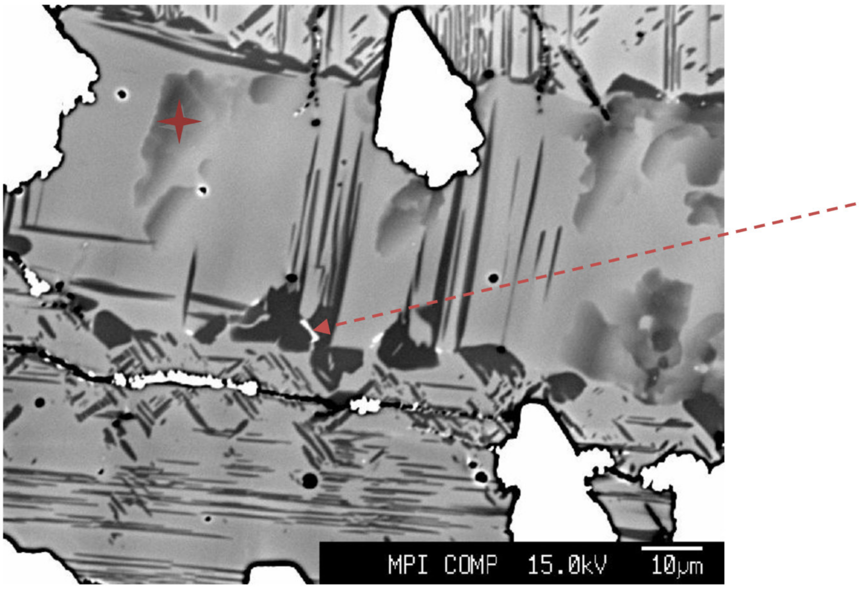

Fig. 4.12: BSE picture of the VAR-Ti-59.8Al-1Mo-3.9Nb-0.03B after 1000 °C / 200 h / WQ showing segregations as in the as-cast state, γ-TiAl (light) and r-$TiAl_2$ (dim). Globular r-$TiAl_2$ formed along the grain boundary, accompanied by clusters containing large shares of refractory elements (very bright spots). The EPMA measurement spots are marked accordingly.

4.1.3 Heat-treated state: 1000 °C / 24 h / WQ

To obtain insights on kinetics of the transformation processes occurring within alloyed Al-rich TiAl alloys, the heat treatment examined in section 4.1.2 was repeated with a change in the annealing time from 200 to 24 hours. Figure 4.13 shows SEM-BSE pictures recorded from all specimens after grinding and electrolytic polishing. All shown images in figure 4.13 reveal microstructures very far from equilibrium.

The LM-Ti-60.4Al-1Mo (fig. 4.13a) herby is the specimen revealing a microstructure that is closest to an equilibrium state. Despite the lamellae show a rather fine state compared to the result after annealing for 200 hours in section 4.1.2, no segregations are observable. Though on the micrograph of the VAR-Ti-59.8Al-1Mo (fig. 4.13c) also a lamellar microstructure is observable, the latter shows distinct remains of the segregated areas from processing. As shown in section 4.1.2, within the LM-Ti-60.4Al-1Mo specimen only small amounts of Mo were detected via EPMA, whereas a much larger fraction of Fe could be observed enriching in the segregations. Actually, Fe might be a larger driving force for the current microstructural evolution than Mo, especially if the contamination with Fe surpasses the actual Mo content, as suggested due to the EPMA results. Furthermore, contrary the other specimens, the segregated areas mainly contained Fe instead of Mo in the as-cast state (see section 4.1.1). This might result in more accelerated transformation kinetics if the Fe possesses better diffusion properties and therefore an advanced transformed microstructure in comparison to a specimen alloyed with Mo. In any case, the contamination with large amounts of Fe appears to rather offer additional insights on transformation kinetics than impeding proper investigation.

The samples LM-Ti-60.0Al-3.1Mo and VAR-Ti-60.3Al-3Mo (fig. 4.13b and 4.13d) reveal a similar microstructure of the as-cast state (γ-TiAl with segregation of Mo) accompanied by plates of r-$TiAl_2$ in the grain interior. No r-$TiAl_2$ shards were found within the segregations. The microstructure appears to be far less advanced in comparison to the alloys with nominal content of 1% Mo.

The VAR-Ti-59.8Al-1Mo-3.9Nb-0.03B (fig. 4.13e) shows a similar picture of the as-cast state of darker segregations (due to the fact that Nb does not segregate) accompanied by plate-like structures of r-$TiAl_2$. However, the r-$TiAl_2$ seems to be more likely to form within the segregated areas containing higher Mo levels but an overall smaller share of refractory alloying elements, though precipitations can be observed on either part of the microstructure.

All investigated alloys reveal several pores and cavities as well as cracks stemming from the water quenching due to the high cooling rate. These cracks can be identified due to the missing precipitations at the crack surfaces.

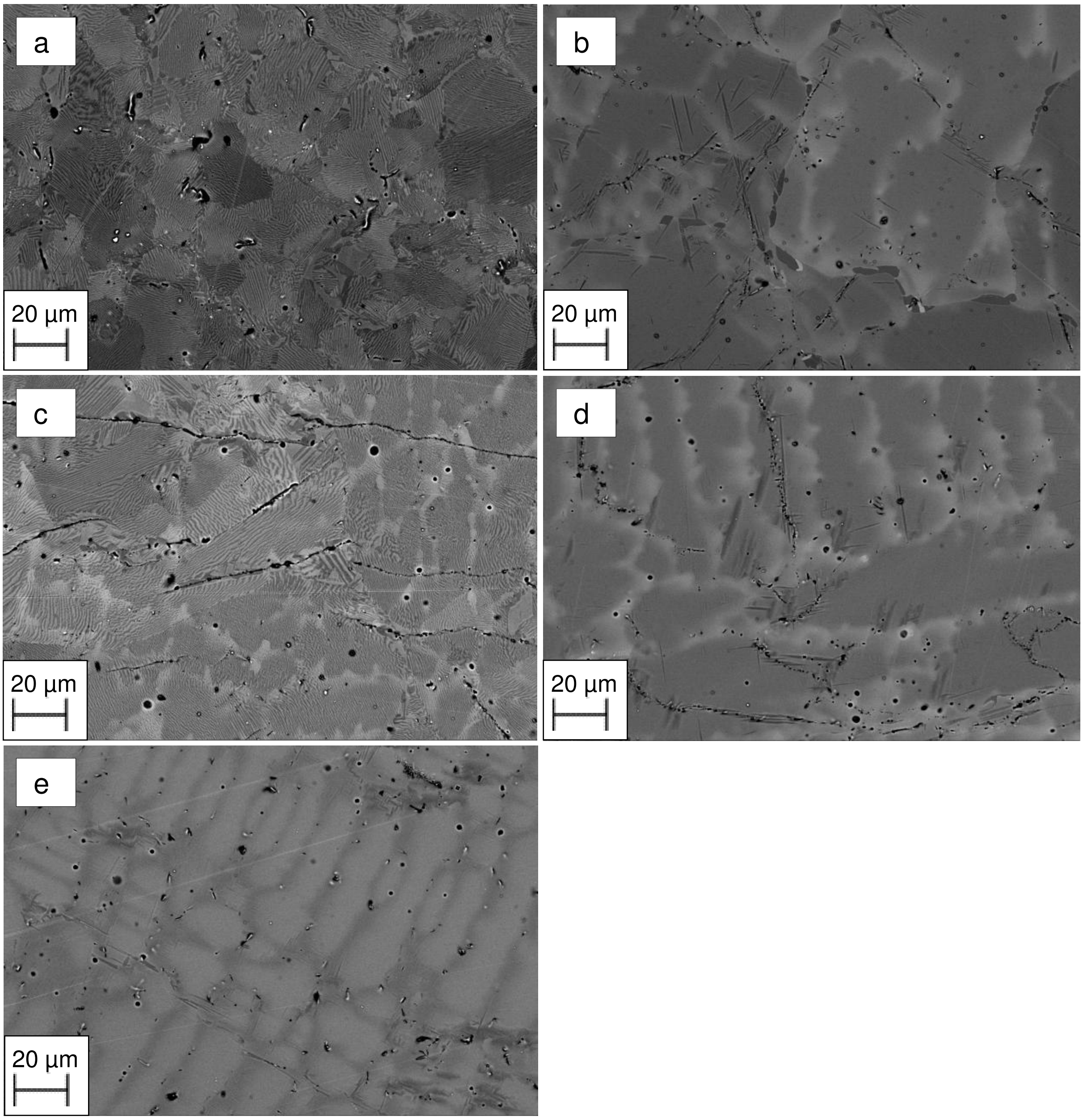

Fig. 4.13: SEM-BSE micrographs of a) LM-Ti-60.4Al-1Mo, b) LM-Ti-60.0Al-3.1Mo, c) VAR-Ti-59.8Al-1Mo, d) VAR-Ti-60.3Al-3Mo and e) VAR-Ti-59.8Al-1Mo-3.9Nb-0.03B after 24 hours at 1000 °C followed by water quenching; a) and c) show lamellar microstructures of γ-TiAl and r-$TiAl_2$ with traces of segregations, whereas b), d) and e) show the as-cast state with a small amount of r-$TiAl_2$ plates.

4.1.4 Heat-treated state: 800 °C / 500 h / WQ

In order to further compare the microstructural evolution of alloyed Al-rich TiAl alloys to its binary counterparts all specimens were annealed at 800 °C for 500 hours followed by water quenching. As known from investigations of the binary system, a specimen of Ti-60Al heat-treated with 800 °C for 500 hours followed by water quenching obtained a tweed-like microstructure of γ-TiAl + Ti_3Al_5 [20]. Figure 4.14 shows the SEM-BSE images of all investigated alloys after the previously mentioned heat treatment. None of them reveal tweed-like structures of Ti_3Al_5 and γ-TiAl, only the samples with nominal 1 % Mo show a large scale microstructural evolution compared to the as-cast state. All specimens show new fissures based on the cooling process and a large amount of pores.

In agreement to previous heat treatments, the LM-Ti-60.4Al-1Mo sample (fig. 4.14a) represents the farthest advanced specimen in terms of microstructural development towards an equilibrium state. The SEM-BSE-images shows a lamellar microstructure of γ-TiAl (brighter zones) and r-$TiAl_2$ (dimmer zones). The lamellae appear rather fine grained in comparison to the achieved microstructure in section 4.1.2.

The VAR-Ti-59.8Al-1Mo (fig. 4.14c) achieved a partially lamellar microstructure in addition to the as cast state observable in its BSE-picture. The current microstructure represents an interstate of the as-cast state and a fully lamellar structure, where some areas already performed the transition, and the rest is still lacking.

The specimens LM-Ti-60.0Al-3.1Mo (fig. 4.14b) and VAR-Ti-60.3Al-3Mo (fig. 4.14d) again reveal similar results in terms of microstructural evolution. Whereas in both of them the respective as-cast state is observable (fine grained for LM and dendritic structures for VAR), both show only small response to the executed heat treatment. Small amounts of granular r-$TiAl_2$ were observed around crack surfaces. The lamellar formations in the grain interior in figure 4.14b might be due to a highly segregated state decreasing the effective Mo content in that area combined with the nigh crack surface offering higher diffusion rates and the different phase equilibrium at 800 °C.

The VAR-Ti-59.8Al-1Mo-3.9Nb-0.03B (fig. 4.14e) sample shows no response to the performed heat treatment what so ever. The microstructure matches the dendritic structures observed in the as-cast state. No precipitations are observable.

Figure 4.15 shows the respective XRD patterns for VAR-Ti-59.8Al-1Mo (which yields the same result as LM-Ti-60.4Al-1Mo), where part of the transformation has already taken place and therefore the microstructure consists of γ-TiAl, r-$TiAl_2$ and h-$TiAl_2$, and for VAR-Ti-59.8Al-1Mo-3.9Nb-0.03B, where the microstructure resembles the as-cast state and the diffractogram yields γ-TiAl and h-$TiAl_2$ as the occurring phases and no r-$TiAl_2$ superlattice peaks are observable. The latter one revealed similar diffractograms to the 3 at.% Mo specimens.

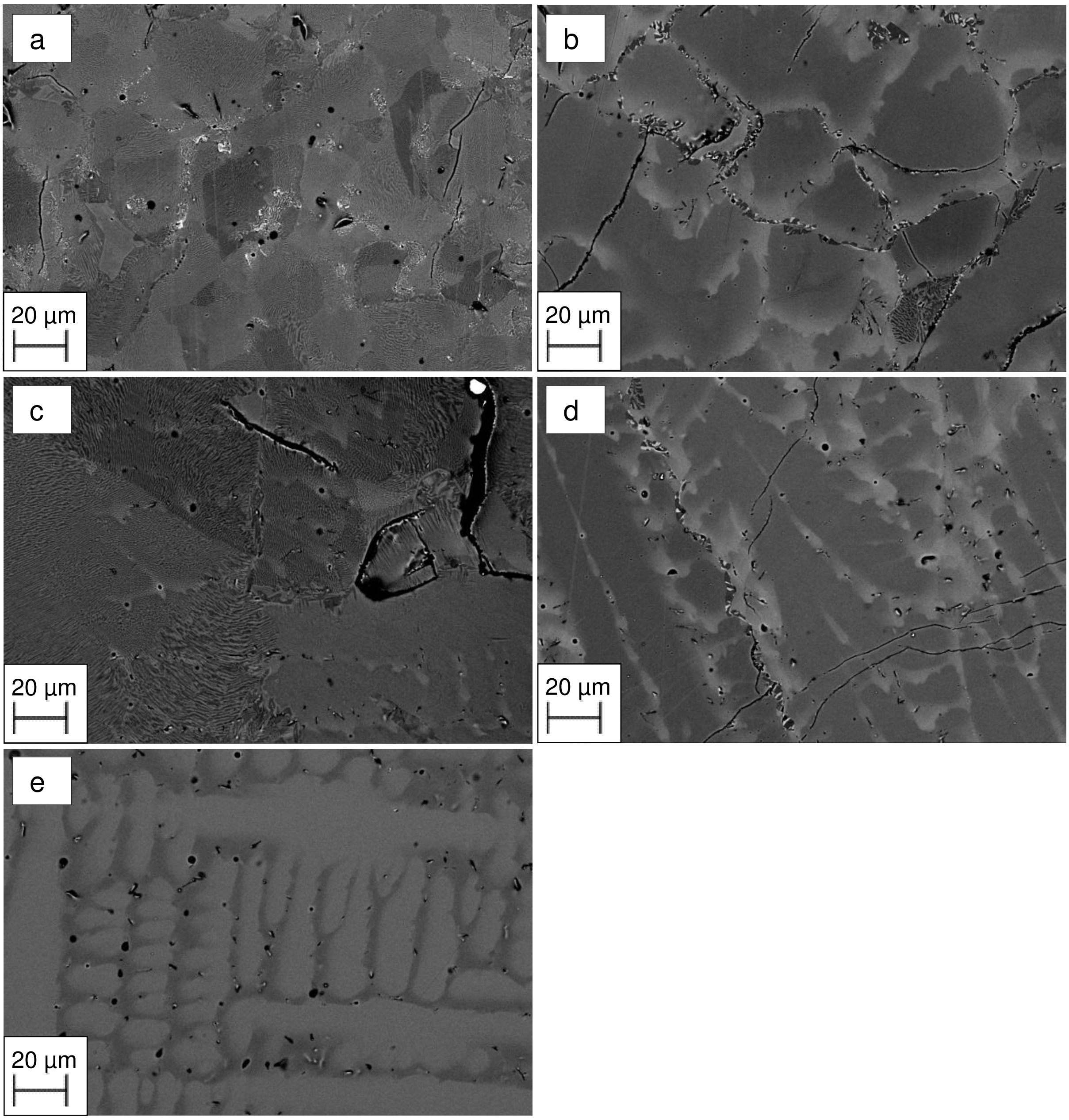

Fig. 4.14: SEM-BSE micrographs of a) LM-Ti-60.4Al-1Mo, b) LM-Ti-60.0Al-3.1Mo, c) VAR-Ti-59.8Al-1Mo, d) VAR-Ti-60.3Al-3Mo and e) VAR-Ti-59.8Al-1Mo-3.9Nb-0.03B after 500 hours at 800 °C followed by water quenching; a) and b) show interstages of the as-cast state and the a fully lamellar structure of γ-TiAl and r-$TiAl_2$; b) and d) show the segregated as-cast state with a few coarse r-$TiAl_2$ precipitations nucleated from cracks; e) did not respond to the heat treatment at all.

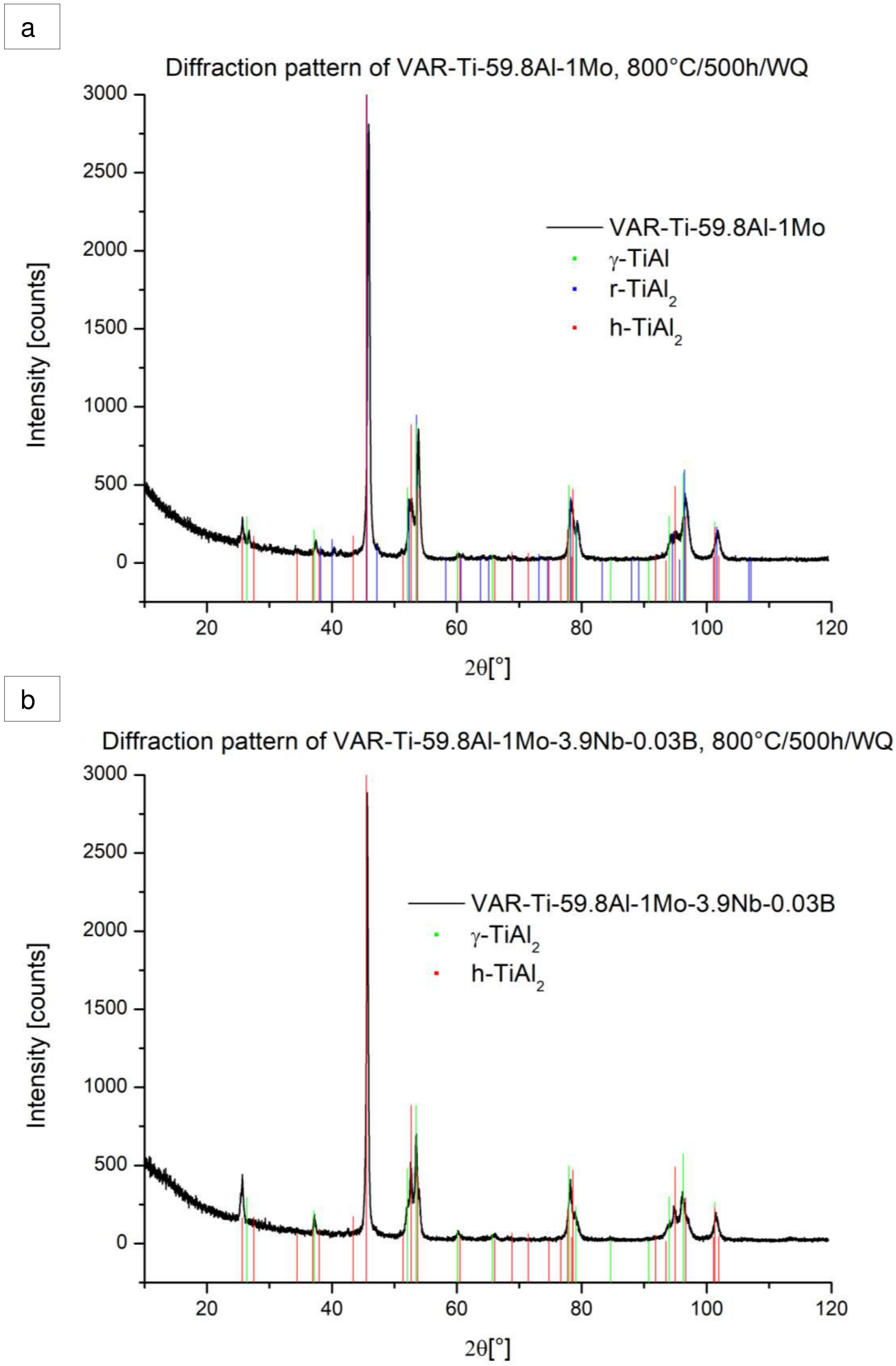

Fig. 4.15: XRD pattern for a) VAR-Ti-59.8Al-1Mo and b) VAR-Ti-59.8Al-1Mo-3.9Nb-0.03B after 800 °C / 500 h / WQ measured with CoKα. The respective diffraction peaks of γ-TiAl (green), r-$TiAl_2$ (blue) and h-$TiAl_2$ (red) are indicated.

To analyze the adjusted chemical compositions in the transformed areas and changes to the as-cast state due to the annealing, further EPMA investigations were performed on all specimens. Contrary to the previous EPMA measurement after 1000 °C / 200 h / WQ, where the LM-Ti-60.4Al-1Mo revealed no solubility range for Mo within r-$TiAl_2$, Mo could be found across all occurring phases. Average Mo shares in r-$TiAl_2$ were 0.56 at.% and 0.8 at.% for both γ-TiAl and spot measurements across lamellar areas. Furthermore, the determined Mo share was comparatively high ranging from 0.48 at.% to 1.28 at.%, whereas the previous results implied a way lower absolute Mo content within the specimen than calculated via wet chemical analysis. It is therefore concluded that the Mo distribution along the bulk material for LM-Ti-60.4Al-1Mo is inhomogeneously distributed. Impurifications with Fe were observable as well, especially within r-TiAl averaging 1.01 at.% and 0.42 at.% in lighter γ-TiAl areas. This behaviour was already witnessed in 4.1.2 and was again in contrast to the Mo behaviour. As observable in Figure 4.14a, clusters containing heavy elements appearing very bright in the BSE micrograph could be observed as well containing up to 1.28 at.% Mo and 3.66 at.% Fe. These clusters also showed partially low total measurement sums of mass percent, from 85 % to 95 %. Therefore, further impurifications might be present that could not be identified and might alter results of LM-Ti-60.4Al-1Mo even further.

On the contrary, VAR-Ti-59.8Al-1Mo showed higher mass percent sums (all above 99 %) and impurifications of Fe averaged 220 ppm. γ-TiAl (61.49 at.% Al and 37.80 at.% Ti) averaged 0.87 at.% Mo, whereas r-$TiAl_2$ (65.01 at.% Al and 34.34 at.% Ti) included 0.62 at.% Mo. Again, contrary to the result observed after the 1000 °C / 200 h / WQ heat treatment, Mo did solute within r-$TiAl_2$.

Once again, LM-Ti-60.0Al-3.1Mo and VAR-Ti-60.3Al-3Mo showed similar results throughout the EPMA. Figure 4.16 shows the BSE pictures for both samples, on which EPMA measurement spots are marked. Both specimens show similar results for r-$TiAl_2$ with 1.5 at.% Mo. Composition ranges vary for strongly depending on the spot within the γ-TiAl ranges for both samples. As previously observed (see section 4.1.1), segregations hold a stronger share of Mo (4.41 at.%), whereas the share for the dimmer areas of γ-TiAl on average is 2.39 at.% Mo. Some very bright, small districts along the transformed areas of r-$TiAl_2$ even contain shares up to 8.5 at.% Mo. Equilibrium is not yet reached and Mo homogenization across the specimen still has to take place. Considering that the heat treatment already took 500 hours, it is questionably if an equilibrium is even reachable practically at 800 °C. Fe contamination amounted to 680 ppm in LM-Ti-60.0Al-3.1Mo and around 150 ppm in

VAR-Ti-60.3Al-3Mo. No preferences in the Fe whereabouts were observable in either sample.

Finally, the VAR-Ti-59.8Al-1Mo-3.9Nb-0.03B, which showed no response to the heat treatment in its corresponding SEM-BSE images, was investigated via EPMA. Contrary to the previous SEM investigation, lamellar areas consisting of γ-TiAl and r-$TiAl_2$ were observable additionally to the as-cast state. Segregations, which appeared darker due to a smaller Nb share, revealed 1.2 at.% Mo, 2.51 at.% Nb, 62.68 at.% Al as well as 33.6 at.% Ti. Measurement spots within the dendrites (60.76 at.% Al, 33.77 at.% Ti) showed a larger Nb (4.47 at.%) and smaller Mo shares (0.56). The same trend was already observed in the previous EPMA measurement on the as-cast state. 10 µm spot measurements revealed a similar result to the interdendritic area: 0.59 at.% Mo, 4.27 at.% Nb complemented by 61.31 at.% Al and 33.81 at.% Ti. Measurements of the r-$TiAl_2$ (darker lamellae) proved that Mo soluted within the precipitated r-$TiAl_2$. 0.66 at.% Mo were observable additionally to 2.59 at.% Nb, 64.43 at.% Al and 32.27 at.% Ti. Furthermore, higher Fe counts were measured within the r-$TiAl_2$ (around 600 ppm). The remaining areas averaged 130 ppm Fe. Figure 4.17 shows the BSE micrograph of VAR-Ti-59.8Al-1Mo-3.9Nb-0.03B after 800 °C / 500 h / WQ consisting of the as-cast state and areas, where the transformation to lamellar γ-TiAl and r-$TiAl_2$ has already taken place. Exemplary EPMA spots are marked.

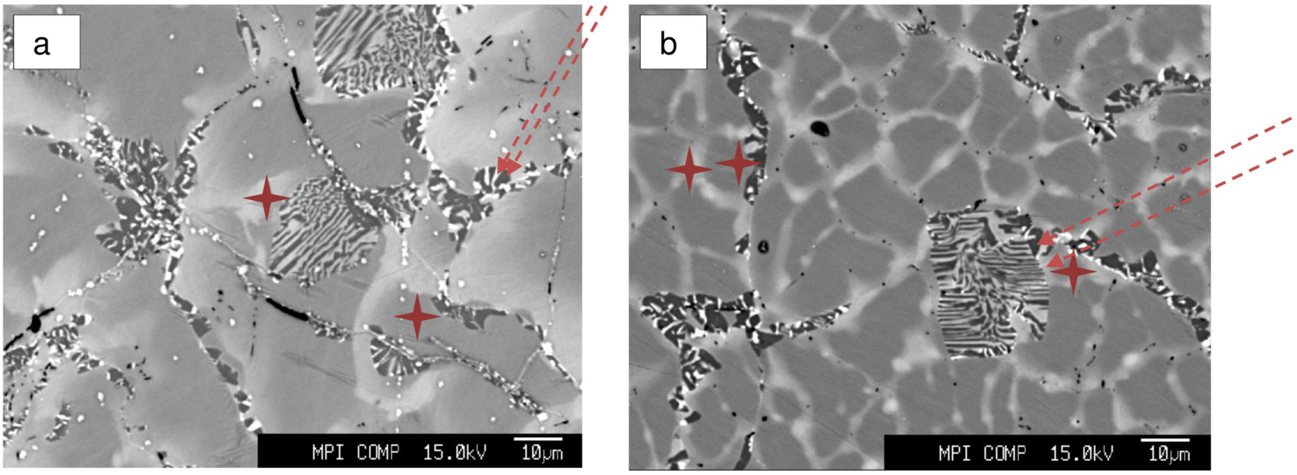

Fig. 4.16: BSE micrographs of a) LM-Ti-60.0Al-3.1Mo and b) VAR-Ti-60.3Al-3Mo showing the as cast state of γ-TiAl (dim areas) with surrounding segregations (light areas) as well as already transformed areas of γ-TiAl and r-$TiAl_2$ (dark). EPMA spots are marked accordingly.

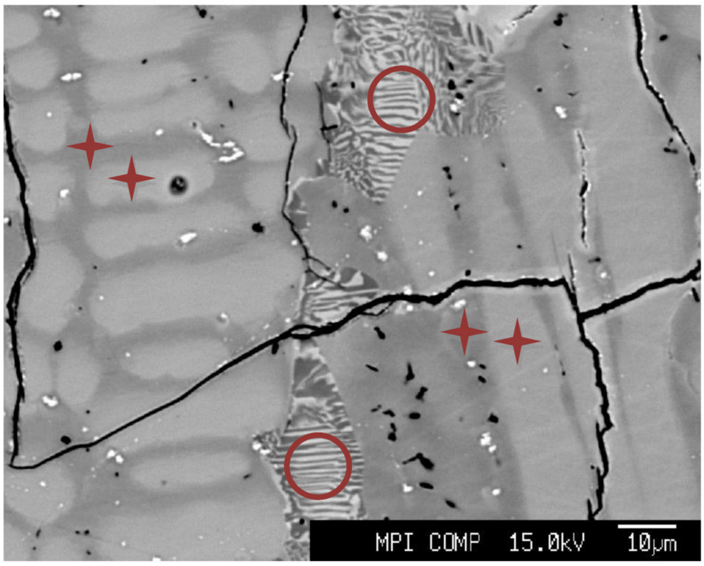

Fig. 4.17: BSE image of VAR-Ti-59.8Al-1Mo-3.9Nb-0.03B after 800 °C / 500 h / WQ showing the as-cast state (dendritic γ-TiAl containing large shares of Nb with segregated Mo) and lamellae of γ-TiAl (bright) and r-$TiAl_2$ (dark). EPMA spots are marked accordingly.

4.1.5 Heat-treated state: 800 °C / 24 h / WQ

In response to the results shown in figure 4.14 an additional heat treatment, annealing the specimens for 24 hours at 800 °C followed by water quenching, was executed to further investigate differences in the LM-Ti-60.4Al-1Mo and the VAR-Ti-59.8Al-1Mo transition properties. The LM sample proofed to be highly contaminated (see section 4.1.1) with Fe (that even enriched in segregation zones contrary to all other samples) and only small traces of Mo were observable through all performed EPMA investigations. Furthermore, the contaminated specimen revealed microstructures that were far closer to an equilibrium state than its VAR counterpart. Although the heat treatment was executed on all present samples, those specimens containing large amounts of ternary and quaternary alloying elements did not respond at all to the annealing and revealed the as-cast state in result of the SEM investigation. This result was expected due to the fact, that these samples also showed rather sluggish responses to the same annealing time for 500 hours (see section 4.1.4). Therefore, only the SEM images for the two mentioned specimens are shown in figure 4.18.

Whereas the LM-Ti-60.4Al-1Mo (fig. 4.18a) shows areas where the transformation to a lamellar microstructure of γ-TiAl+r-$TiAl_2$ has already taken place, the microstructure of the VAR-Ti-59.8Al-1Mo specimen is very similar to the as-cast state with segregated areas appearing brighter in the image (fig. 4.18b). No microstructural development apart from a homogenization seems to have taken place. A large amount of pores are observable probably stemming from preparation.

With that particular result in mind, it is therefore concluded, that the quicker microstructural evolution of the LM-Ti-60.4Al-1Mo sample is due to a smaller effective Mo content in this specific investigated area, which is also in accordance to prior EPMA investigations (see further sections). The reason for this might be a general inhomogeneous Mo distribution along the bulk material during processing, which might also explain a different Mo content observed via microstructural characterization in contrast to the one observed with wet-chemical analysis. Thus, the implication concerning the highly Fe contaminated LM-Ti-60.4Al-1Mo is actually, that due to inhomogeneity the investigated samples across all heat treatments contain a much smaller Mo fraction than expected from wet chemical analysis and Fe acts as the main alloying element apart from Ti and Al. Because the actual Fe content in the specimen is still unknown, the designation LM-Ti-60.4Al-1Mo will be maintained for the rest of the thesis. In direct comparison, the sample with a higher content of Mo appears to be far more kinetically impeded.

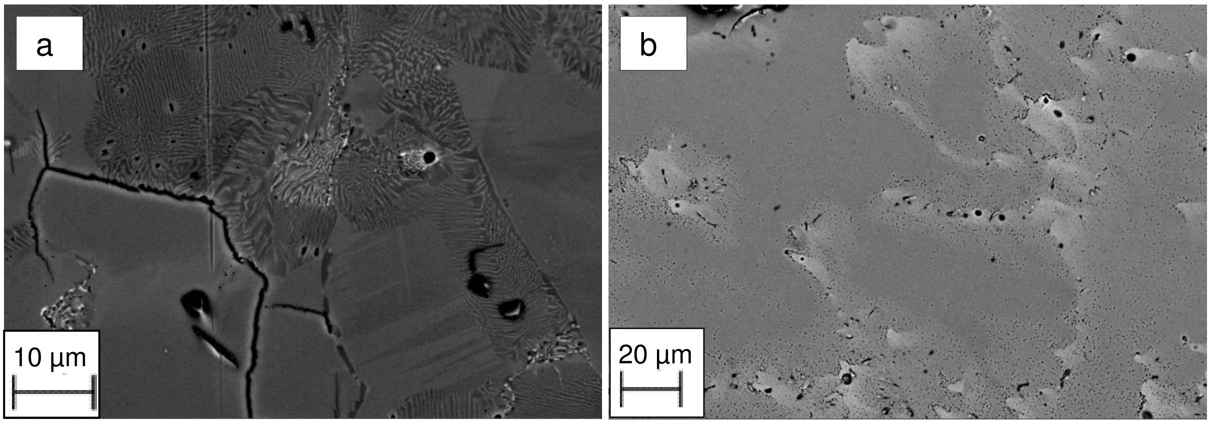

Fig. 4.18: SEM-BSE micrographs of a) LM-Ti-60.4Al-1Mo and b) VAR-Ti-59.8Al-1Mo; a) reveals a partial lamellar microstructure, whereas b) shows a microstructure very close to the as-cast state.

4.1.6 Heat-treated state: 1400 °C / 1 h / FC

Due to the fact that the investigated specimens in their as-cast state revealed a highly segregated microstructure contaminated with large amounts of Fe, O and Ni (see section 4.1.1), the availability of heat-treatment leading to a homogenization of the sample was investigated. All present samples were therefore annealed at 1400 °C for one hour following by furnace cooling for around 15 hours. Figure 4.19 shows the SEM-BSE pictures of the corresponding microstructures.

All of the investigated specimens show a highly improved microstructure in terms of chemical homogenization. Furthermore, all samples reveal a large portion of small scale damages in forms of cracks and fissures, additionally a large amount of pores is observable.

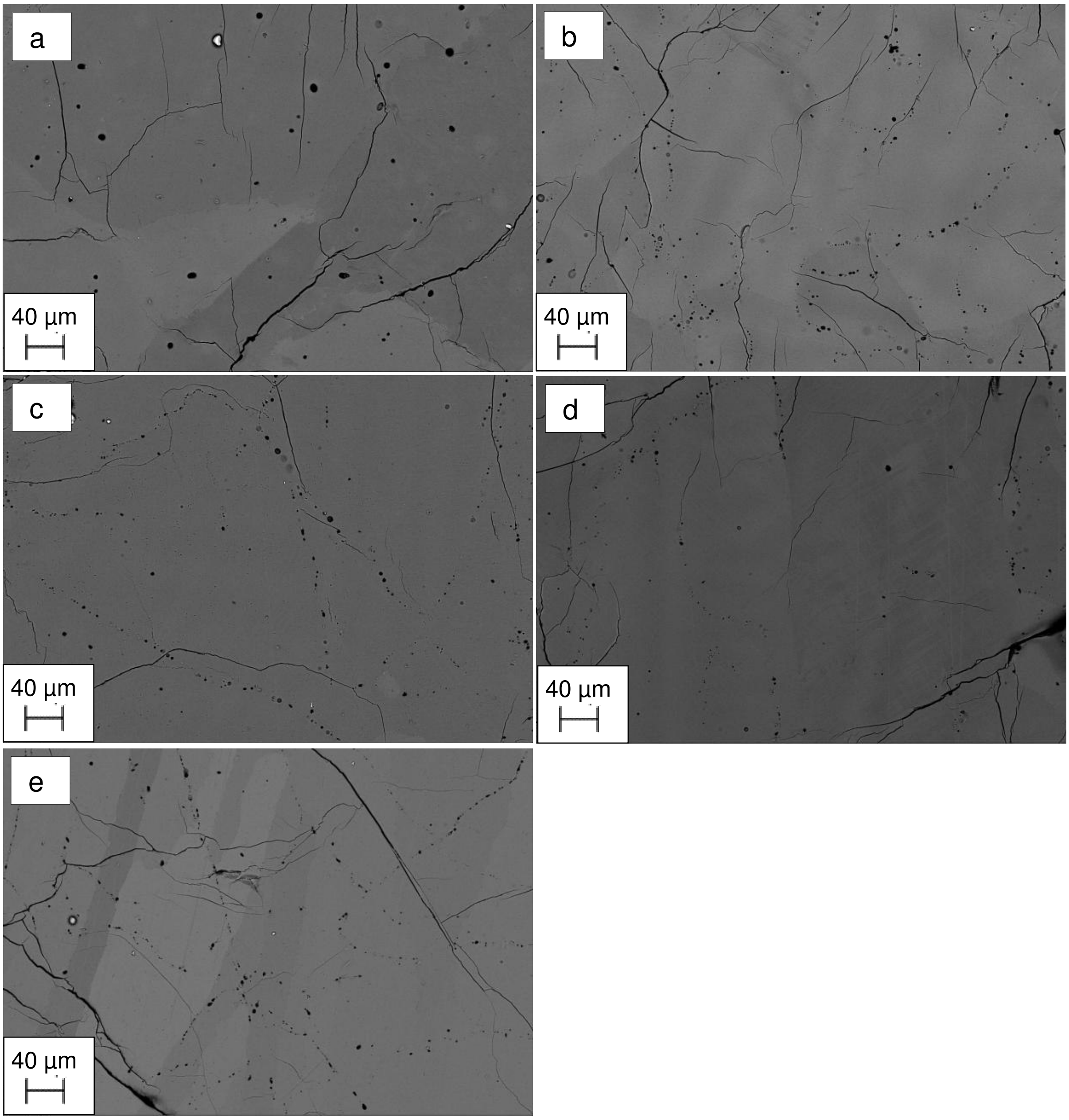

Fig. 4.19: SEM-BSE images of a) LM-Ti-60.4Al-1Mo, b) LM-Ti-60.0Al-3.1Mo, c) VAR-Ti-59.8Al-1Mo, d) VAR-Ti-60.3Al-3Mo and e) VAR-Ti-59.8Al-1Mo-3.9Nb-0.03B after 1 hour at 1400 °C followed by furnace cooling. All of them show an improved microstructure of homogenized γ-TiAl, the strong contrasts in a) and e) might stem from grain orientations.

Furthermore, grain growth has taken place and coarsened the previously fine-grained structure remarkably. Grain orientation contrast is observable in figure 4.19a and 4.19e. The alloys containing higher nominal Mo contents still show remains of segregations in their respective SEM-BSE micrographs (fig. 4.19b and 4.19d).

4.2 Thermal Investigation

4.2.1 Differential thermal analysis

To gain proper insights on the influences of alloying elements on the transition temperatures of Al-rich phases differential thermal analysis (DTA) and differential scanning calorimetry (DSC) were performed. The gateway to a proper investigation was hereby DTA on the as-cast state of all available specimens, evaluating temperature points of physically significance as onset temperatures for first order transitions and peak temperatures (or points of inflection) for second order transitions [20] as described in chapter 3.6.

Table 4.1 includes average onset and peak temperatures as well as liquidus points for all specimens heated three times with 10 K/min, 10 K/min and 5 K/min in Ar-atmosphere. The notation "ac" implies that the effect only took place during the first heatup (as-cast).

Table 4.1: Observed onset, peak and liquidus temperatures for all investigated alloys in °C as observed with DTA

Designation	T_{on} [°C]	T_{peak} [°C]	T_{on} [°C]	T_{peak} [°C]	T_{liq} [°C]
VAR-Ti-59.8Al-1Mo	ac740-823 720-785	ac848	930	1010	1440
VAR-Ti-60.3Al-3Mo	ac720	-	850	935	1435
VAR-Ti-59.8Al-1Mo-3.9Nb-0.03B	840	850	-	935	1455
LM-Ti-60.4Al-1Mo	ac730-805	-	Ac1081	Ac1141 1045	1434
LM-Ti-60.0Al-3.1Mo	Ac710-780	-	-	935	1433

A first evaluation of these significant temperatures is already possible. The first effect taking place at around 700 to 850 °C is highly dependent on the stage within the heating cyclus, which is pronounced especially during first heatups (ac in table 4.1).

This behaviour was already observed for the metastable Ti_3Al_5 phase (see section 2.6). Ti_3Al_5 needs a certain amount of oversaturated γ-TiAl to form, which might has been the case during processing cooldown. During further heatups the effect is hardly observable at all except for the VAR-Ti-59.8Al-1Mo-3.9Nb-0.03B, which shows a highly pronounced peak at slightly higher temperature during every heatup in contrary to all other samples. The sample VAR-Ti-59.8Al-1Mo shows the effect on a very small scale during every heatup, whereas within its levitation melted counterpart LM-Ti-60.4Al-1Mo a very small effect is only observable during the very first heatup. In consideration of the highly impure state of the LM-Ti-60.4Al-1Mo as observed in section 4.1, the accuracy of its DTA is questionable and remarked within this thesis. Both specimens containing nominal 3 at.% Mo reveal similar results with a very small effect during the first cyclus. Except for the peak-like effects of VAR-Ti-59.8Al-1Mo-3.9Nb-0.03B all observable effects are only slightly pronounced and very weak.

The effect occurring at higher temperatures of around 850 to 1050 °C might therefore appertain to the solution of h-$TiAl_2$ and possible r-$TiAl_2$ within the γ-TiAl phase. All observed effects occur during every heatup with consistency except for the contaminated LM-Ti-60.4Al-1Mo, for which the effect takes place at slightly higher temperature during the first heatup in the as-cast state. The evaluated temperatures are higher for the specimens containing lower contents of alloying elements with definable onset temperatures for the effect.

The liquidus temperature itself shows small dependency on alloy composition. Whereas an increase in Mo from 1 at.% to 3 at.% content lowers the liquidus temperature by 5 °C, the VAR-Ti-59.8Al-1Mo-3.9Nb-0.03B revealed an increase in liquidus temperature to 1455 °C. The influence of alloy composition on the liquidus temperature was not further investigated in this thesis. The next chapter described the results of the DSC investigations to properly investigate these observed significant temperatures and their dependency on microstructural state and heating cycles.

4.2.2 Differential scanning calorimetry

As observed in chapter 4.1, the samples processed via levitation melting revealed contaminations with Fe and Ne. Therefore, to retain a certain degree of comparability, DSC investigations were only performed on all three alloys processed via vacuum arc remelting. Because all effects in temperature range from 700 to 1100 °C show very weak changes in the heat flow, an additional reference sample (Ti-57Al) was heated up to 1300 °C. To represent the small peculiarity of the observable effects a single specimen (VAR-Ti-59.8Al-1Mo after 1000 °C / 200 h / WQ) was heated to 1500 °C with 10 K/min. Its characteristic DSC curve is shown in figure 4.20. The broad, first order transition peak belongs to the melting process, the temperature range of significant solid state transformations is marked by the rectangle.

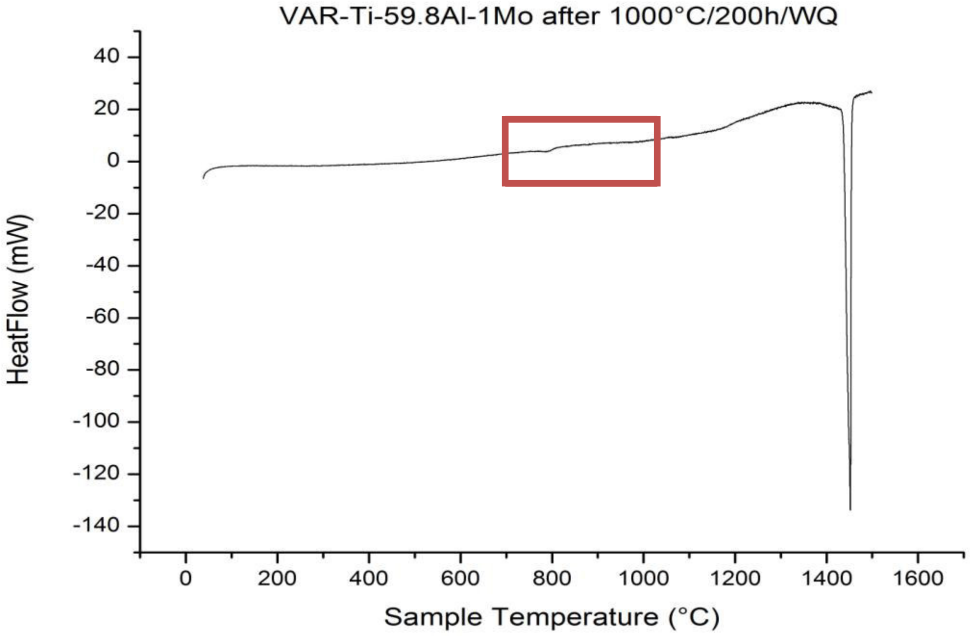

Fig. 4.20: DSC heating-curve of VAR-Ti-59.8Al-1Mo after 1000 °C / 200 h / WQ with a strong melting peak at around 1430 °C and small effects from 800 °C to 1000 °C. The temperature range with significance for this thesis is marked with the red rectangular.

The three specimens in their representative as-cast state were heated to 900 °C (held for 10 hours), 1100 °C (held for 30 minutes) and 1300 °C to bypass the characteristic effects of Al-rich TiAl alloys, such as the occurrence of Ti_3Al_5 from an oversatured γ-TiAl crystal. The first end temperature of 900 °C was therefore chosen to stop the heating process in the two-phase region, the second temperature of 1100 °C was selected to ease into the single-phase region of γ-TiAl and the final temperature of 1300 °C was chosen for a final, complete heatup. Figure 4.21 shows the DSC heating curves for VAR-Ti-59.8Al-1Mo, VAR-Ti-60.3Al-3Mo and VAR-Ti-59.8Al-1Mo-3.9Nb-0.03B in the as-cast state. As observed in the DTA (section 4.2.1), the effect occurring at around 800 °C appears highly pronounced for the first heatup for VAR-Ti-59.8Al-1Mo (green curve in fig. 4.21a) and is hardly observable afterwards. VAR-Ti-60.3Al-3Mo also behaves similar to previous DTA results, where it showed only a very weak effect during the first heatup.

VAR-Ti-59.8Al-1Mo-3.9Nb-0.03B on the other hand shows the pronounced, peak-like effect around 850 °C for the first (green curve in fig. 4.21c) and the third heatup (red curve in fig. 4.21c). During the previous DTA investigation, the effect was pronounced during every heatup, whereas the second curve (blue in fig. 4.21c) shows only a weak effect at lower temperature. During the previous DTA, the specimen was heated all the way up to its melting point during every cyclus, whereas the maximal temperature during the first heatup performed via DSC was 900 °C, as mentioned before. The first cooldown process therefore provided a less oversaturated γ-TiAl crystal for formations of metastable phases. This behaviour goes in line with literature (see section 2.6 for further information) and it is hence concluded that the effect at around 800 °C belongs to the solution and formation of Ti_3Al_5. Because the metastable Ti_3Al_5 rapidly dissolves above a certain phase boundary temperature, the onset temperature (T_{on}) is of physically significance. The effect happening at around 1000 °C is attributed to the solution of h-$TiAl_2$ and possibly r-$TiAl_2$ along a phase boundary. Due to its stretched and weak appearance, proper determination of the significant peak temperature (Tpeak) is difficult and therefore heat-treated samples were investigated.

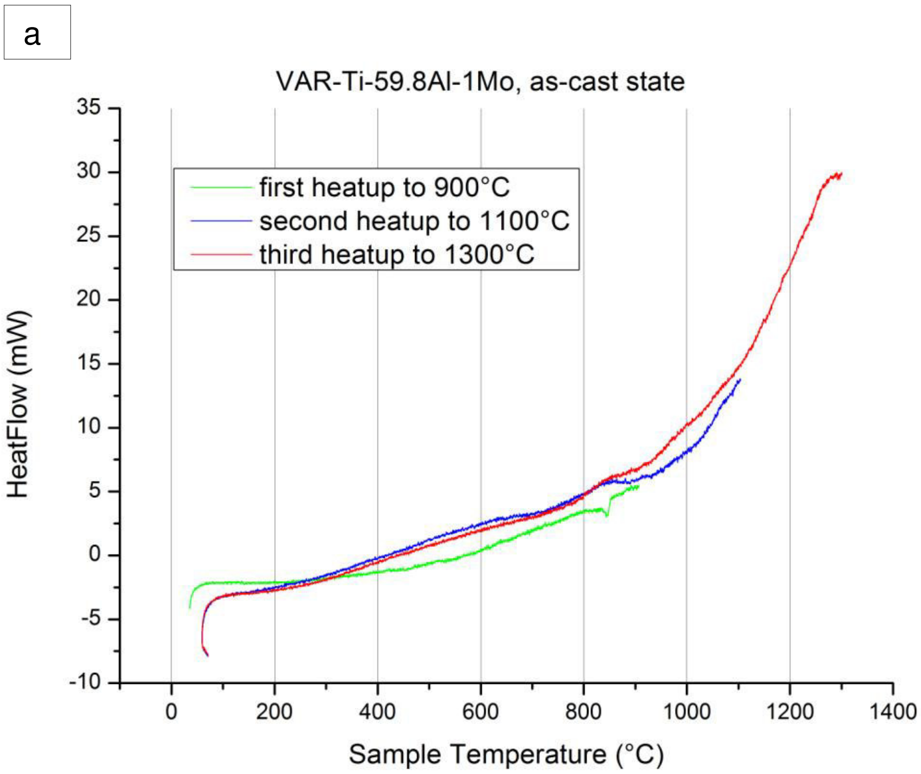

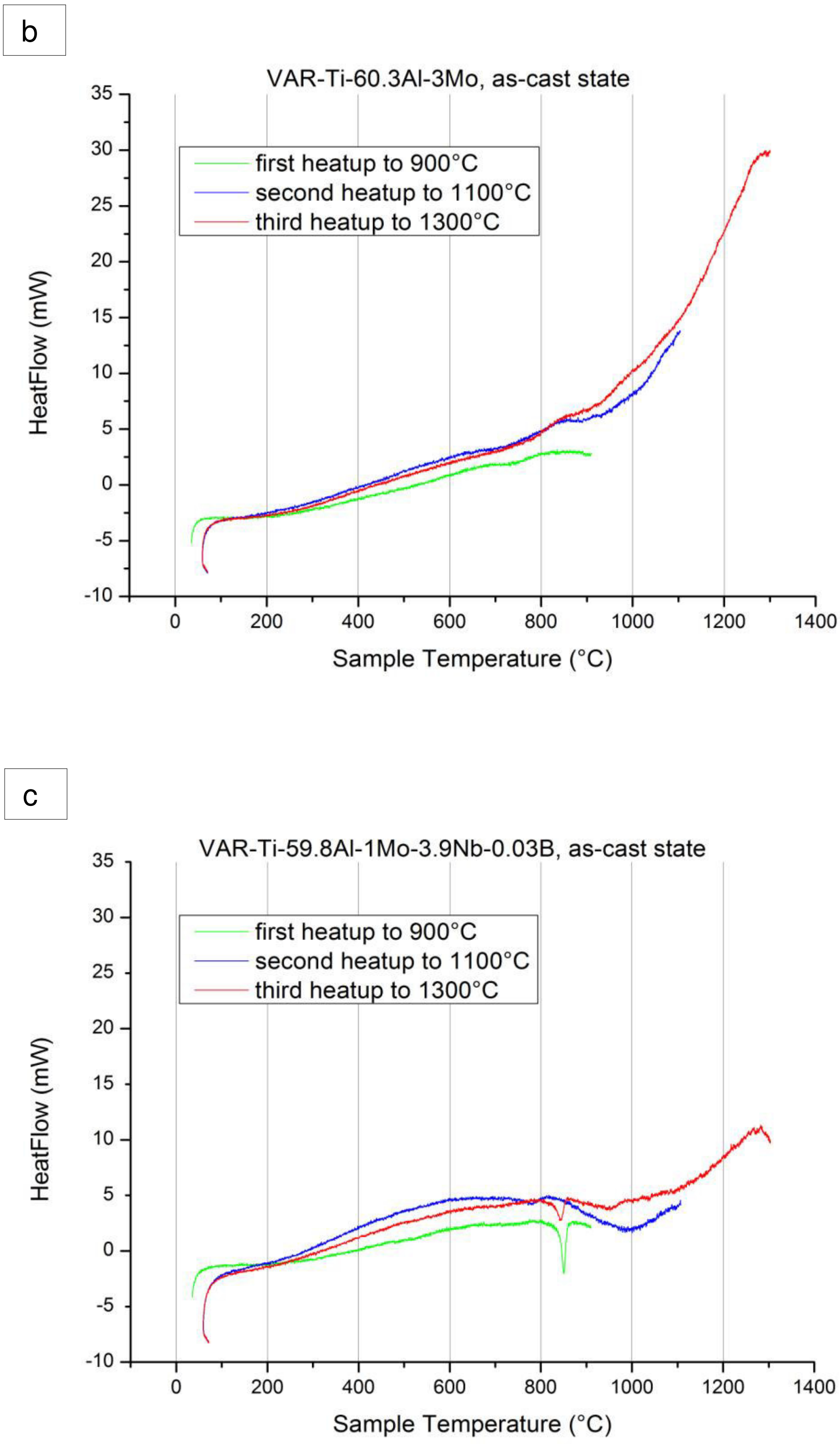

Fig. 4.21: DSC heating-curves for a) VAR-Ti-59.8Al-1Mo, b) VAR-Ti-60.3Al-3Mo and c) VAR-Ti-59.8Al-1Mo-3.9Nb-0.03B in their as-cast state with 10 K/min. The green curve is the first heatup to 900 °C, the blue curve represents the second heatup to 1100 °C and the red curve is the final heatup to 1300 °C.

4.2.2.1 Determination of the γ-TiAl/r-TiAl$_2$ ↔ γ-TiAl transition temperature

Proper establishment of the transition temperature from the one phase γ-TiAl region into a two-phase domain of γ-TiAl and r-TiAl$_2$ yielded rather difficult due to the weak effects of the transition and the additional dissolving of Ti$_3$Al$_5$ at lower temperatures. To gain a satisfying result DSC investigations were performed on heat-treated samples (1000 °C / 200 h / WQ), which provides a microstructure containing a rather large amount of r-TiAl$_2$. To further increase peak intensity the second curve of the heating cycles was chosen for the final transition point determination. Due to an annealing time of 10 hours at 900 °C after the first heating cycle the state of oversaturation of the γ-TiAl crystal was rather small. Therefore, only small shares of Ti$_3$Al$_5$ formed during cooldown due to their closer crystallographic relations with γ-TiAl than r-TiAl$_2$ (see section 2). The result was a specimen with a high amount of dissolvent (r-TiAl$_2$) and a very small share of the additional phase (Ti$_3$Al$_5$). Figure 4.22 shows the DSC heating curves for VAR-Ti-59.8Al-1Mo, VAR-Ti-60.3Al-3Mo and VAR-Ti-59.8Al-1Mo-3.9Nb-0.03B in their respective heat-treated state.

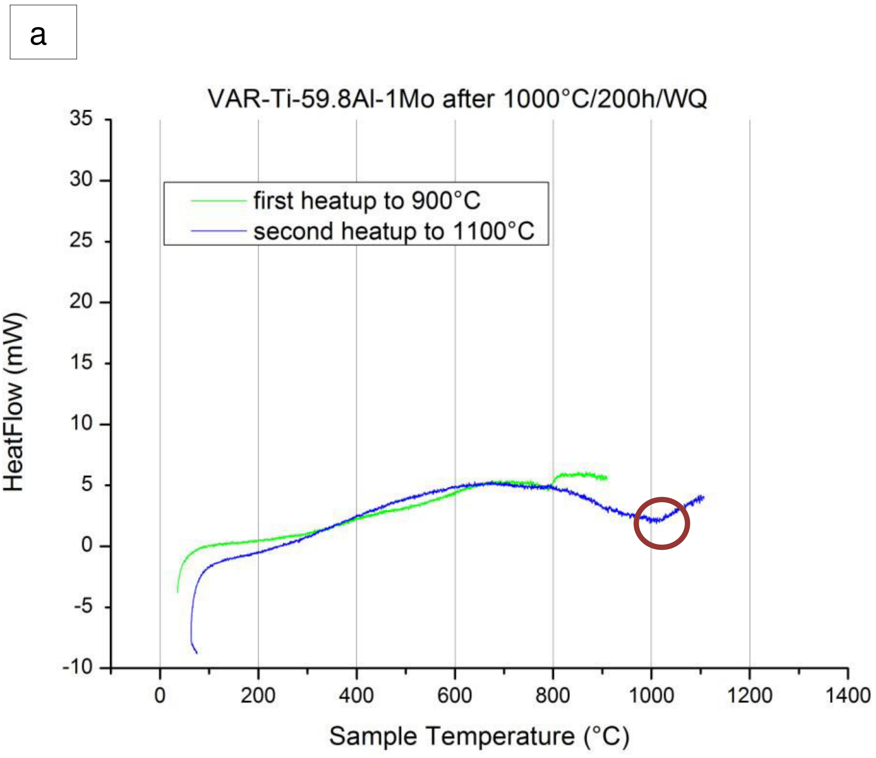

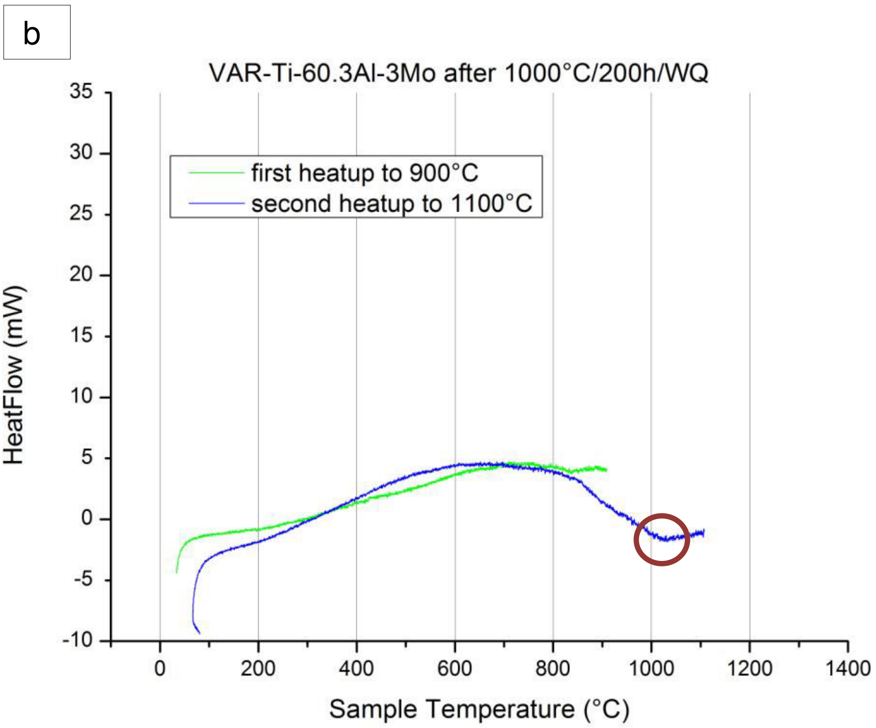

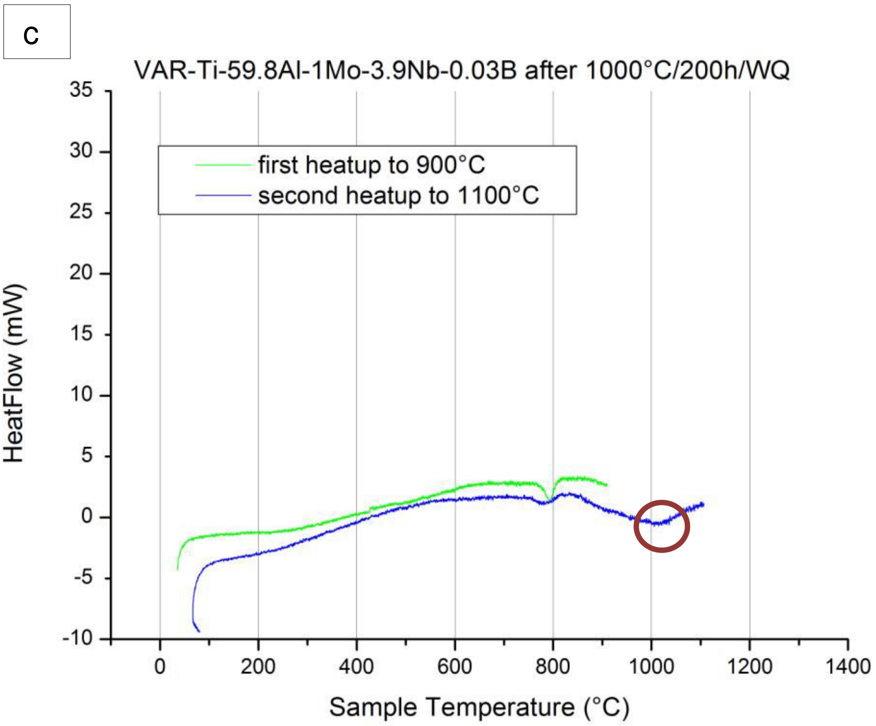

Fig. 4.22: DSC heating-curves for a) VAR-Ti-59.8Al-1Mo, b) VAR-Ti-60.3Al-3Mo and c) VAR-Ti-59.8Al-1Mo-3.9Nb-0.03B after 1000 °C / 200 h / WQ with 10 K/min. The green curve is the first heatup to 900 °C and the blue curve represents the second heatup to 1100 °C. Determined peak temperatures are marked with red circles.

Table 4.2 includes the measured peak temperatures for the γ-TiAl/r-$TiAl_2$ ↔ γ-TiAl transition.

Table 4.2: Peak temperatures for the γ-TiAl/r-$TiAl_2$ ↔ γ-TiAl transition temperature for the three VAR specimens as observed with DSC

Designation	T_{peak} [°C]
VAR-Ti-59.8Al-1Mo	1010.1
VAR-Ti-60.3Al-3Mo	1002.5
VAR-Ti-59.8Al-1Mo-3.9Nb-0.03B	1008.7

All observed results were reproducible for 800 °C / 500 h / WQ heat-treated specimens (because 900 °C annealing temperature is enough to fully dissolve Ti_3Al_5). Due to the fact that the higher temperature heat treatment yielded microstructures closer to equilibrium for all compositions the peak temperatures from the 1000 °C / 200 h / WQ were chosen as representative results for this thesis.

4.2.2.2 Determination of the Ti_3Al_5 decomposition temperature

Due to the specific thermal stability of the metastable Ti_3Al_5 determination of the decomposition temperature, at which Ti_3Al_5 rapidly dissolves, is highly dependent on previous sample history in terms of heating and annealing cycles. Furthermore, decomposition temperature of Ti_3Al_5 is dependent on the present microstructure. Therefore, evaluated temperatures were chosen from these specific conditions where a large share of Ti_3Al_5 is present and an energetically preferable state is reached for this metastable structure. Onset temperatures of the respective peaks were chosen for the decomposition temperature due to its nature of rapid decomposition above a certain temperature (see section 2.6 for further information). Temperature values were determined for the as-cast samples due to the highly oversaturated states of the γ-TiAl crystal and pronounced peaks of Ti_3Al_5 during the first heatup. Figure 4.23 shows the DSC-curves for VAR-Ti-59.8Al-1Mo, VAR-Ti-60.3Al-3Mo and VAR-Ti-59.8Al-1Mo-3.9Nb-0.03B up to 900 °C with 10 K/min. The respective peaks and effects for the decomposition of Ti_3Al_5 take place between 690 and 870 °C. The determined onset temperatures are included in Table 4.3.

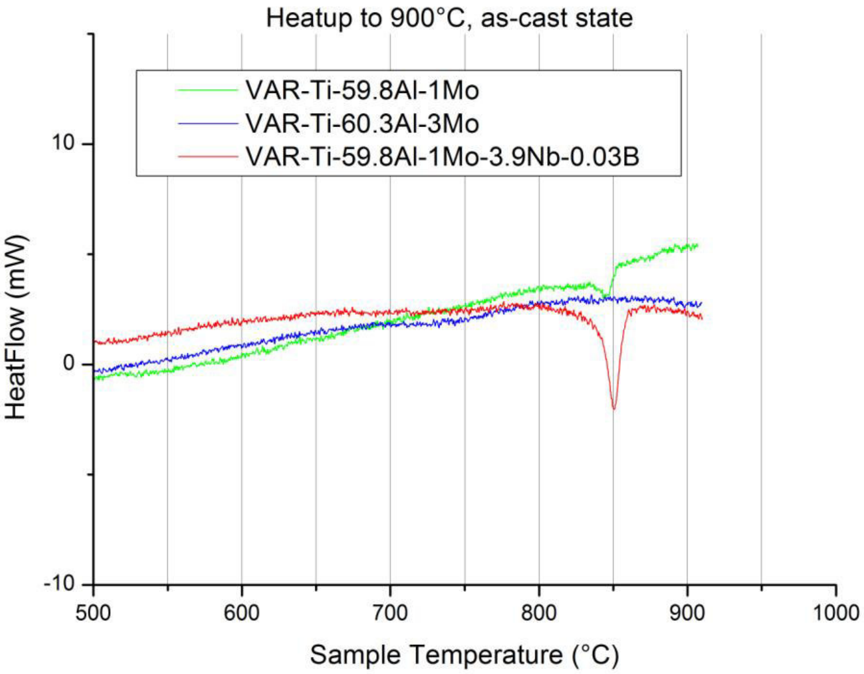

Fig. 4.23: DSC heating-curves for VAR-Ti-59.8Al-1Mo (green curve) VAR-Ti-60.3Al-3Mo (blue curve) and VAR-Ti-59.8Al-1Mo-3.9Nb-0.03B (red curve) in their as-cast state with 10 K/min.

Table 4.3: Onset temperatures for the Ti_3Al_5 decomposition temperatures determined for the three VAR specimens in their as-cast state as observed with DSC

Designation	**T_{onset} [°C]**
VAR-Ti-59.8Al-1Mo	830.8
VAR-Ti-60.3Al-3Mo	738.4
VAR-Ti-59.8Al-1Mo-3.9Nb-0.03B	843.8

In direct comparison the onset temperatures for VAR-Ti-59.8Al-1Mo and VAR-Ti-59.8Al-1Mo-3.9Nb-0.03B show a rather similar value, however, the sample containing Nb revealed more intense effects for the Ti_3Al_5 decomposition, though both specimens contain the same nominal Mo share. VAR-Ti-60.3Al-3Mo shows only very weak effects at very low temperature and it remains questionable to which extend Ti_3Al_5 appears at all. A share of 3 at.% Mo at this stage highly suppresses Ti_3Al_5 formation, whereas a Nb content up to 4 at.% might even ease the Ti_3Al_5 formation. Furthermore, after 800 °C / 500 h / WQ the onset temperature for the Ti_3Al_5 decomposition for VAR-Ti-59.8Al-1Mo-3.9Nb-0.03B increased as already observed in previous investigations (see section 2.6). Therefore, it is concluded that energetically more stable microstructures for Ti_3Al_5 also form for VAR-Ti-59.8Al-1Mo-3.9Nb-0.03B when annealed for a considerately time shortly underneath the Ti_3Al_5 decomposition temperature. Figure 4.24 shows the heating curves to 900 °C for VAR-Ti-59.8Al-1Mo-3.9Nb-0.03B in their as-cast state and after the 800 °C / 500 h / WQ heat treatment, were a very slight increase in the Ti_3Al_5 decomposition temperature of around 10 °C is observable. This behaviour could not be reproduced with the other 2 sample compositions and might therefore be directly connected to the presence of 3.9 at.% Nb in the alloy composition which already showed to increase and sharpen peak intensity for Ti_3Al_5 decomposition.

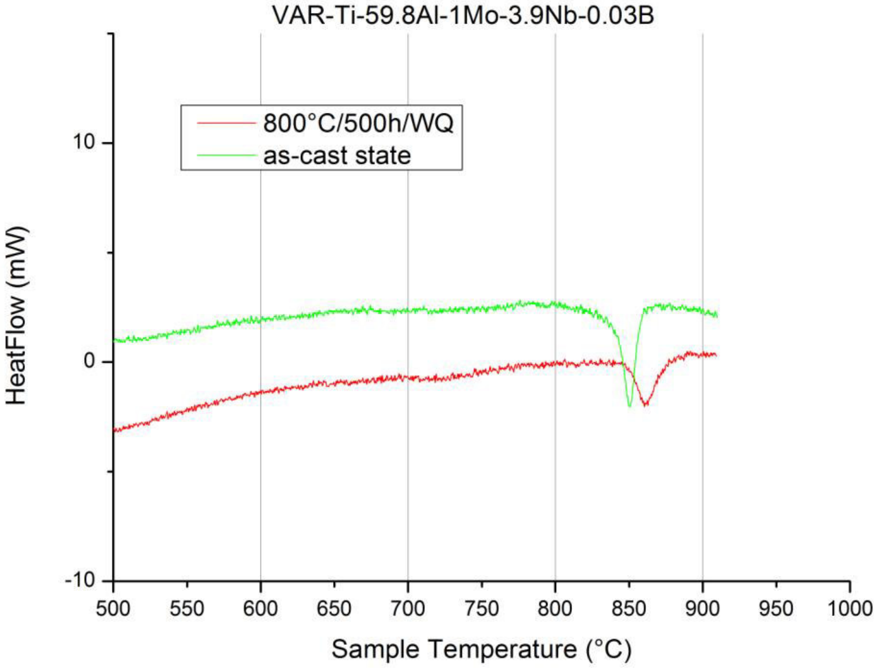

Fig. 4.24: DSC heating-curves for VAR-Ti-59.8Al-1Mo-3.9Nb-0.03B up to 900 °C with 10 K/min in their as-cast state (green curve) and after 800 °C / 500 h / WQ. A slight increase in Ti_3Al_5 decomposition temperature is visible.

4.2.3 The quasi binary Ti-60Al - Mo phase diagram

Due to the results from previous chapters the quasi binary phase diagram of Ti-60Al and Mo is concludable. All solidus and liquidus temperatures were determined via DTA (see section 4.1). Solid state reactions such as the Ti_3Al_5 decomposition and γ-TiAl/r-$TiAl_2$ ↔ γ-TiAl phase border were taken from the DSC measurements in section 4.2. Binary transition temperatures were obtained from literature presented in section 2.

The Ti_3Al_5 decomposition temperature is dotted between 1 at.% and 3 at.% Mo due to the fact that proper determination of the onset temperature proved to be difficult with a remaining degree of uncertainty due to the extremely weak effect.

Additionally, because no specimen revealed a completely transformed microstructure to an equilibrium state during SEM and EPMA investigations and heat treatment studies in section 4.1, the present quasi binary phase diagram represents a practical and technical approach to this topic and it is hereby highly advised to handle it with the proper care, especially because the nominal 60 at.% Al were only approximated with the real alloys and segregations were present in the high alloyed specimens throughout the whole investigation.

Figure 4.25 shows the final quasi binary phase diagram of the Ti-60Al - Mo system with its respective phase regions and transition temperatures. Furthermore, the metastable Ti_3Al_5 has its decomposition temperature line included.

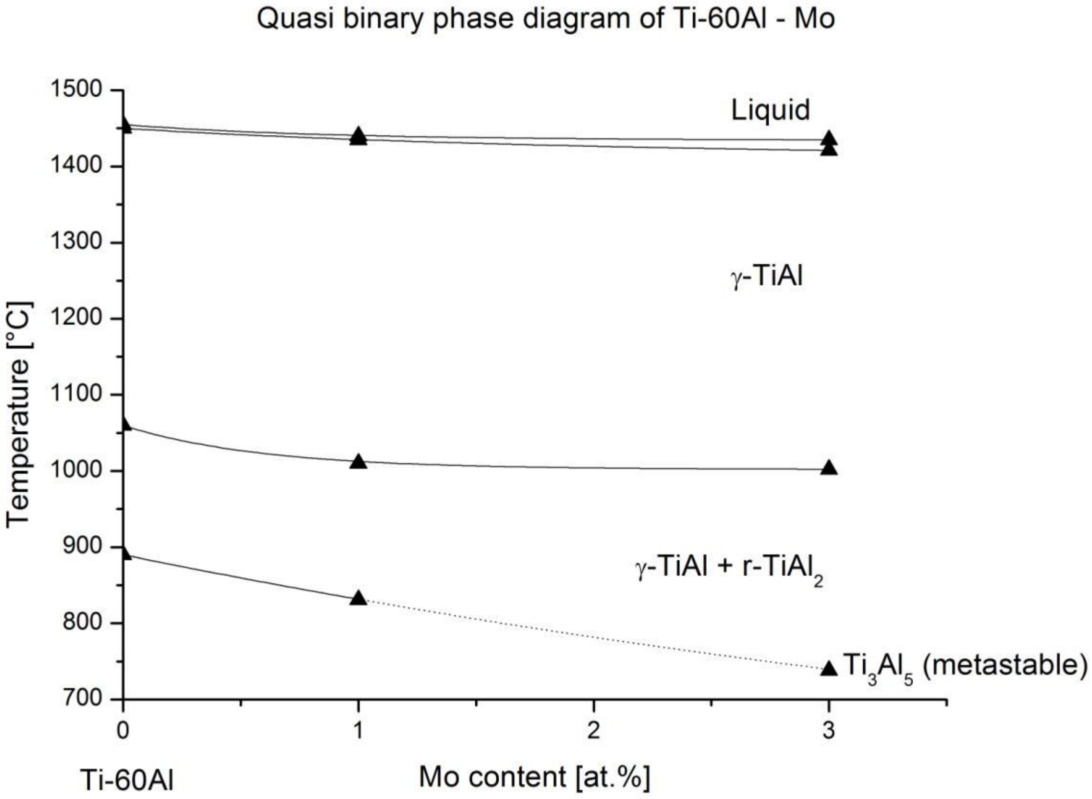

Fig. 4.25: Quasi binary phase diagram of Ti-60Al - Mo as observed throughout this thesis, measured temperatures are marked with triangular symbols. The phase regions liquid, γ-TiAl and γ-TiAl+r-$TiAl_2$ are marked accordingly. Furthermore, the Ti_3Al_5 (metastable) decomposition line is drawn, which is dotted above 1 at.% Mo due to the formation of the Ti_3Al_5-phase being suppressed.

In addition to liquidus and solidus temperature, which decrease for an Al-rich TiAl alloy with increasing Mo content, the size of the single phase γ-TiAl region increases and the stability range of r-$TiAl_2$, which solves only very small shares of Mo within the alloy as shown in section 4.1, gets constrained slightly. A higher Mo content impedes the formation of Ti_3Al_5 and decreases the decomposition temperature. Formation of Ti_3Al_5 was almost complete suppressed in the alloy with 3 at.% Mo. Increasing the Mo content therefore is a valid method to decrease and deny appearance of the embrittling Ti_3Al_5, whereas an increase in Mo content at this stage does shift the phase equilibrium of γ-TiAl and r-$TiAl_2$ towards a larger share of γ-TiAl, but does not completely deny formation of r-$TiAl_2$, which would be necessary in Al-rich TiAl alloys for lamellar microstructures.
The trends for the VAR-Ti-59.8Al-1Mo-3.9Nb-0.03B are quite similar, the width of the γ-TiAl single phase region increased, whereas solidus temperature decreased. Surprisingly, in comparison to the alloy counterparts without Nb, the liquidus temperature stayed the same and the decomposition temperature for Ti_3Al_5 was higher than for the other samples without Nb, as well as larger enthalpies for the decomposition were observed. Therefore, it is concluded that Nb as alloying element in this range does not impede the formation of Ti_3Al_5 but rather supports them.

The results will be concluded in the next chapter and also be discussed comprehensively.

5 Discussion

TiAl alloys based on γ-TiAl are lightweight materials for high temperature applications due to a proper creep resistance based on lamellar structures of γ-TiAl and Ti_3Al providing sufficient strength at elevated temperature and necessary ductility at ambient temperature. To further improve, e.g. oxidation resistance, an exceeding Al content of 54 at.% provides a protective Al_2O_3 layer up to 1200 °C. In binary Al-rich TiAl alloys lamellar structures of γ-TiAl and r-$TiAl_2$ were already produced, but further investigation is often handicapped by formation of metastable structures such as Ti_3Al_5 and h-$TiAl_2$ which are very persistent. Information on influences of ternary alloying elements on these metastable formations as well as processing influences and beyond is scarce and therefore main topic of investigation in this thesis.

Investigated alloys contained a nominal Al content of 62 at.%, whereas the samples after processing had Al shares of around 60 at.% due to Al evaporation. No large deviations of the contents of additional alloying elements were observed except for B, where the final result only accounted as 0.03 at.% compared to the desired 0.1 at.%. Processing was done via levitation melting and vacuum arc remelting. The following revises the qualitative and quantitative results obtained in chapter 4.

All specimens contain a large amount of processing related flaws and impairments in their as-cast state, especially the VAR samples were highly damaged on a macroscopic scale. Preparation was rather difficult due to brittle material behaviour. Furthermore, SEM investigations revealed a highly damaged microstructure for all specimens consisting of γ-TiAl and h-$TiAl_2$ as observed via XRD. The radial crack networks stem from high temperature differences during the cooling process. VAR processed samples showed a radial dendritic microstructure, whereas the LM specimens revealed a rather fine-grained microstructure. It is concluded that the LM process provided a quicker cooldown rate and therefore a smaller grain size. Contaminations with Fe and Ni, which were especially present in LM-Ti-60.4Al-1Mo during first EPMA investigations, clustered locally and did not solve within the γ-TiAl matrix.

Mo was in all respective as-cast states contained within segregated areas as well as segregation lines along margins of the γ-TiAl grains. Contrary to Mo, Nb within the VAR-Ti-59.8Al-1Mo-3.9Nb-0.03B sample did not segregate, which lead to reverse contrasts of the SEM-BSE micrographs. Furthermore, borides were observed during

EPMA investigations of the as-cast state of VAR-Ti-59.8Al-1Mo-3.9Nb-0.03B, but not thereafter in heat-treated specimens and no significant grain fining effect was observable for the as-cast condition.

Both processing routes therefore resulted in macroscopic as well as microscopic damaged structures with processing related crack networks as well as highly segregated microstructures. Cracks and manufacturing related flaws are a no-go criterion for future exemplary light-weight materials and therefore processing needs further refinement to improve cooldown conditions such as radial temperature differences. In addition, impurities related to processing and low-grade source materials impede investigations especially with occurrence of these persistent metastable phases and should therefore be prevented as much as possible in further alloy and process development.

As shown in section 4.1.6, holding the specimens at 1400 °C for one hour followed by furnace cooling homogenized all investigated samples to a large extend accompanied by grain growth. None of the other heat treatments of as-cast-samples for various times even up to 500 hours at 800 °C and 1000 °C achieved a microstructure in an equilibrium state. The inclusion of the refractory metals Mo and Nb therefore hampered the microstructural evolution of Al-rich TiAl alloys even more so. Presented heat-treatments were previously conducted in existing literature (see section 2) and resulted in equilibrium-state microstructures, which could not be achieved for Al-rich TiAl alloys supplemented with Mo and Nb.

After heat-treating all specimens for 200 hours at 1000 °C (see section 4.1.2) followed by water quenching similar results to the binary Ti-Al system were achieved. The samples containing nominally 1 at.% Mo revealed lamellar microstructures of γ-TiAl and r-$TiAl_2$ (and h-$TiAl_2$ to some extent, because none of the samples were in an equilibrium state, as shown with XRD in section 4.1.2), which proves at this point that the addition of 1 Mo does not suppress the formation of the metastable h-$TiAl_2$, which is necessary to obtain these lamellar structures. The metastable h-$TiAl_2$ needs to be present in order of the discontinuous phase transformation to take place, which finally leads to lamellar formations of γ-TiAl and r-$TiAl_2$ as shown in [5] (see section 2.5 for further information). No Mo was observed in the Al-rich phase r-$TiAl_2$. It is therefore concluded that the solubility of Mo within r-$TiAl_2$ is very low at a Mo content of 1 at.%. Contrary to the behaviour of Mo, higher Fe contents were found within the r-$TiAl_2$ than in γ-TiAl of the LM-Ti-60.4Al-1Mo specimen, which was contaminated with Fe and Ni. Fe therefore seems to fit rather well within the r-$TiAl_2$ crystal structure as opposed to Mo. Due to the small shares of Fe within the other specimens, these behaviour was not reproducible, where Fe was prone to cluster locally. All microstructures were close to an equilibrium state, though no sample reached it yet. Both specimens with 1 at.% nominal Mo content revealed lower overall Mo contents during EPMA investigations. Especially, only the LM-Ti-60.4Al-1Mo showed Mo contents up to 0.43 at.% Mo in some spots, and not Mo in every γ-TiAl spot during EPMA. The wet chemical analysis concluded larger shares of Mo in the range of 1 at.%, therefore it was concluded that the Mo distribution was not homogenous along the bulk material.

The two samples with 3 at.% nominal Mo content on the other hand revealed microstructures far away from an equilibrium state. The as-cast state was still highly pronounced and visible, with segregations along the grain margins containing large shares of Mo and appearing very bright in SEM-BSE images. The grain interior revealed γ-TiAl with plates of r-$TiAl_2$, which highly resembled structures already observed during studies of the binary system. No r-$TiAl_2$ precipitations were observable along the grain boundaries, were the larger shares of Mo are present from the original as-cast state. Contrary to the lower Mo content samples, the r-$TiAl_2$ plates shared Mo contents up to 1.1 at.% Mo. Still, areas with higher Mo content along the grain margins showed no precipitations of r-$TiAl_2$ at all. Therefore, it is concluded that locally low Mo contents favour precipitation of h-$TiAl_2$ and r-$TiAl_2$ and appropriate Mo diffusion has to take place to generate circumstances necessary for precipitations with h-$TiAl_2$ and r-$TiAl_2$. Alloying Al-rich TiAl alloys with Mo slows the phase transformation to an equilibrium state and impedes the precipitation of Al-rich phases as r-$TiAl_2$. Furthermore, it is very important that the as-cast state of the samples were not in an equilibrium state previously to the heat treatment. Therefore, specimens with segregated microstructures were investigated, which have an influence on investigation outcome. Effectively no precipitations took place in segregated areas with high Mo contents. The question remains how the microstructural evolution would take place if the specimens were previously in a homogenous state. Due to accumulation of Mo within these segregated areas along the boundaries the effective Mo content within the grains is lower as theoretically estimated. Though the plate like structures are similar to Al-rich TiAl alloys with higher Ti content and therefore a smaller share of r-$TiAl_2$, it is questionable if these shares of r-$TiAl_2$ visible in grain interiors would even form to this extend for a homogenous sample. The actual equilibrium state for the 3 at.% Mo content specimens might be postponed more towards γ-TiAl. Figuratively this means, that with an evenly dispensing Mo content along the sample, r-$TiAl_2$ would start to partially dissolve again as a result of previously locally lower Mo contents that shifted the metastable state towards a higher share of r-$TiAl_2$. Further studies on Mo alloyed Al-rich TiAl alloys should investigate microstructural evolution on homogenous specimens for comparison, because the actual equilibrium state might provide smaller shares of r-$TiAl_2$. Heat treatments for homogenization as shown in section 4.1.6 might be appropriate previously. Figure 5.1 shows the SEM-BSE micrographs for VAR-Ti-59.8Al-1Mo and VAR-Ti-60.3Al-3Mo again as in section 4.1.2. The Al-rich r-$TiAl_2$ appears dark, whereas the γ-TiAl appears light.

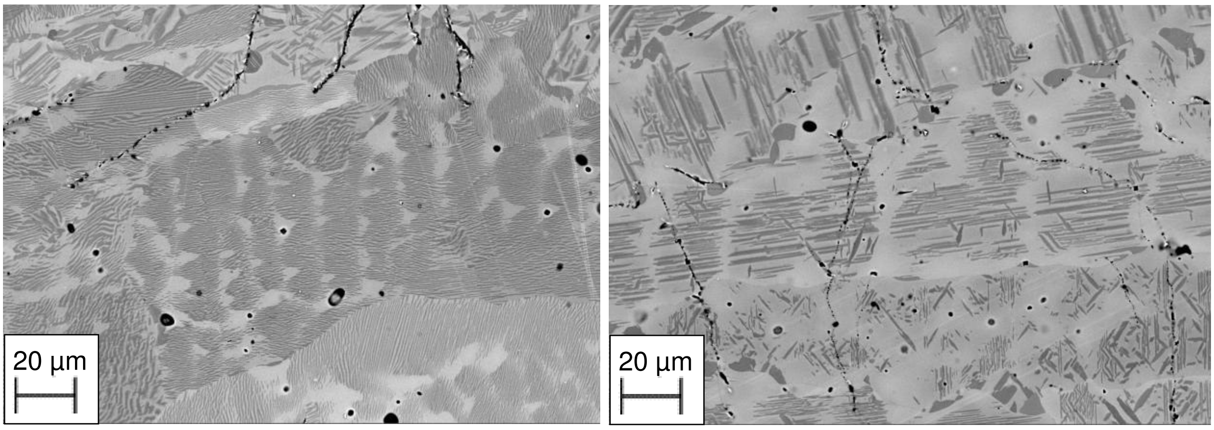

Fig. 5.1: SEM-BSE-micrographs for a) VAR-Ti-59.8Al-1Mo and b) VAR-Ti-60.3Al-3Mo containing γ-TiAl (bright areas) and r-$TiAl_2$ (dim areas) after annealing at 1000 °C for 200 h followed by water quenching. The samples containing nominally 1% Mo a) revealed lamellar microstructure, whereas higher alloyed samples in b) show plate-like microstructures with smaller ratios of r-$TiAl_2$.

The sample VAR-Ti-59.8Al-1Mo-3.9Nb-0.03B also showed a microstructure consisting of γ-TiAl with plates of r-$TiAl_2$. As previously investigated, additional alloying elements rather preferred γ-TiAl as their whereabouts. The plates itself appeared finer grained in comparison to the 3 at.% Mo specimens, which could be attributed to the addition of B as alloying element, which might have a refining effect on the precipitation.

For comparison, the 1000 °C heat treatment was additionally conducted for a shorter duration, to get insights on transformation kinetics. Whereas the 1 at.% Mo specimen showed already developed microstructures similar to the 1000 °C / 200 h / WQ results, the 3 at.% Mo sample showed a highly delayed development. Only a few r-$TiAl_2$ plates were observable within the γ-TiAl grains.

The VAR-Ti-59.8Al-1Mo-3.9Nb-0.03B specimen consisted of segregated γ-TiAl with a few plates of r-$TiAl_2$. Remarkably, the r-$TiAl_2$ plates predominantly precipitate from the grain exterior, the segregations, where a smaller share of refractory elements was present in the as-cast state because Nb shows no tendency to segregate. The behaviour therefore was again reversed to previous results obtained on high Mo alloyed specimens.

For further comparison to the binary Ti-Al system the 800 °C / 500 h / WQ heat treatment was performed. As explained in section 2.6, Ti-60Al revealed a network-like structure of γ-TiAl and Ti_3Al_5 after this heat treatment. No such results were observable for further alloyed Al-rich TiAl alloys. Instead all results were rather similar to the 1000 °C / 200 h / WQ heat treatment, but in an underdeveloped way. Whereas the highly contaminated LM-Ti-60.4Al-1Mo sample (with lower effective Mo content in this specific sample) revealed a rather developed microstructure of γ-TiAl and r-$TiAl_2$ lamellae, though very fine grained, VAR-Ti-59.8Al-1Mo only partially transformed and still showed large domains of the as-cast state.

The other three specimens containing higher degrees of alloying elements only slightly responded to the heat treatment. Though no r-$TiAl_2$ plates were observable, however, in certain areas along cracks and flaws where diffusion rates must have been suitable high, lamellar structures of γ-TiAl and r-$TiAl_2$ were detected. The reason for lamellar structures within the higher alloyed specimens is the different phase equilibrium at 800 °C compared to 1000 °C based on the binary system, which is frozen during cooldown by water quenching. Annealing temperature therefore plays an important role for the adjusting microstructures, but still, these structures mostly resemble the as-cast state even after 500 hours at 800 °C. It is therefore concluded that an actual equilibrium state in Mo and Nb alloyed Al-rich TiAl alloys is not achievable within an appropriate annealing time at 800 °C.

When annealed at 800 °C for 24 hours as shown in section 4.1.5 the three higher alloyed alloys (VAR-Ti-60.3Al-3Mo, LM-Ti-60.0Al-3.1Mo, VAR-Ti-59.8Al-1Mo-3.9Nb-0.03B) did not react to the heat treatment, due to 24 hours being way too short for these composition ranges to actually respond to annealing at 800 °C. Whereas the VAR-Ti-59.8Al-1Mo did only slightly respond, LM-Ti-60.4Al-1Mo, which is Fe contaminated and shows varying, mostly lower contents of Mo compared to samples investigated via wet-chemical analysis, revealed already transformed grains of γ-TiAl and r-$TiAl_2$ lamellae, which proves an impediment of microstructural evolution on grounds of an higher Mo content.

Thermal investigations throughout this thesis were based on the DTA of the as-cast specimens. Whereas the liquidus temperature decreased with increasing Mo content, the specimen VAR-Ti-59.8Al-1Mo-3.9Nb-0.03B surprisingly revealed a higher liquidus temperature. The same effect was observed during investigation of the lower temperature effect which was related to the solution of Ti_3Al_5. Whereas the samples containing 1 at.% and 3 at.% Mo revealed decreasing effect size with increasing Mo concentration, the Ti_3Al_5 peak was highly pronounced and sharp for VAR-Ti-59.8Al-1Mo-3.9Nb-0.03B. For 3 at.% Mo the Ti_3Al_5 effect at around 730 °C was so sluggish that proper determination proved difficult. Nb on the other hand seems to highly support the metastable Ti_3Al_5 structure and stabilize the system up to the melting temperature to some extent. Only vague assumptions can be given for this behaviour and so further work on the topic could focus on these specific, structural related influences of Mo and Nb on the Al-rich TiAl system. Anyway, increasing contents of Mo suppressed the formation of Ti_3Al_5, which is highly wanted in an engineering perspective due to its embrittling behaviour. It is noted again, that no specimen was investigated in an absolute equilibrium state. All quantitative values concluded are therefore "technical" figures, approached from a realistic aspect due to the duration of the performed heat treatments of up to 500 hours.

Due to the annealing state dependency of the lower temperature effect ranging from 730 to 850 °C throughout this investigation it was concluded that this occurrence must belong to the metastable Ti_3Al_5, for which such behaviour could have already been shown in the respective literature in section 2. For the VAR-Ti-59.8Al-1Mo-3.9Nb-0.03B sample it was also possible to show the dependency of the dissolution temperature of Ti_3Al_5 on an annealing heat treatment below the said temperature. This was already shown for binary Ti-Al samples and could therefore be reproduced. The sample VAR-Ti-59.8Al-1Mo did not show such a behaviour though the effective Mo contents are similar. It is therefore concluded that the addition of Nb up to 3.9 at.% to Al-rich TiAl alloys supports formation of Ti_3Al_5.

The temperature range for the γ-TiAl/r-$TiAl_2$ $\leftrightarrow$ γ-TiAl transition was very narrow, ranging from 1002 to 1010 °C. Though addition of refractory alloying elements decreased the transition temperature by around 50 °C compared to the binary system, the Mo increase within the investigated specimens only had small influences as can be seen in figure 5.2, where the assembled quasi binary Ti-60Al - Mo phase diagram is shown. By annealing the samples at 900 °C the state of oversaturation of the γ-TiAl crystal was sufficient to proper determine the transition temperature. This further indicates that the previous effect belongs to the decomposition of the metastable Ti_3Al_5, which forms only from oversaturated γ-TiAl crystals due to a close crystallographic relation.

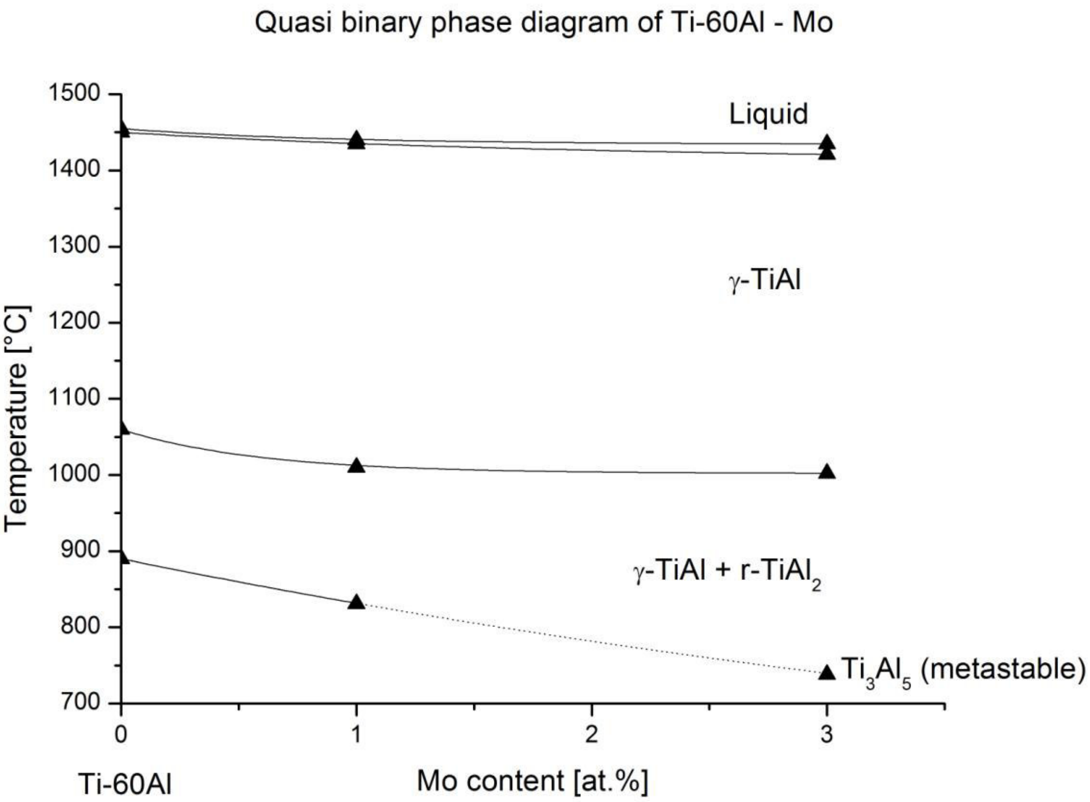

Fig. 5.2: Quasi binary phase diagram of Ti-60Al - Mo as conducted throughout this thesis, measured spots are marked with triangular symbols. The phase regions liquid, γ-TiAl and γ-TiAl+r-TiAl$_2$ are marked accordingly. Furthermore, the Ti$_3$Al$_5$ (metastable) decomposition line is drawn, which is dotted above 1 at.% Mo due to the formation of the Ti$_3$Al$_5$-phase being suppressed.

As previously described, the Ti$_3$Al$_5$ decomposition of VAR-Ti-60.3Al-3Mo was poorly pronounced and the exact temperature very difficult to determine. Only insignificant amounts of Ti$_3$Al$_5$ are present in heat-treated states of all kind for VAR-Ti-60.3Al-3Mo. The decomposition line above 1 at.% Mo was therefore dotted to represent the at least exceedingly inhibited formation of Ti$_3$Al$_5$. Because the decomposition effect is still highlighted for 1 at.% Mo, it was decided to dot the line beyond the 1 at.% Mo spot. The actual course beyond 1 at.% Mo is presently unknown and could therefore be topic of further studies.

Furthermore, farther raising the Mo content of Ti-60Al beyond 3 at.% might permanently suppress h-TiAl$_2$ and r-TiAl$_2$ formation. At this point the tetragonal Ti$_3$Al and its ternary cubic form could take place in the microstructural evolution, which were discussed as a possibility in section 2.8, but were not observed in either way during the study.

Future investigations should consider the fact that Ti_3Al_5 could not be verified by XRD and SEM and therefore TEM investigations might be a reasonable step for additional determination.

To further investigate the grain-refining capabilities of B addition to Al-rich TiAl alloys, samples with similar composition but highly differing B contents should be analysed. Though a grain-refining effect might have taken place after 1000 °C / 200 h / WQ for VAR-Ti-59.8Al-1Mo-3.9Nb-0.03B, a proper assignment to the B supplement was not possible due to a lack of comparable compositions.

As to increase comparability and reproducibility, prospective studies should also focus on improving sample quality in terms of manufacturing related segregations and damages. Advancing cooldown rates and proper homogenization heat treatments previously to specific heat treatments might prove highly prosperous.

6 Conclusions

As possible future high performance materials Al-rich TiAl alloys suffer from persistent metastable phases, embrittling the alloy and delaying a microstructural and thermodynamical equilibrium state. The capabilities of additional alloying elements such as Mo, Nb and B to suppress unwanted phases and accelerate transformation to equilibrium were topic of this thesis.

The insights from the microstructural and thermal investigation in chapter 4 summarise as follows: the full extent of microstructural evolution resembles observations known from research on the binary system. Both manufacturing routes resulted in cracks and fissures as well as highly segregated microstructures. Manufacturing via levitation melting resulted in more fine-grained microstructures, whereas the specimens revealed dendritic structures when processed via vacuum arc remelting. Mo segregated during first cooldown in all samples, whereas Nb did not. It was possible to homogenize the segregated states by annealing the samples at 1400 °C for one hour followed by furnace cooling. Increasing contents of Mo as well as Nb shifted the microstructural equilibrium towards a state similar to binary compositions with comparably lower Al content by suppressing Al-rich metastable phases as well as stable ones. Although virtually entirely lamellar structures of γ-TiAl and r-$TiAl_2$ were still achievable for 1 at.% Mo, the kinetic rate of reaching equilibrium was highly decelerated by increasing the Mo and Nb content, and not a single specimen reached a microstructural equilibrium state although heat treatments were conducted up to 500 hours. 3 at.% Mo revealed to be nearly sufficient to suppress the unwanted Ti_3Al_5 as shown by differential scanning calorimetry though the alloy did also suppress r-$TiAl_2$ to an extend where only plates of r-$TiAl_2$ were present in an γ-TiAl matrix and the kinetic evolution was highly delayed. The respective results were summarized in a quasi binary phase diagram for Ti-Al-Mo and Ti-60Al Mo.

The addition of 3.9 at.% Nb also proved to impede kinetics of the microstructural evolution as well as supporting the formation of the metastable Ti_3Al_5. Furthermore, r-$TiAl_2$ plates appeared to be finer grained, which might be attributed to the higher concentration of alloying elements and a therefore decreased diffusion rate.

Overall, adding further alloying elements to Al-rich TiAl alloys impeded microstructural evolution in terms of reaching an equilibrium state and partially suppressed wanted as well as unwanted intermetallic phases. Still, Al-rich TiAl with an γ-TiAl + r-$TiAl_2$ microstructural base might be of high interest for further investigation. After all, not a large number of uncoated intermetallic high-performance materials can be kept in an air atmosphered furnace at 1000 °C for 200 hours without tremendous damages from pervasive oxidation.

7 Bibliography

[1] H. Kestler, H. Clemens, in: C. Leyens, M. Peters, (ed), "Titanium and titanium alloys", WILEY-VCH, Weinheim, 2003, p. 351-392.

[2] H. Clemens, S. Mayer, Design, processing, microstructure, properties, and applications of advanced intermetallic TiAl alloys, Advanced Engineering Materials 15 (2013) 191-215.

[3] X. Wu, Review of alloy and process development of TiAl alloys, Intermetallics 14 (2006) 1114-1122.

[4] M. Eckert, K. Hilpert, in: H.J. Grabke, M. Schütze, (ed), "Oxidation of intermetallics", WILEY-VCH, Weinheim, 1997, p. 238-243.

[5] L.C. Zhang, M. Palm, F. Stein, G. Sauthoff, Formation of lamellar microstructures in Al-rich TiAl alloys between 900 and 1100°C, Intermetallics 9 (2001) 229-238.

[6] M. Palm, L.C. Zhang, F. Stein, G. Sauthoff, Phases and phase equilibria in the Al-rich part of the Al-Ti system above 900 °C, Intermetallics 10 (2002) 523-540.

[7] F. Appel, J.D.H. Paul, M. Oehring, "Gamma Titanium Aluminide Alloys", WILEY-VCH, Weinheim, 2011, p. 9-10.

[8] J.C. Schuster, H. Ipser, Phases and phase relations in the partial system $TiAl_3$-TiAl, Zeitschrift für Metallkunde 81 (1990) 389-396.

[9] M. Palm, F. Stein, in: Y.-W. Kim, D.M. Dimiduk, M.H. Loretto, (ed), "Gamma titanium aluminides", TMS, Warrendale, PA, 1999, p. 161.

[10] J.C. Schuster, M. Palm, Reassessment of the binary aluminium-titanium phase diagram, Journal of Phase Equilibria and Diffusion 27 (2006) 255-277.

[11] A. Raman, K. Schubert, On the constitution of some alloy series related to $TiAl_3$ II, Zeitschrift für Metallkunde 56 (1965) 44-52.

[12] F.J.J. van Loo, G.D. Rieck, Diffusion in the titanium-aluminium system - II. Interdiffusion in the composition range between 25 and 100 at.% Ti, Acta Metallurgica 21 (1973) 73-84.

[13] R. Kainuma, J. Sato, I. Ohnuma, K. Ishida, Phase stability and interdiffusivity of the $L1_0$-based ordered phases in Al-rich portion of the Ti-Al binary systems, Intermetallics 13 (2005) 784-791.

[14] A. Loiseau, A. Lasalmonie, G. van Tendeloo, J. van Landuyt, Ordered structures in Ti Al alloys in the composition range from AB to AB_3, MRS Symp. Proc. 21 (1984) 381-385 (C,TEM)

[15] R. Miida, M. Kasahara, D. Watanabe, Long-period antiphase domain structures of Al-Ti alloys near composition Al_3Ti, Japanese Journal of Applied Physics 19 (1980) 707-710.

[16] J. Braun, M. Ellner, B. Predel, About the structure of the high-temperature phase $Ti_{1-x}Al_{1+x}$, Journal of Alloys and Compounds 203 (1994) 189-193.

[17] F .J. J. van Loo, G.D. Rieck, Diffusion in the titanium-aluminium-I. Interdiffusion between solid Al an Ti or Ti-Al Alloys, Acta Metallurgica 21 (1973) 61-71.

[18] T. Nakano, A. Negishi, K. Kayashi, Y. Umakoshi, Ordering process of Al_5Ti_3, h-Al_2Ti and r-Al_2Ti with f.c.c.-based long-period superstructures in rapidly solidified Al-rich TiAl alloys, Acta Materialia 47 (1999) 1091-1104.

[19] M. Palm, N. Engberding, F. Stein, K. Kelm, S. Irsen, Phases and evolution of microstructures in Ti-60 at.% Al, Acta Materialia 60 (2012) 3559-3569.

[20] F. Stein, L. C. Zhang, G. Sauthoff, M. Palm, TEM and DTA study on the stability of Al_5Ti_3- and h-Al_2Ti-superstructures in aluminium-rich TiAl alloys, Acta Materialia 49 (2001) 2919-2932.

[21] F. Stein, M. Palm, in Intermetallics and Superalloys, Euromat 1999, D. G. Morris, S. Naka, P. Caron, WILEY-VCH, Weinheim, 2000, p.336.

[22] D. Sturm, Dissertation, Otto-von-Guericke-Universität Magdeburg, 2010.

[23] D. E. Mikkola, J. P. Nic, S. Zhang, W. W. Milligan, Alloying of Al_3Ti to form cubic phases, ISIJ International 31 (1991) 1076-1079.

[24] J. P. Nic, S. Zhang, D. E. Mikkola, Observations on the systematic alloying of Al_3Ti with fourth period elements to yield cubic phases, Scripta Metallurgica et Materialia 24 (1990) 1099-1104.

[25] S. Zhang, J.P. Nic, D.E. Mikkola, New cubic phases formed by alloying Al_3Ti with Mn and Cr, Scripta Metallurgica et Materialia 24 (1990) 57-62.

[26] S. Vyazovkin, A.K. Burnham, J.M. Criado, L.A. Pérez-Maqueda, C. Popescu, N. Sbirrazzuoli, ICTAC Kinetics Committee recommendations for performing kinetic computations on thermal analysis data, Thermochimica Acta 520 (2011) 1-19.

[27] ThyssenKrupp Materials Schweiz, Titan Grade 2, Juni 2017, www.thyssenkrupp.ch/documents/Titan_Grade_2.pdf